Charles University in Prague

Faculty of Mathematics and Physics

DOCTORAL THESIS

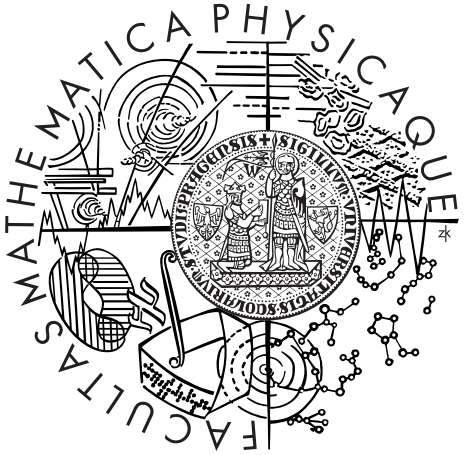

Mgr. Martin Varga

Study of electrical and dielectric properties of conducting polymers

Department of Macromolecular Physics

Supervisor:	RNDr. Jan Prokeš, CSc.
Study programme:	Physics
Specialization:	Biophysics, Chemical and Macromolecular Physics

Prague 2015

First of all, I would like to express my deep gratitude to the Dr. J. Prokeš for his advisory, extensive support during all experiments that were carried out, for collegiality and friendly working atmosphere during all these years.

Since the research topic is interdisciplinary, a lot of people was involved in various projects and scientific tasks, and the presented thesis is only a small part of them. Hence I would like to thank all people involved in. I am particularly thankful for all images from SEM, and data for density and ash residuals.

I would like to thank to members of the Department of Macromolecular Physics, namely Assoc. Prof. I. Křivka for consulting and diverse software-related support, to Assoc. Prof. J. Nedbal for a help with my internship in Athens and for the opportunity to work on challenging projects which led me to the field of numerical modeling, to Mrs. E. Alekseeva for the preparation of samples. I am grateful to Dr. A. Ryabov for many stimulating discussions and his continuing interest in the topic.

Many thanks belong to colleagues at Institute of Macromolecular Chemistry AS in Prague, first of all to Dr. J. Stejskal for intensive support related to chemistry and samples synthesis. I am deeply indebted to all colleagues who prepared samples, especially to Dr. P. Bober, Dr. M. Bláha, and others. Fruitful collaboration with the group of spectroscopy, namely with Assoc. Prof. M. Trchová and Dr. Z. Morávková is fully acknowledged. Many thanks also to colleagues at the University of Chemistry and Technology Prague for sample preparation and SEM images, particularly to Mrs. J. Kopecká and Dr. D. Kopecký.

I am thankful to people from the dielectric group at National Technical University of Athens where I spent fruitful three months in cordial atmosphere extending my research interest to the field of sensors. Namely to Prof. P. Pissis, Assoc. Prof. A. Kyritsis, Dr. C. Pandis and Mr. C. Chatzimanolis.

A number of low temperature experiments and magnetoresistance measurements were carried out in the Magnetism and Low Temperature Laboratories supported within the program Czech Research Infrastructures (LM2011025). The access and support of the staff is fully acknowledged.

The financial support from the projects of the Ministry of the Education, Youth and Sports of the Czech Republic (SVV–2011–263305, SVV–2012–265305, SVV–2013–267305, SVV–2014–260093) and the Czech Science Foundation (13–00270S) is fully acknowledged.

Last but not least, many thanks to all my friends and family who supported me during all these years. Special thanks to my beloved wife for her support and patience while working on the thesis.

I declare that I carried out this doctoral thesis independently, and only with the cited sources, literature and other professional sources.

I understand that my work relates to the rights and obligations under the Act No. 121/2000 Coll., the Copyright Act, as amended, in particular the fact that the Charles University in Prague has the right to conclude a license agreement on the use of this work as a school work pursuant to Section 60 paragraph 1 of the Copyright Act.

In Prague, ... Mgr. Martin Varga

Název práce: Studium elektrických a dielektrických vlastností vodivých polymerů

Autor: Mgr. Martin Varga

Katedra: Katedra makromolekulární fyziky

Vedoucí disertační práce: RNDr. Jan Prokeš, CSc., KMF MFF UK

Abstrakt: Transport elektrického náboje v polyanilinu a polypyrrolu byl studován s ohledem na jejich různou morfologii, dále pak v souvislosti s použitím různých oxidantů, různých dopantů a též s ohledem na další modifikace při jejich přípravě. Mechanismus transportu náboje je diskutován v rámci kombinace různych modelů popisujících transport v neuspořádaných systémech. Tento přístup je vhodný z důvodu heterogenní struktury vodivých polymerů. Byl také studován vliv vody na vodivost, v dlouhočasové limitě je pro vzorky lisované do tablet navrženo vysvětlení jevu na základě difúzního modelu. Zkoumali jsme stabilitu polypyrrolových nanotrubek v silně zásaditých prostředích a také jejich stárnutí, a to pomocí stejnosměrných i střídavých měřicích technik. Vodivost studovaných materiálů při jejich přirozeném stárnutí zůstává stejného řádu i po dvou letech, avšak při deprotonaci v silných alkáliích nebo při zrychleném stárnutí za zvyšených teplot klesá vodivost polymerů o několik řádů. Materiál se tak stává silně neuspořádaným s jiným mechanismem transport náboje. Jako příklad praktické aplikace použití vodivých polymerů byla studována odezva polyanilinu reprotonovaného různými kyselinami na čpavek. Nejlepší výsledek byl získán pro vzorky dopované kyselinou metasulfonovou.

Klíčová slova: vodivé polymery, transport náboje, elecktrická vodivost, stárnutí

Title: Study of electrical and dielectric properties of conducting polymers

Author: Mgr. Martin Varga

Department: Department of Macromolecular Physics

Supervisor: RNDr. Jan Prokeš, CSc., Department of Macromolecular Physics

Abstract: Charge transport in polyaniline (PANI) and polypyrrole (PPy) was studied in respect to various oxidants, dopants, morphology, and other modifications in their synthesis. The mechanism of transport was discussed in the framework of combination of several models characteristic for disordered solids due to inherent heterogeneous structure of conducting polymers. Effect of drying on conductivity was studied and the long-time limit was explained with the diffusion-based model for bulk materials. For PPy nanotubes stability in strong alkaline media and aging were studied by AC and DC techniques. While conductivity of naturally aged samples after two years remained in the same order of magnitude, after exposure to alkaline media or accelerated aging at high temperatures, conductivity decreased several orders of magnitude. Degraded material exhibited strong disorder and the transport model was completely changed. Despite severe treatment electrical properties were still comparable to other as-prepared materials. Finally, an application example as ammonia sensor, the response of PANI reprotonated with various sulfonic acids was studied with the best performance achieved for MSA.

Keywords: conducting polymers, charge transport, electrical conductivity, aging

Contents

Preface

Although conducting polymers (CP) have been studied for several decades since their discovery, the understanding of their properties which mankind can benefit from, *e.g.* use in applications, is due to their complexity far from being complete. Intensive research started in mid of 70's was crowned by the Nobel prize award to A.J. Heeger, A.G. MacDiarmid and H. Shirakava in 2000. A comprehensive introduction to the field can be found in their Nobel lectures [1, 2]. The interdisciplinary field of conducting polymers has been fully established and continuous interest is reflected in numerous papers that have been published so far.

The aim of the thesis is investigation of the influence of various parameters reflected in synthesis and/or post-treatment on the charge transport properties, particularly on conductivity and charge transport mechanisms. In this thesis we limit ourselves to two of the most important representatives in the field—polyaniline and polypyrrole. In the work we tried to address several problems coming mainly from vast variety of experimental conditions at the level of synthesis (different oxidants, dopants, polymerization temperature, *etc.*) and post-treatment (deprotonation in alkaline media, reprotonation) and their effects on the final electrical properties. The second problem studied here is long-term stability of electrical properties important for their successful introduction to market. At the end a case study of response to ammonia is presented. All experimental results come hand by hand with the study of the charge transport phenomena and they were tried to be mapped onto physical models at least on the phenomenological level.

The presented thesis is composed from four chapters. First chapter is dedicated to introduction to the studied field reviewing the basic properties of conducting polymers and various commonly used theoretical models for charge transport explanation. The second chapter reviews experimental methods used for measurements of conductivity and permittivity, continues with the description of apparatuses used, ending with the brief description of the studied samples although their direct synthesis was not the subject of the work. Third and fourth chapters contain results and discussion divided into several sections. The former deals mostly with effect of various factors, such as oxidants, dopants, polymerization temperature, templates or silver decoration, on the charge transport mechanism and related physical parameters. The latter is focused more on the stability of electrical properties facing natural and accelerated aging, aggressive alkaline media and drying. Owing to the number of presented results, each section is ended with a short summary. This chapter is followed with the overall conclusions and outlooks.

1. Introduction to conducting polymers

This chapter reviews basic knowledge needed to understand charge transport in disordered systems, particularly conducting polymers (CP). Starting with very basic terms, followed by the introduction to CP with attention focused on various charge transport models, and ending up with stability and applications review. The aim of this chapter, however, is not to provide broad list of physical and chemical properties even though they have impact on charge transport properties. They can be easily found in field-related literature.

1.1 Basic terms

The interaction of the electromagnetic field and matter on macroscopic scale is well described by the set of Maxwell's equations. Introduction to this topic can be found in a number of textbooks (*e.g.* [3, 4]). Nevertheless, in the following, at least basic terms are briefly listed. The electrical conductivity σ reflects the proportionality between the electric current density $\vec{j}$ as a response of system to the perturbation by the electric field $\vec{E}$. Within the linear response theory, when the applied field is low, it is expressed by the well-known Ohm's law:

$$\vec{j}(\vec{r}) = \sigma\vec{E}(\vec{r}) = -\sigma\nabla\varphi(\vec{r}). \tag{1.1}$$

Generally, conductivity is a tensor of second order, in case of isotropic conductivity it is reduced to number. Eq. (1.1) can be also viewed as an ordinary differential equation for electric potential $\varphi(\vec{r})$. Hence, spatial maps of the current density and potential can be obtained when it is solved. For problems diverse in geometry and boundary conditions, it can be treated numerically for instance by the finite element method (FEM) widely used for much complex partial differential equations [5]. However, details are beyond the scope of the thesis. In the following, the dependence on spatial coordinates is omitted. On a macroscopic (integral) scale, the resistance R of piece of material can be related to its resistivity $\rho = 1/\sigma$ via dimensions, for instance, in the simple wire geometry with the cross section A and the length l :

$$R = \rho\frac{l}{A}. \tag{1.2}$$

Throughout the work conductivity is expressed in $\mathrm{S\,cm^{-1}}$ and the electrical resistivity in $\Omega\,\mathrm{cm}$.

Similarly to the conductivity, the (relative) dielectric permittivity expresses relationship between the electric field and the electric displacement $\vec{D}$:

$$\vec{D} = \epsilon_\mathrm{r}\epsilon_0\vec{E}, \tag{1.3}$$

with the permittivity of free space ϵ_0. It can be expressed in a form of the polarization P in material which comes from bound charges:

$$\vec{P} = (\epsilon - 1)\epsilon_0 \vec{E}. \tag{1.4}$$

Analogously to Eq. (1.1), the potential map can be obtained after application of the divergence operator to Eq. (1.3) and hence, solving the Poisson's equation. Macroscopically, the capacity C can be related to the dielectric permittivity of material the corresponding capacitor is made from:

$$C = \epsilon_\mathrm{r}\epsilon_0 \frac{A}{l}. \tag{1.5}$$

In the case of the time dependent electric field, for instance the periodic one $\vec{E}(\omega) = \vec{E}_0 e^{i\omega t}$ with the angular frequency ω (or the frequency $f = \omega/(2\pi)$), conductivity is generally frequency dependent as well:

$$\vec{j}(\omega) = \sigma^*(\omega)\vec{E}(\omega), \tag{1.6}$$

and usually expressed as a complex variable. In this case it concerns both, resistive and capacitive response. Alternatively, ϵ^* formalism can be used:

$$\sigma^*(\omega) = i\omega\epsilon_0\epsilon^*. \tag{1.7}$$

The real part ϵ' is related to energy reversibly stored in the system and the imaginary part ϵ'' is related to the dissipated energy. The latter includes the DC contribution of free carries to the imaginary part $i\epsilon_0\sigma_\mathrm{DC}/(\omega)$ [4].

In the condensed matter physics, conductivity can be understood as a material property derived from some microscopic model; for instance, the kinetic theory of electron gas results in the famous Drude formula [6]:

$$\sigma = \frac{ne^2\tau}{m} \tag{1.8}$$

with the charge carrier concentration n, electric charge e, charge carrier mass m and relaxation time τ (time between two collisions). Transport properties of solids can be better understood within the band theory. Then the electronic structure of materials is decisive, with a partially filled conduction band for metals and an empty conduction band for semiconductors with the Fermi energy level E_F in the band gap between the conduction and the valence band. Temperature dependence of conductivity can be derived using the Boltzmann transport equation. For crystalline metals at high temperature region a linear increase of resistivity with temperature is due to scattering of conducting electrons on phonons:

$$\sigma(T) = \frac{1}{\rho_\mathrm{r}(1 + \alpha_\mathrm{r}(T - T_\mathrm{r}))} \tag{1.9}$$

with the resistivity ρ_r at reference temperature T_r and the thermal coefficient for resistivity α_r. This well known model will be important when we discuss conductivity of composites of CP with silver. At low temperatures linear dependence

changes to power law with exponent about 5. In case of metals, there is finite residual resistivity at zero temperature limit due to impurities and imperfections. Detailed description of low temperature transport phenomena in crystalline metals is however beyond the scope of this thesis since they are not of prime interest. For crystalline semiconductors, typically temperature activated transport occurs, for instance promotion of electrons to the conduction band:

$$\sigma(T) \sim \exp\left(\frac{E_\mathrm{A}}{k_\mathrm{B}T}\right), \tag{1.10}$$

where k_B is the Boltzmann constant and E_A is an appropriate activation energy. Introduction of additional charge carriers (electrons, holes) to material due to their rather low intrinsic density is referred as doping. More diverse behaviour can be found for disordered solids, the group of materials CP belong to. Overview of their properties follows.

1.2 General overview of condcuting polymers

Conducting polymers are referred to intrinsically conducting conjugated polymers. The most famous and studied representatives are polyacetylene (PA), polyaniline (PANI), polypyrrole (PPy), poly(*p*-phenylene vinylene) (PPV), polythiofene (PTh) and poly(3,4-ethylenedioxythiophene) (PEDOT) , some of them are depicted on Fig. 1.1, but much more could be listed [1]. Since this thesis is focused on PANI and PPy their properties are preferentially discussed.

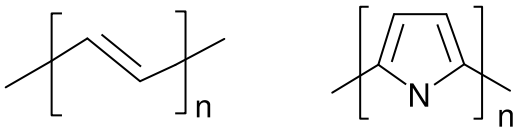

(a) PA (b) PPy

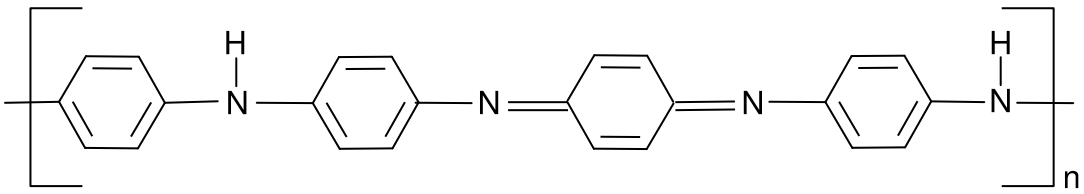

(c) PANI

Figure 1.1: Chemical structure of common conducting polymers.

From the nature of one dimensional (1D) conjugated π-electron system the metallic state with half-filled conducting band should be found. The electronic structure of polyacetylene (with the most simple chemical structure) was theoretically calculated using the so-called SSH hamiltonian within the tight-binding approach. The metallic (ground) state was found unstable due to the Peierls distortion in 1D systems, and after dimerization the band gap was open, therefore

converting conducting polymers into the insulators [7]. The more complicated CP were later modeled with the unified SSH hamiltonians [8]. Alternatively, the electronic structure of CP was obtained using *ab initio* calculations [9] or using the density functional theory [10].

Since the nature of pristine CP was found insulating, charge transport is rather due to impurities and defects. For instance, in PA such conformational defect is called soliton. It is quasiparticle which does not carry charge but spin. In other CP charged quasiparticles are common such as polarons and bipolarons. Since the intrinsic concentration of such defects is low, in order to increase conductivity additional carries have to be introduced. This effect is referred as doping and can be done in various routes, *e.g.* chemical, electrochemical, photochemical, or interfacial (by injection from electrode). It can be permanent (with presence of counterions) or temporal [1]. During this process the number of electrons is changing. The exception is the so-called protonation during reaction with protonic acid. Then, protons are donated to polymer chain and the positive charge is compensated by anion from acidic solution resulting in the salt form. The electrons are redistributed to form polarons/bipolarons [11]. Conductivity depends strongly on the degree of protonation, for instance in PANI it varies from 10^{-8} to $1\,\mathrm{S\,cm^{-1}}$ [12]. The final properties depend on the concentration and type of anion (dopant). For instance, while PANI sats produced by hydrochloric acid (HCl) are generally insoluble, when doped with camphorsulfonic acid (CSA) PANI becomes soluble in *m*-cresol [13]. With increasing level of doping the transition from insulating to metallic region was observed with possible tuning by external magnetic field or pressure [14, 15]. The transition between these regimes is usually referred as the metal-to-insulator transition (MIT).

Besides chemical structure, the morphology of CP determines the final properties. A vast variety of morphologies can be found as CP form granules (common), nano/microtubes, nanowires, nanorods, *etc.* [16]. Several methods concerning various hard of soft templates techniques for CP synthesis alongside with their electrical properties and applications have been recently reviewed [17]. The interest for nanotubular form started during the 80's when hard templates were successfully employed [18]. As example, significant enhancement of conductivity was reported in case of PPy fibrils (diamater 30 nm) [19] or PPy nanotubes (wall thickness 15 nm) [20] with conductivity estimated to 2215 and $5000\,\mathrm{S\,cm^{-1}}$, respectively. In some cases, template is not necessary and self-assembly process takes place, for instance polyaniline nanotubes are formed in the presence of weak acid but with poor conductivity of 10^{-2}–$10^{-1}\mathrm{S\,cm^{-1}}$ [21].

1.3 Charge transport models

Conductivity and the charge transport mechanism in CP is complex as it depends on several factors such as the doping level, the level of disorder and its homogeneity, properties of polymer backbone as well as dopant counter-ions [1]. Furthermore, granularity as an inherent morphological heterogeneity of CP was

claimed to be crucial in charge transport [22]. Review of several commonly used models and approaches to transport in CP can be found in Ref. [23].

In the following we categorize three basic regimes reflected in the temperature dependence of conductivity, $\sigma(T)$:

- metallic regime, $\mathrm{d}\sigma/\mathrm{d}T < 0$, heavily doped CP
- critical regime, $\mathrm{d}\sigma/\mathrm{d}T > 0$, transition between metallic and insulating regime
- insulating (semiconducting) regime, $\mathrm{d}\sigma/\mathrm{d}T > 0$, low and moderately doped CP with thermally activated charge transport.

The most of the attention will be focused on the semiconducting regime as the most prominent one in our samples.

1.3.1 Metallic regime

When the level of doping in CP is sufficiently high and material consist from well oriented polymer chains with high degree of perfection a metallic behavior can be observed. Conducting polymer can be viewed as quasi-one dimensional metal with high anisotropic conductivity along the chain, only limited by the back scattering on the polymer backbone $2k_\mathrm{F}$ (k_F is the Fermi wavevector) phonons [24, 25]:

$$\sigma(T) = \sigma_0^\mathrm{M} \exp\left(\frac{\hbar\omega_\mathrm{ph}}{k_\mathrm{B}T}\right) \tag{1.11}$$

where $\hbar$ is the reduced Planck constant, ω_ph is the $2k_\mathrm{F}$ phonon frequency, which however differs from authors to authors. Pre-exponential factor depends on the electron-phonon interaction, the transfer integral, the mass and the length of the repeat unit. Experimentally, the metallic behavior was observed for heavily doped PA but the expected anisotropic conductivity of order $10^6\,\mathrm{S\,cm^{-1}}$ has not been achieved maybe due to structural defects, thus being the limit of transport [1, 25]. Nevertheless, conductivity as high as $1.5 \times 10^5\,\mathrm{S\,cm^{-1}}$ was achieved for iodine-doped PA [26].

1.3.2 Critical regime

In CP a crossover from the metallic state to the insulating state is often found. This can be viewed either as the disorder-induced localization crossover or percolation-based disorder in case of granular metal structure depending on homogeneity of material [15]. This issue is discussed mainly in the next subsection. In the former case, for the 3D system in the critical region activated charge transport is absent

and $\sigma(T)$ is given by the power law (PL) [27]:

$$\sigma(T) \sim \frac{\hbar^2}{e^2 p_{\mathrm{F}}} \left(\frac{k_{\mathrm{B}} T}{E_{\mathrm{F}}} \right)^{\gamma} = a T^{\gamma} \tag{1.12}$$

where p_{F} is the Fermi momentum. When the disorder in CP is strong, all states become localized (mobility edge is shifted towards the band gap center) and material behaves as the insulator [28]. Extensive experimental results for variety of CP, including driving the systems through MIT via application of external magnetic field or pressure, were reported alongside with several unresolved issues that come from complex structure of CP [29]. Besides, the GM approach to MIT was questioned in the same work. On the other hand, the explanation of MIT only by disorder-like models was subjected to criticism as well since it did not consider the interchain charge transfer and the interplay between electronic correlations [30]. Therefore, the perturbation theory and the scaling analysis arguments were used for its consistent explanation [31].

1.3.3 Insulating regime

In the case of undoped or lightly doped CP their behavior is insulating or semiconducting. Due to their disordered character with prevailing amorphous phase over the semicrystalline regions charge transport can be described by models developed for amorphous semiconductors or granular metals [15]. The commonly used charge transport models for CP were reviewed in Ref. [23] and we list them as well since they were used for our experimental data evaluation.

Hopping-based models

In CP, the charge carriers (solitons, polarons, bipolarons) are localized due to strong (Anderson) localization [1]. This happens due to constructive interference in back-scattering events, the charge carrier cannot diffuse freely and becomes trapped [32]. These localized states are located in the band gap (mid-gap states) and charge can be transmitted due to the phonon-assisted non-resonance tunneling referred as hopping [33]. One of the most common model of such thermally activated hopping mechanism is the so-called variable range hopping (VRH) model developed by Mott [34]. In this scenario the charge carrier can hop either to state with different energy (E_{ij} being the difference energy) or to a more distant state in space with the relative distance R_{ij}, whatever is more probable. In this model, a single-phonon hopping rate ν_{ij} introduced by Miller and Abrahams is used [35]:

$$\nu_{ij} \sim t_0^2 \exp - \left(\frac{E_{ij}}{k_{\mathrm{B}} T} + 2 R_{ij} / \xi \right) \tag{1.13}$$

with the electronic transfer energy t_0 and the localization length ξ. Maximizing the probability of hop one can obtain the famous stretched-exponential depen-

dence which for arbitrary dimension D of transport takes a form [36]:

$$\sigma(T) = \sigma_0^{\mathrm{Mott}} \exp\left(-\left(\frac{T_0^{\mathrm{Mott}}}{T}\right)^n\right), \tag{1.14}$$

with an exponent $n = 1/(1+D)$. Parameters T_0^{Mott} and σ_0^{Mott} reflect the disorder in material through the localization length ξ [37]:

$$T_0^{\mathrm{Mott}} = \frac{18.1}{g(E_{\mathrm{F}})k_{\mathrm{B}}\xi^3}, \tag{1.15}$$

$$\sigma_0^{\mathrm{Mott}} = \nu_{\mathrm{ph}} T^2 \frac{18.1}{g(E_{\mathrm{F}})k_{\mathrm{B}}\xi^3}, \tag{1.16}$$

with the phonon attempt frequency ν_{ph} and the density of states at the Fermi level $g(E_{\mathrm{F}})$ which is assumed to be constant. Comparing to strong exponential dependence σ_0^{Mott} can be considered as temperature-independent. In general, pre-exponential factors play a rather minor role. More details about the VRH model alongside with the multi-phonon hopping approach can be found in a recent review [33]. Within this model the optimum hopping distance R_{hop} and the hopping activation energy E_{hop} can be obtained [36]:

$$R_{\mathrm{hop}} = \left(\frac{9\xi}{8\pi g(E_{\mathrm{F}})k_{\mathrm{B}}T}\right)^{1/4}, \tag{1.17}$$

$$E_{\mathrm{hop}} = \left(\frac{3}{4\pi g(E_{\mathrm{F}})R_{\mathrm{hop}}^3}\right). \tag{1.18}$$

The localizes states contribute to dielectric constant by factor:

$$\epsilon_{\mathrm{r}} = 4\pi e^2 g(E_{\mathrm{F}})\xi^2/\epsilon_0 \tag{1.19}$$

which becomes dominant over intrinsic (core) ϵ_{r} near MIT where ξ tends to diverge [37]. Various numerical factors can be found for Eq. (1.19) [38]. When some functional form of the density of states is assumed, *e.g.* $g(E) \sim E^{\mu}$, the exponent in Eq. (1.14) is modified to $n = (1+\mu)/(1+D+\mu)$ [39]. Further complication arises from the mutual electron-electron Coulomb interaction which leads to the so-called soft gap in $g(E)$ which vanishes at the Fermi energy. This 3D VRH model, important mainly at low temperatures, is referred as Efros-Shklovskii VRH model (ES VRH) and it leads to exponent 0.5 in Eq. (1.14) [40]. Unfortunately, it coincides with the quasi-one-dimensional VRH model (Q1D VRH) where transport is limited by interchain hopping which is weaker than the intrachain one. [41] This model thus accounts for the internal heterogeneity, emphasizes one-dimensional nature of CP and as such considers anisotropy of conductivity. It was successfully applied on PANI and its derivatives [38,42]. Parameters T_0^{ES} [40] and T_0^{Q1D} [41] differ:

$$T_0^{\mathrm{ES}} = \frac{2.8e^2}{4\pi\epsilon_0\epsilon_{\mathrm{r}}k_{\mathrm{B}}\xi}, \tag{1.20}$$

$$T_0^{\mathrm{Q1D}} = \frac{8}{zg(E_{\mathrm{F}})k_{\mathrm{B}}\xi}, \tag{1.21}$$

where z the number of nearest neighbor chains and the density of states and the localization length are meant along the polymer chain. The numerical factor in Eq.(1.38) is changed to 16 if $g(E_F)$ concerns both signs of spin of charge carriers [38]. Various numerical factors can be also found for Eqs. (1.15) and (1.20) as summarized in Ref. [43]. Since the optimum hopping distance decreases with temperature, Eq. (1.17), at a certain value of the thermal energy only the nearest-neighbor hops prevail and VRH is changed to the nearest neighbor hopping (NNH) with the exponent in Eq. (1.14) changed to 1 [36], particularly to:

$$\sigma = \sigma_0^{\mathrm{NNH}} \exp\left(-\frac{E_{\mathrm{hop}}}{k_B T}\right), \tag{1.22}$$

Unfortunately, there is a whole family of models based on hopping mechanism with the same functional dependence. To name some others, the model of NNH in a system with distribution of conjugation lengths leads to exponent 1/3 [44], the model with the linear Coulomb gap in coupled metallic rods gives 2/5 [45] and hopping between superlocalized states yields 3/7 [46]. In the case of the variable range hopping, also the crossover between ES and Mott VRH can appear at low temperatures, either as a smooth one [43,47] or a more abrupt one [48]. Moreover, models based on tunneling between granular metals (islands) can give the same functional form as discussed later.

In spite of ambiguity in determination of the model from the exponent it remains the foremost important parameter. A useful way of its estimation is the so-called Zabrodskii plot of the reduced activation energy W on temperature (double logarithmic) [49]:

$$W = T\frac{d\ln(\sigma)}{dT}. \tag{1.23}$$

When calculated for Eq. (1.14), one can easily obtain the exponent from the slope of the plot.

Besides $\sigma(T)$, the transport model can be determined from electric or magnetic field dependence of conductivity. For the Mott VRH model at moderate electric fields, $eER \sim k_B T$, conductivity has the following functional form [36]:

$$\sigma(E) \sim \exp\left(-\frac{eER}{k_B T}\right), \tag{1.24}$$

while at much higher fields, the thermal activation is no longer necessary:

$$\sigma(E) \sim \exp\left[-\left(\frac{E_0}{E}\right)^{0.25}\right], \tag{1.25}$$

with the parameter E_0 depending on ξ and $g(E_F)$. In the case of the Q1D VRH model [42] and the ES VRH model [50], the exponent is changed to 0.5 with corresponding change in E_0. More details are not presented here, since $\sigma(E)$ were not investigated in the present work. Another tool to obtain additional information about charge transport is the magnetic field (or the magnetic induction B) dependence, in particular magnetoresistance ($\mathrm{MR} = (\rho(B) - \rho_0)/\rho_0$). In case of the

VRH model the MR effect is due to the shrinkage of the localized wavefunctions overlap, and it is positive with the quadratic dependence in weak magnetic fields:

$$\ln\left(\frac{\rho(B,T)}{\rho(0,T)}\right) = t\left(\frac{\xi}{L_B}\right)^4\left(\frac{T_0}{T}\right)^y \sim B^2, \tag{1.26}$$

with the magnetic length $L_\mathrm{B} = \sqrt{\hbar/eB}$, the numerical factor $t = 5/2016$ or 0.0015, and the exponent $y = 3/4$ or $3/2$ for Mott VRH or ES VRH [36, 51], respectively. In high magnetic fields the $B^{1/3}$ dependence can be obtained [51]:

$$\ln\left[\frac{\rho(B,T)}{\rho(0,T)}\right] = \left(\frac{2.1eB}{g(E_\mathrm{F})\hbar L_\mathrm{B} k_\mathrm{B} T^3}\right)^{1/3} \sim B^{1/3}, \tag{1.27}$$

with crossover between regimes at a certain value of the magnetic field B_c:

$$B_\mathrm{c} = \frac{\hbar(g(E_\mathrm{F})k_\mathrm{B}T)^{1/4}}{e\xi^{5/4}}. \tag{1.28}$$

A general but empirical dependence on the magnetic field containing only one fitting parameter with mentioned low- and high-field limits has been later suggested [52]. The situation becomes even more puzzling with an effect of the forward interference among various hopping paths among sites taken into account which results in negative MR [53]. In the model, the numerical averaging of logarithm led to linear dependence of MR on the magnetic field. More rigorous approach, the critical percolation method, led to quadratic dependence [54]. However, in practice, the empirical relation with corresponding adjustable parameters C_sat, B_sat is used instead [55]:

$$\frac{\rho(B,T)}{\rho(0,T)} \sim \frac{1}{1 + C_\mathrm{sat}\frac{B/B_\mathrm{sat}}{1+B/B_\mathrm{sat}}}, \tag{1.29}$$

reduced to the linear dependence in the low-field limit (in Mott regime).

In the time-dependent harmonic field, the conductivity in the VRH regime takes the form of the Mott-Austin formula for the pair approximation [36] with one extra power in the logarithm (due to energy dimension) [39]:

$$\sigma'(\omega,T) = \sigma_\infty \frac{\omega}{\nu_\mathrm{ph}} \frac{T}{T_0^\mathrm{Mott}} \left[\ln\left(\frac{\nu_\mathrm{ph}}{\omega}\right)\right]^{D+2}, \tag{1.30}$$

and the dielectric constant is given by:

$$\frac{\epsilon'(\omega,T)-1}{(\epsilon_\mathrm{s}-1)} = 1 + \frac{T}{T_0^\mathrm{Mott}} \left[\ln\left(\frac{\nu_\mathrm{ph}}{\omega}\right)\right]^{D+3}. \tag{1.31}$$

However, at very low frequency the pair approximation is not further valid and from the hydrodynamic approximation follows:

$$\frac{\epsilon'(\omega,T)-1}{(\epsilon_\mathrm{s}-1)} = \left(\frac{T}{T_0^\mathrm{Mott}}\right)^{2/(D+1)}. \tag{1.32}$$

Hence, for given frequency, there is a maximum $\epsilon(T)$. Others expressions can be found for various VRH models depending of dimensionality (including the fractal VRH model) summarized for instance in Ref. [39]. For commonly discussed Q1D VRH model one finds:

$$\sigma'(\omega, T) = \sigma_0 \frac{T}{T_0^{\mathrm{Q1D}}} \left(\frac{\omega}{\nu_{\mathrm{ph}}} \right)^{1-(T/T_0^{\mathrm{Q1D}})}, \tag{1.33}$$

and

$$\frac{\epsilon'(\omega, T) - 1}{(\epsilon_{\mathrm{s}} - 1)} = \exp\left[\left(\frac{T}{T_0^{\mathrm{Q1D}}} \right)^{0.5} \ln\left(\frac{\nu_{\mathrm{ph}}}{\omega} \right) \right]. \tag{1.34}$$

Another hopping-based model for $\sigma^*(\omega)$ known as the random free-energy barrier model (RFEB) assumes hopping of charge carriers in the presence of spatially randomly varying energy barriers, and solved within the continuous random walk approximation it gives [56]:

$$\sigma^*(\omega) = \sigma_0 \frac{i\omega\tau}{\ln(1 + i\omega\tau)} \tag{1.35}$$

with the attempt frequency to overcome the largest barrier $1/\tau$.

We showed that hopping based models manifest themselves in several transport properties. However, their identification is not so straightforward since alternative group of models based on granular structure exhibits similar macroscopic properties. Their brief overview follows.

Granular 'metals' models

Since the heterogeneity is inherently present in CP in the form of heterogeneity of protonation distribution, or the existence of well and poorly ordered phases, models based on granular structure can be used to explain the charge transport properties [23]. These granular metals models (GM) assume existence of well conducting ('metallic') islands dispersed in less conducting matrix. Originally, they were developed for metallic particles embedded in inorganic matrices where charge transport occurs via tunneling between conducting islands through insulating barriers [57, 58]. It was shown that the charging energy E_{c}—electrostatic energy required to be overcome when two neutral grains become charged due to charge transfer is the limiting factor for the charge transport provided that metallic islands are sufficiently small. In this charging energy limited tunneling model (CELT) conductivity takes the form of the VRH model, Eq. (1.14), with exponent 0.5 when constraint of constant s/d was applied, where s is the separation between grains of size d [57]. The high electric field conductivity was obtained in the form:

$$\sigma(E) = \sigma_0 \exp\left(-\frac{E_0}{E} \right), \tag{1.36}$$

at 0 K with E_0 dependent on properties of the tunneling junction. At higher temperatures, additional term has to be added. The model was later extended to

account for experimentally observed exponent crossover to 0.25 at low temperatures or > 0.5 at high temperatures depending on distribution of grains' sizes [59]. The model was adopted to explain transport in CP by means of hopping between polaronic clusters following the same constraint for s/d [60]. The charging energy is then related to the Coulomb repulsion energy U, the monomer size a and polaronic clusters of mean diameter d separated by mean distance s:

$$E_{\mathrm{c}} = \frac{2Ua}{d(1 + d/2s)}, \tag{1.37}$$

and the parameter in Eq. (1.14) T_0^{C} is given by:

$$T_0^{\mathrm{C}} = \frac{8U(s/d)^2}{k_{\mathrm{B}}(0.5 + s/d)}. \tag{1.38}$$

However, the correlation between s and d turned out to be unnecessary to obtain VRH-like dependence according to numerical simulations based on effective medium theory, and arbitrary exponent $0.5 < n < 1$ could be found. The commonly observed value 0.5 is obtained when s and d are not correlated, random potentials are included in the charging energy distribution and the maximum intergrain distance and the maximum charging energy involved in transport are temperature dependent [61]. Obviously, the similar range of exponents with the hopping models makes the determination of the charge transport mechanism based on $\sigma(T)$ challenging.

For large islands, separated by only thin insulating layers, the conductivity is due to tunneling modified by thermal fluctuations of charge carriers in the area of junction, and the parabolic barrier approximation results in [62, 63]:

$$\sigma(T) = \sigma_0^{\mathrm{F}} \exp\left(-\frac{T_1^{\mathrm{F}}}{T + T_0^{\mathrm{F}}}\right), \tag{1.39}$$

with the pre-exponential factor σ_0^{F} treated as temperature-independent and parameters T_0^{F} and T_1^{F}:

$$T_1^{\mathrm{F}} = \frac{AV_0^2\epsilon_0\epsilon_r}{2k_{\mathrm{B}}e^2w}, \tag{1.40}$$

$$\frac{T_1^{\mathrm{F}}}{T_0^{\mathrm{F}}} = 2w\sqrt{\left(\frac{2m^*V_0}{\hbar^2}\right)}g(\lambda), \tag{1.41}$$

determined by the height of barrier V_0, the width of barrier w, the area of junction A, the effective mass m^* of charge carriers, and $g(\lambda)$ related to the probability for tunneling at the Fermi energy through the barrier potential without applied field, $\exp(-2g(\lambda))$. In the proposed approximation it is $\pi/8$. Later, the relative permittivity of insulating barriers ϵ_{r} in Eq.(1.39) was introduced [64]. The image forces correction to the barrier potential is expressed in the parameter λ:

$$\lambda = \frac{0.795e^2}{16\pi\epsilon_0\epsilon_r V_0 w}, \tag{1.42}$$

related to the properties of tunneling junction, with the upper limit 0.25. The mentioned parabolic barrier approximation was supposed to be valid mainly for

$\lambda \approx 0.07$ [63] and later to $\lambda \approx 0.148$ [65]. However it turned out that Eq.(1.39) is only rough approximation for small and medium barriers and can be used for 0.1–0.15 $< \lambda <$ 0.25 with

$$g(\lambda) = 1 - (8 - \pi)\lambda + 4(4 - \pi)\lambda^2, \tag{1.43}$$

in Eq.(1.41). In the case of high barriers, $\sigma(T)$ is given by the VRH equation, Eq.(1.14), with exponent 1/3. Further generalization of the model accounted for the thermally activated tunneling and the thermal activation of the charge carriers over the barrier [66].

For PANI as the system modeled by spherical conducting islands with the volume fraction η separated by an insulating matrix, the RFEB model and the effective medium approximation were used to obtain the total complex conductivity [67]:

$$\sigma^*(\omega) = i\omega \left[\epsilon_2 - \frac{i\sigma_2^*(\omega)}{\epsilon_0\omega}\right] \frac{2(1-\eta)\left(\epsilon_2 - \frac{i\sigma_2^*(\omega)}{\epsilon_0\omega}\right) - (1+2\eta)\frac{i\sigma_1}{\epsilon_0\omega}}{(2+\eta)\left(\epsilon_2 - \frac{i\sigma_2^*(\omega)}{\epsilon_0\omega}\right) - (1-\eta)\frac{i\sigma_1}{\epsilon_0\omega}} \tag{1.44}$$

where properties of conducting islands (purely conducting) and insulating matrix (with the RFEB model) are indexed as 1 and 2, respectively.

Various approaches to heterogeneity

Up to this point we mentioned predominantly homogeneous VRH models, except Q1D which assumes anisotropic transport, and heterogeneous models based on existence of dispersed metallic islands. In some cases, however, neither the single Eq.(1.14) nor Eq.(1.39) were able to fit a broad range of temperatures, and the superposition of various above-mentioned models including models of the metallic conductivity, based on the concept of internal heterogeneity of conducting polymers was suggested by Kaiser [68]:

$$\rho(T) = 1/\sigma(T) = \sum_{i=1}^{N} f_i \rho_i(T), \tag{1.45}$$

where N resistors connected in series represent various models. Geometrical factor $f_i = l_i A/(l A_i)$ express the fraction of material's total length and area where particular model holds. Its temperature dependence is generally neglected and the parallel contributions can be also included. This approach was particularly successful in explanation of non-monotonic $\sigma(T)$ [69].

To obtain macroscopic properties of heterogeneous systems, several methods have been developed and have been many times reviewed, *e.g.* [70–72]. Typically, when mixing conducting and nonconducting phase, high polarization is observed due to charge built-up at phase interfaces, referred as Maxwell-Wagner-Sillars (MWS) polarization. For higher concentrations, the so-called effective medium approximation (EMA) which treat inclusions to be embedded in a such effective

medium that their inclusion does not change its properties. Various formulae for this approach applied to various situation can be found in Ref. [70]. Another approach is the so-called percolation theory when the size of conducting clusters increases with conducting filler concentration and the macroscopic conductivity is achieved due to formation of 'infinite' cluster at some critical concentration Φ_c referred as the percolation threshold [73, 74]:

$$\sigma(\Phi) = \sigma_f(\Phi - \Phi_c)^t \tag{1.46}$$

$$\sigma(\Phi) = \sigma_m(\Phi_c - \Phi)^{-s} \tag{1.47}$$

where exponents cover details of the percolation model, σ_f and σ_m are related to conductivity of filler and matrix, respectively. Both EMA and percolation theory were applied in models for disordered solids mentioned above, for instance, the derivation of VRH models with a percolation treatment of the resistor network [75, 76] or the derivation of $\sigma(T)$ in the CELT model using EMA [61].

In disordered solid, where CP belong to, several 'universalities' were observed in the AC response [70,71], such as, a power law dependence on frequency for $\omega > \omega_c$ with some critical ω_c mostly related to frequency of of loss peak maximum ω_m in $\epsilon''(\omega)$. These frequencies are proportional to the contribution of DC conductivity (manifested as low frequency plateau in $\sigma'(\omega)$), which is referred to as the Barton-Nakajima-Namikawa (BNN) relation. The power law can be expressed in a form proposed by Joncher [77]:

$$\sigma'(\omega) = \sigma_0 + A\omega^s, \tag{1.48}$$

with exponent s lower than 1 and the characteristic plateau at low frequencies. Or more generally by [78]:

$$\sigma'(\omega) = \sigma_0[1 + i\omega\tau_0]^s, \tag{1.49}$$

with the characteristic relaxation time τ_0. The exponent s in Eq. (1.48) can be identified with some microscopic model when expressed in the appropriate form, such as the Q1D VRH model [39] or the RFEB model [56]. In permittivity formalism, predominantly used for dielectric spectroscopy focused on the dipolar polarization, the most generalized phenomenological function is the Havriliak-Negami dielectric function [79, 80]:

$$\epsilon^*(\omega) - \epsilon_\infty = \frac{\Delta\epsilon}{(1 - (i\omega\tau)^\alpha)^\beta}, \tag{1.50}$$

with the parameters α and β related to the shape of loss peak in $\epsilon''(\omega)$, the dielectric strength $\Delta\epsilon = \epsilon_s - \epsilon_\infty$, and the static ϵ_s. This function can be simplified for certain values of parameters, for instance, when $\alpha = 1$ it is called Cole-Davidson (CD) function, the case of $\beta = 1$ is known as the Cole-Cole (CC) function which exhibits symmetric loss peak, and the simplest case is for $\alpha = 1$ and $\beta = 1$ reduced to well-known Debye response. The position of the loss peak maximum (in $\epsilon''(\omega)$) depends on temperature and often follows the Arrhenius law:

$$\omega_m(T) = \omega_{m,0}(T) \exp\left(-\frac{E_A}{k_B T}\right). \tag{1.51}$$

The same activation energy was ofter observed for the DC conductivity [71].

In this section we listed a number of various charge transport models commonly employed in CP. Obviously, the determination of the model for particular systems is a rather complex task.

1.4 Stability and aging of conducting polymers

Successful use of CP in applications requires the long-term stability of their properties, in particular electrical conductivity. It was found, however, that conducting polymers face aging and the conductivity decreases with time and number of studies have been carried out regarding natural or accelerate aging at elevated temperatures *e.g.* [81–93]. Interestingly, one order of magnitude decrease of conductivity in PPy after 20 years of storage at ambient conditions with only slight decay after 7 years was reported [91]. To compare stability of materials the half-life time $t_{0.5}$ defined as the aging time required for conductivity to be halved $\sigma(t_{0.5}) = \sigma_0/2$ is often used [81]. The conductivity decay is mostly expressed as exponential decay [82]:

$$\sigma(t) = \sigma_0 \exp\left(-\frac{t}{\tau}\right) \tag{1.52}$$

with the initial conductivity σ_0. The long-term aging is mostly simulated by elevated temperatures [81, 86]. In the limited temperature range, the relaxation time follows Arrhenius law:

$$\tau = \tau_0 \exp\left(-\frac{E_\mathrm{A}}{k_\mathrm{B}T}\right) \tag{1.53}$$

with the activation energy E_A and with the time-temperature shift one can obtain the so-called mastercurve [81, 87]. Moreover, one can estimate the long-term behavior such as half-life time at lower operating temperature (e.g. close to room temperature). One of the simplest, but not exclusive, explanation of such decay concerned increase of defects on polymer chains at constant rate with conductivity being determined by the rest unaffected chains [88]. A diffusion-like dependence of conductivity decay was also observed [83]:

$$\sigma(t) = \sigma_0 - K\sqrt{Dt} \tag{1.54}$$

with the diffusion coefficient D and some prefactor K. The change of conductivity was correlated with absorbed oxygen with temperature-dependent D and the prefactor given by the film thickness, $K = 4/l\sqrt{\pi}$ [84, 85]. Finally, when the GM model was assumed, the stretched exponential-decay was introduced [86]:

$$\sigma(t) = \sigma_0 \exp\left(-\frac{t}{\tau}\right)^{0.5} \tag{1.55}$$

where the exponent is given by the GM model with possible generalization to n [87]. In this model of aging the heterogeneous corrosion-like process of conducting islands disruption at expense of amorphous insulating phase was assumed [86].

The main chemical reasons were the dedoping due to covalent bonding of counterions to polymer backbone (*e.g.* chlorination), oxidation and chemical cross-linking (ternary amines in PANI) [88].

Besides study of DC conductivity the impedance spectroscopy was also found an excellent tool for probing aging [90, 92]. Alongside DC contribution in dielectric spectrum, a wide relaxation loss peak in ϵ'' was found with temperature dependent E_{A} for the frequency of its maximum, $f\mathrm{m}$ but different from that for σ_{DC}). The dielectric strength was about 10^3 and is inversely proportional to temperature, $\Delta\epsilon \sim 1/T$, and decreased with time [90]. Moreover, decrease of this AC contribution during aging was found about 100 times slower than DC conductivity. The polarization is generally associated with granular-like structure of PPy but its identification with a simple model for the MWS interfacial polarization was denied due to its independence on the size of conducting inclusions that were only considered to be changed during aging [90]. Lower number of transverse polarons due to aging can be cause of limited interchain (or intergrain) hopping and the associated loss peak decreased [92]. On the other hand, the relaxation peak associated with intrachain hopping was intensified due to aging-induced enhancement of intrachain localization [92].

When discussing stability, storage conditions are of great importance, since degradation of PPy was found to occur in ambient humid atmosphere (presence of oxygen and water) while in the inert one negligible degradation has been found [81]. In PANI thermal degradation dependent on the level of humidity showed a maximum for value $\approx$ 50% RH [89]. The stability of CP also depends on counterions and oxidation level, as reported for PPy films [81]. For PANI with oxygen-containing counterions, such as sulfates or sulfonates higher stability than for chlorides was observed [93].

Response of conductivity to change in ambient (pH, humidity) is another factor regarding their stability. It has been widely investigated that conductivity depends on water content and the its loss is often connected with decrease of conductivity [94–96]. It is believed that water in CP can be in various forms, such as free water, or bounded by one or two hydrogen bonds to the polymer backbone [94, 96, 97]. Recently, existence of nanodroplets was proposed based on atomistic simulations [97]. The discussion of the last three decades offers several explanations of conductivity-water relationship such as secondary doping [98], electron hopping assisted by proton exchange [99] or stabilization of protonated sites [100]. To our best knowledge the general agreement has not been achieved and this phenomenon still calls for more research. Next, it is well known that conducting polymers undergo (reversible) salt-base transition when immersed in alkaline medium. For PANI, emeraldine salt-base conversion is accompanied with the change of conductivity in 9 orders of magnitude [12]. In case of PPy, three orders of magnitude decrease of conductivity after immersion of granular PPy in 1 M NH_4OH was reported [101]. Generally, electrochemically prepared PPy films have been more investigated in respect to various oxidation levels [102–106]. As a mechanism of the conductivity loss, the covalent bonding of OH^- to polymer [102], dopant anion exchange with intercalated OH^- [103] or deprotonation

(reaction of OH^- and H^+ from PPy chain) [104] were proposed; moreover, in case of large polymer dopants, their neutralization by Na^+ was suggested [105]. Stability of conductivity when operating in ambient with high pH can be important in applications, particularly in biomedical applications [107]. Another application of deprotonated CP was reported for NaOH-treated PPy films which exhibited better sensitivity in infrared detection [106].

1.5 Outlook and applications

The current research in the field of CP is mostly devoted to characterization of individual objects on nanoscale for emerging nanoelectronics [108, 109], to composites with noble metals or inorganic semiconductors seeking synergistic effects [110, 111], to 3D structures such as conducting hydrogels [112]. In a theoretical direction, several alternative models for the charge transport properties have emerged, such as the band theory with traps included [113], and the electric field induced phonon-assisted tunneling [114] claimed to be superior to the prevailing VRH-like approach. Numerical simulations are being applied to bridge the microscopic and macroscopic properties of CP [100].

Conducting polymers exhibit some unique properties (or at least their combination) which make them attractive for industry. They can be prepared in semiconducting or metallic soluble form, they can be transparent, their E_F can be controlled over a wide range [1]. Besides electrical properties, response to external stimuli, ease of synthesis and processing, low cost and environmental stability can be listed as the main advantages of CP. All these can be valuable when thinking about applications, to name at least a few: chemical sensors, batteries, solar cells, anti-corrosive coatings, field effect transistors, *etc.* [1]. An optimistic view on their use in tissue engineering based on review of progress in the field has been recently published [115].

Particularly, use of CP as chemical sensors has been intensively studied. Their response, in particular change of electrical properties, is based either on chemical reactions (*e.g.* deprotonation) or on physical interactions (*e.g.* swelling); they can operate at room temperature, exhibit high sensitivity and short response time, and provide opportunity for easy device fabrication, on the other hand, they suffer from low selectivity, long-time instability and irreversibility [116]. As an example, PANI films on silicon microchips were used for ammonia sensing, with empirical equations for the time response and the dependence on the gas concentration [117]. Various models based on diffusion and reaction kinetics to describe the response can be found in literature, for instance, reviewed in Ref. [116]. However, confident determination of the underlying process can be problematic, since models based on chemisorption (Langmuir isotherm) and diffusion (with dual sorption process) provided equally good fit due to mimicking of exponential-like time response [118]. Recently, a bottom up multiscale strategy combining atomistic microscopic modeling with macroscopic diffusion and reaction processes has been proposed to explain PANI sensing mechanism [100]. Detailed overview of

this extensive field is however beyond the scope of this thesis. A short case study of PANI films reprotonated by sulfonic study for ammonia sensing is presented at the end of Chap. 4.

2. Experimental

2.1 Overview of experimental methods

In this section we list the commonly used experimental methods for DC and AC conductivity measurements. They concern two and four probe methods, with various arrangement of electrodes. The list is not meant to be exhaustive, more details can be found in specified books, e.g. [119,120]. Some of the methods were used for our measurements and the experimental apparatuses will follow in the next section. Typical configurations for experiments carried out for this thesis on bar-shaped sample (or thin film) and pellet with various electrode positions are shown at Fig. 2.1.

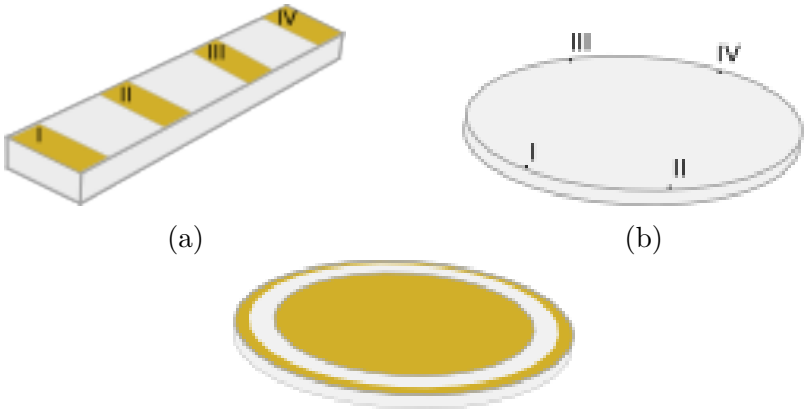

(a) (b)

(c)

Figure 2.1: Typical configurations for two and four probe techniques. A bar-shaped sample with four gold electrodes (a), a pellet with four point probes at circumference (b), a pellet with gold electrodes from bottom and top side and a guarding ring at the top circumference (c).

2.1.1 DC methods

In order to avoid misleading and incorrect interpretation of charge transport properties, the experimental method should be selected carefully. Real measurements of conductivity always consist of current I and voltage U measurements and their recalculation regarding the specific geometry, in the simple case using Eq. (1.2). Several techniques can be find, each with its pros and cons, which should be considered when designing experiment.

The two-point probe method belongs to the simplest methods since only two probes attached to sample are needed for measurement. Each of them serves as both, a voltage probe and a current probe. The price for its simplicity is the presence of parasitic resistances. With this method the total resistance R_{tot} is

measured [119]:

$$R_{\mathrm{tot}} = \frac{U}{I} = 2R_p + 2R_c + 2R_{sp} + R_s \tag{2.1}$$

which consist of the probe resistance R_{p}, the contact resistance R_{c} at the probe-sample contact, the spreading resistance R_{sp} when current flows from a small metal probe into the sample (and *vice versa*), and, finally, the sample resistance R_{s}. This method thus contains three parasitic resistances with only R_{c} easily separable by measurement at shorted probes. The rest of them remains unknown and should be considered when interpreting the results. When the resistivity of material is high and such errors can be neglected, two-terminal measurement can be conducted, for instance using two larger electrodes from bottom and top sides (sandwich configuration) as depicted at Fig. 2.1c and applying constant voltage. However, since resistivity of sample is high, errors due to electrostatic interference should be avoided placing sample into shielded test fixture [121]. Moreover, surrounding guarding ring around top electrode held on the same potential can prevent surface current leakage [122]. The configuration with guarding ring can be used for both, bulk and surface resistivity measurements [121].

An elegant way for the parasitic resistances elimination is the four probe method with two current probes separated to two voltage probes. The parasitic resistances are negligible for voltage probes due to flow of only small currents during voltage measurement. A standard geometry can be bar-shaped sample usually used also for Hall effect measurements (Fig. 2.1). The current enters and leaves the sample from electrodes 1 and 4 while voltage drop is measured between electrodes 2 and 3. The particular four parallel stripes reflect the real configuration used in our experiments. Generally, voltage probes can employed as contacts on side arms to minimize their effect on current lines [123] or current can be applied from electrodes placed on the left side and the right side of sample instead of the top one [124]. This method has wide application, *e.g.* in semiconductors [123] or metal [125] characterization, however its disadvantage is necessity for precise geometry and knowledge of all dimensions with high accuracy. Other techniques thus have been developed. One of them is the collinear configuration of four point probes from the top of sample. For the arbitrarily shaped sample with the finite dimensions and the equidistant spacing s between the probes, the resistivity can be written in the form [119]:

$$\rho = \frac{1}{\sigma} = 2\pi s \frac{U}{I} F, \tag{2.2}$$

with the correction factor Fconcerning the sample geometry, its thickness, and the probes' (mis)locations. The condition for much smaller thickness than spacing should be fulfilled for its independent determination. Possible problems with collinear placing can be bypassed with point probes at sample's circumference (Fig. 2.1) in the so-called van der Pauw configuration (vdP). Based on conformal mapping it was shown that for an arbitrary shaped sample the resistivity can be determined easily when the sufficiently small contacts are placed at circumference provided that the sample is uniform in thickness h and is singly connected [126]:

$$\rho = \frac{\pi h (R_{12,34} + R_{23,41})}{2\ln(2)} F\left(\frac{R_{12,34}}{R_{23,41}}\right), \tag{2.3}$$

where $R_{12,34}$ is the resistance measured when the current enters the sample at contact 1 and leaves at contact 2 and the voltage is measured between the contacts 3 and 4 (rotated for $R_{23,41}$), and correction factor F depending only on ratio of $R_{12,34}/R_{12,34}$. For the correction factor, the implicit equation has to be solved:

$$\frac{R_{12,34}/R_{12,34}-1}{R_{12,34}/R_{12,34}+1}=\frac{F}{\ln(2)}\operatorname{arccosh}\left[\frac{\exp(\ln(2)/F)}{2}\right]. \tag{2.4}$$

Obviously, for symmetrical $R_{12,34}$ and $R_{23,41}$, it reduced to 1. Similarly to collinear configuration, the displacement of contacts from circumference introduces an error [126]. This method was later adopted also for resistivity anisotropy measurements [127]. In general, the vdP method has been widely used thanks to mentioned advantages over conventional method requiring bar-shaped samples, to mention at least two particular cases, in laboratory high temperature (at 600 °C) measurements of resistivity and Hall coefficient [124] and for large scale measurements of aluminum alloys for aircraft manufacture [125].

Besides errors due to contacts displacement, additional source of uncertainty is the Joule heating of a sample due to the current flow and the minority/majority carriers injection. The parasitic thermoelectric voltage can accompany possible temperature inhomogeneity in sample [119]. In the case of poorly conducting materials (σ <10^{-7} S cm^{-1}), the leakage currents as the source of errors could be eliminated using guarding approach with unity gain buffers and a differential measurement [121, 128], electrostatic interference could be shielded by placing sample into a metallic box and the low noise shielded coax and triax cabling should be used [121].

To conclude, measurement of resistivity could seem as easy to perform, however, when high accuracy is desired, a lot of precautions have to be made.

2.1.2 AC methods

As mentioned in previous chapter, the AC measurements can bring additional information about the charge transport mechanism. In principle, the complex dielectric function as the property of interest can be measured by impedance Z spectroscopy in a very wide frequency range, 10^{-6} Hz–10^{12} Hz, but several techniques have to be employed [129]. The midterm range 10^{-6} Hz–10^{7} Hz can be achieved with the lumped circuit methods, where sample is represented as serial or parallel circuit of resistor and capacitor, being limited by device (impedance bridges) or at least by enormous experimental time at low frequencies (dielectric converters with Fourier correlation analysis) and by the geometrical restriction of sample capacitor alongside with the parasitic impedances caused by cabling at high frequencies. The former limit can be overcome within the time domain measurements (*e.g.* time dependence of the DC polarization current) followed by the Fourier transformation, and the later by distributed circuit methods (waveguide and cavity techniques) 10^{-7} Hz–10^{11} Hz or latter by quasi-optical and optical methods. The mid-term frequency range is of the prime interest here.

Using the lumped circuit methods the sample forms a capacitor with complex capacity $C^*(\omega)$, and within the linear response on harmonic electric field the dielectric function $\epsilon^*(\omega)$ is calculated from the complex impedance $Z_s^*(\omega)$ of sample: [129]

$$\epsilon^*(\omega) = \frac{C^*(\omega)}{C_0} = \frac{1}{i\omega Z_s^*(\omega) C_0}, \tag{2.5}$$

with C_0 being the vacuum capacitance of the particular experimental arrangement. The complex impedance can be obtained from impedance analysis using an AC impedance bridge where two currents are balanced. The current flowing through the sample $I_s^*(\omega)$ generated by $U_s^*(\omega)$ on one side and the compensating current $I_c^*(\omega)$ generated by the variable amplitude-phase generator $U_c^*(\omega)$ through the compensation impedance $Z_c^*(\omega)$ on the other side. Then $Z_s^*(\omega)$ can be expressed as:

$$Z_s^*(\omega) = \frac{U_s^*(\omega)}{I_s^*(\omega)} = -\frac{U_s^*(\omega)}{U_c^*(\omega)} Z_c^*(\omega). \tag{2.6}$$

Alternatively, the Fourier correlation analysis where applied voltage $U_1(t)$ and measured voltage $U_2(t)$ are analyzed by means of their Fourier base waves (both phase and amplitude) given by two sine wave correlators. This method provides very precise measurements, since the noise is averaged out and $Z_s^*(\omega)$ is given:

$$Z_s^*(\omega) = \frac{U_s^*(\omega)}{I_s^*(\omega)} = R\left(\frac{U_1^*(\omega)}{U_2^*(\omega)} - 1\right), \tag{2.7}$$

where resistor R converts current $I_s(t)$ to voltage $U_2(t)$. This is usually combined with some broadband current to voltage converter (*e.g.* a electrometer amplifier with variable gain) which replaces the resistor R and as a whole it is generally integrated into commercially available dielectric analyzers. The advantage of the impedance bridge besides price is the lower measurement time but it is overwhelmed by the dielectric analyzer in frequency range and precision [129].

2.2 Samples

Samples for conductivity measurements were prepared either in the bulk form of compressed pellets (at load 7 kN) of 13 mm in diameter and thickness about 1 mm which were occasionally cut to bar-shaped samples wit dimensions about $5 \times 2 \times 1$ mm, or in the form of thin films approximately 100 nm thick[1]. All materials studied here were based on PPy or PANI. The short description of their synthesis follows with the notation used throughout the text. Besides chemical structure, the morphology of CP is an important factor which determines electrical properties. Throughout the text several representatives of globular and nanotubular form, polymer-silver composites and thin films are presented[2].

[1] All samples were synthesized by several colleagues at collaborating institutions—IMC AS CR and UCT in Prague.

[2] Images were obtained again by several colleagues at different institutions: IMC AS CR, UCT Prague, CU FMP and NTUA.

One of the key material presented here is PPy in form of nanotubes (PPy-NT). It was prepared at 5 °C by oxidation of pyrrole monomer with iron(III) chloride ($FeCl_3$) hexahydrate in presence of Methyl Orange (MO) as a structure-guiding agent in the 'standard' molar monomer:oxidant:MO ratio being 1:1:0.05. More details about synthesis and the mechanism of nanotubes formation can be found elsewhere, for our samples in Ref. [130]. This is the starting point for various derivatives and comparison of their properties. For instance, other oxidants such as iron(III) sulfate hydrate ($Fe_2(SO_4)_3$), ammonium peroxydisulfate (APS) were used (PPy-NT-oxidant with or without use of MO when globular morphology was obtained (PPy-G-oxidant) [131]. The influence of MO molar concentration within range 0.44 to 22 mM on electrical properties of PPy-NT-$FeCl_3$ was studied as extension of preliminary results [130]. Except MO, other azo dyes such as Sunset Yellow (SY), Acid Red (AR) and Orange G (OG) were used as templates in continuity to previous study [132]. Since ability of PPy to reduce silver nitrate ($AgNO_3$) to metallic silver was reported [133], the next work was focused on single-step PPy-silver composites (PPy-Ag) synthesis where oxidant $FeCl_3$ was replaced with $AgNO_3$ for polymerization and monomer:oxidant:MO ratio was varied 1:1:0–0.1 (PPy-Ag-e) and 1:2.5:0–0.2 (PPy-Ag-s) with subsequent variation in both components' morphology [134]. Finally, the effect of PPy-NT-$FeCl_3$ deprotonation in NH_4OH or NaOH solutions of various molar concentration was studied inspired by unexpected stability of conductivity when immersed in excess of in 1 M (1 mol l^{-1}) NH_4OH was used [133].

The second group of samples is based on PANI. As the 'standard' is considered globular PANI prepared at room temperature by oxidation of aniline hydrochloride with APS in presence of 1 M solution of hydrochloric acid (HCl), PANI-G-APS(HCl) [12, 135].As an alternative, methanesulfonic acid (MSA) was used instead of HCl, PANI-G-APS(MSA). Interestingly, nanotubular form, PANI-NT-APS(Suc), was obtained when weak doping acid, such as succinic acid (Suc) [136]. The effect of polymerization temperature T_p from −20 °C to 40 °C in case of 'standard' PANI was examined. Samples PANI-G-APS-T_p were prepared by the polymerization of aniline hydrochloride with APS in a vessel placed in bath kept at constant temperature. Only for solid state polymerization at −20 °C the reaction mixture at 0 °C was immersed in liquid nitrogen and subsequently placed in freezer. An effect non-thermostated bath was studied at 20 °C, denoted as 20-N [137]. The standard procedure was applied in thin films synthesis with subsequent convertion to base form [12] and reprotonation with various sulfonic acids such as MSA, dodecylbenzenesulfonic acid (DBSA), poly(4-styrenesulfonic acid) (PSSA), poly(2-acrylamido-2-methyl-1-propanesulfonic acid) (PAPMSA) and phtalocyaninesulfonic acid (FCA). The selection of sulfonic acids was related to observed higher stability of reprotonated samples [93]. In powder form, DBSA was also used after reprotonation, PANI-G-APS(DBSA). Besides widely used APS oxidant, $FeCl_3$ was also used together with MSA as co-dopant at various molar concentration from 0 to 1 M. Finally PANI-silver composites (PANI-Ag) were studied in salt and base form, particularly with variable silver content achieved when various molar ratios of APS and $AgNO_3$ was used [138].

2.3 Experimental conditions

Due to range of studied materials in various forms measurements were based on various methods and experimental apparatuses. In the following several experimental procedures, protocol and set ups are described.

Experimental methods and apparatuses used for measurements of DC conductivity can be listed in following way:

- The four-point probe method in the vdP configuration was used for compressed pellets or thin films using various devices. Good ohmic contacts were achieved by mechanically pressed wires (alloy of platinum and rhodium). The following apparatuses were employed:

  ⋆ The apparatus A-I was composed from a Keithley 237 High Voltage Source Unit, a Keithley 2010 Multimeter as a voltmeter equipped with a 2000-SCAN 10 Channel Scanner Card for contacts commutations. This construction operated well for samples with conductivity within range $10^{-5}\,\mathrm{S\,cm^{-1}}$–$10^{3}\,\mathrm{S\,cm^{-1}}$. The upper limit was imposed by the current limit about 100 mA for point contacts to avoid damaging Joule heating. The lower limit was overcome with apparatus A-II.

  ⋆ The apparatus A-II was composed from two Keithley 6517 Electrometers with high input resistance, a Keithley 6220 Precision Current Source and Keithley 7001 Switch system equipped with a Keithley 7152 Matrix Card and the differential measurements had to be used (Sec. 2.1). The voltage on each voltage probe was measured by electrometers and their difference was additionally measured by a Keithley 2000 Multimeter. The input current was measured with a Keithley 6485 Picoammeter. Samples were place in a metallic box and cabling based on triax and coax cables was used. The limit was thus lowered down to about $10^{-9}\,\mathrm{S\,cm^{-1}}$ but measurement time increased.

  ⋆ Some measurements (with upper limit of 2 MΩ) were done using A-III which was simply a Lake Shore 370 AC Resistance Bridge embedded in a commercial device Physical Properties Measurement System 9 (PPMS9) from Quantum Design.

  ⋆ Alternatively to A-I, different equipments were used for specific experiments, such as A-IV composed from Keithley 220 Programmable Current Source, a Keithley 2010 Multimeter, and a Keithley 705 Scanner equipped with a Keithley 7052 Matrix Card and used for room temperature conductivity, σ_{RT}, measurements, A-V composed from a Keithley 6220 Precision Current Source, a Keithley 2182A Nanovoltmeter and a Keithley 7002 Switch System equipped with a Keithley 7011-S Quad 1×10 Multiplexer Cards used at mid-temperature aging experiments, and finally, A-VI composed from a Keithley 238 High

Current Source Unit, and a Solartron Schlumberger 7081 Precision Volmeter and a Keithley 706 Switch with for high-temperature aging measurements.

- The four probe method with evaporated linear parallel gold electrodes used for bar-shaped samples or thin films. In the former case, previously mentioned apparatuses were used, in the the latter case it was employed in a sensor testing and A-VII was used containing a Keithley 2182A Current Source and a Keithley 6220 Multimeter. The used of bar-shaped method suffered mainly from imperfect geometry of not parallel sides and the required precise knowledge of all dimensions. Moreover, gold electrodes were evaporated on samples which could damage surface layers of material.

- The probe measurements with two parallel gold electrodes employed for sensor measurements with either A-VI or a Keithley 6517 Electrometer. Highly resistive pellets such as PANI bases (with circular gold electrodes and optionally with a guarding ring were measured with a Keithley 6517A Electrometer, Fig. 2.1c) but A-II which allowed the vdP method was preferred whenever possible.

Measurement of AC conductivity was performed with a Novocontrol Dielectric α-analyzer within broad frequency range 10^{-2} Hz–10^{6} Hz and coaxial cabling on pellets with gold electrodes (evaporated or sputtered) occasionally with a guarding ring (meant mostly of DC measurements). Due to the ring spacing of about 1 mm kept at a floating potential during measurements, the absolute values of ϵ^* could not be precisely determined using simple Eq. (1.5). Since relative values are not changed, the error in absolute values is not of great importance.

Alongside conductivity measurements for specific experiments, ambient conditions (temperature, pressure, atmosphere) had to be modified. The following list of 'auxiliary' devices can be listed:

- Measurements in the high temperatures (HT) region 70–318 K were performed in a Janis Research VNF-100 cryostat and flowing stream of nitrogen vapor (with pumping at the low temperature end), noted as T-I. Temperature was controlled by a Lake Shore 332 Temperature Controller. The limited range 123–313 K was also available using a cryostat with nitrogen flow controlled by a Quatro system embedded in a Novocontrol dielectric analyzer, T-II.

- The low temperature (LT) region 4–70 K (but routinely extended to 318 K) was achieved in a helium cryostat embedded in a PPMS9 integrated system, T-III. This equipment allowed magnetoresistance measurements in magnetic fields up to 9 T using superconducting coils.

- Aging at elevated temperatures 32–80 °C was studied in a slightly modified Janis cryostat at ambient atmosphere with temperature controlled by a Lake Shore 330 Temperature Controller, T-IV.

- High temperature aging measurements within range 100–140 °C were performed in a Heraeus Vötsch oven with temperature measured with a Keithley 195A digital multimeter.

Prior to temperature scans in T-I and T-III, samples were placed in continuously pumped cryostat (dynamic vacuum) for approximately 8 hours at pressure below 10 Pa or about 100 Pa, respectively, in order to remove moisture.

Usually, T-I was connected with A-I, T-II was directly embedded in a dielectric analyzer, and T-III was combined with A-II or A-III according to sample conductivity. Accelerated aging tests were performed with combination of T-IV and A-V or T-V and A-VI. This modular-like approach gives an advantage of potential modification or extension of experiments when connected with appropriate sample holders and wiring. All experiments were to a certain point automated with controlling software.[3] In case of sensor testing[4], A-VII or Keithley 6517B Electometer were combined with a sample chamber connected to a Bronkhorst liquid flow meter and controller, and mixing system where desired ammonia concentration was prepared in mixing with dry nitrogen. Continuous gas flow was used and the chamber was not tempered. More details can be found in Ref. [139].

[3]Dr. J. Prokeš and Assoc. Prof. I. Křivka are fully acknowledged as the key persons behind of majority of experimental arrangement.

[4]The support of Greek colleagues from NTUA is acknowledged.

3. Effects of various synthesis conditions on charge transport

This chapter is focused on the study of charge transport in conjugated polymers—PANI, PPy and their composites with silver. All these materials were prepared by chemical polymerization at various conditions such as various oxidants, dopants, polymerization temperatures, and templates. The effect of these variations in synthesis on charge transport is discussed here.

We focus mainly on conducting polymers forming nanotubes which are generally promising due to the better order in 1D structures [17,140] and composites of polymer with silver which are easy to prepare at reasonable cost and we can benefit from both components [110]. In order to go step further in functional design of materials, understanding of final properties originating from various synthesis conditions and processing is crucial. This point is discussed as well. In the case of PANI differences between thin films and bulk material in form of compressed pellets are presented as well.

It is essential to note that conductivity as the property of our prime interest is almost exclusively discussed here. However, sa much as possible it should be correlated with measurements of other properties such as morphology (SEM), optical (Raman and FTIR) spectra, crystallinity (WAXS), thermogravimetric measurements (TGA) *etc.* This supplementary material, except few micrographs, is not included in thesis. Some results can be found in already published papers, others (mostly in preliminary stage) are based on personal communications only.

The chapter is composed from three sections. First one is focused on effect of oxidants and dopant on charge tranport for PANI and PPy. The following section is built up on previous results and discuss more subtle factors such as polymerization temperature, type and concentration of template. The last one is dedicated to polymer-silver composites. A short summary is included at the end of each section.

3.1 Effect of oxidants and dopants

Prior to examination of oxidant and dopant effects on conductivity, short introduction to the data analysis is presented in order to build a basic framework for the later discussion. Majority of samples studied in this thesis, with an exception of some composites with high content of silver, exhibited semiconducting behavior mostly in a kind of stretched-exponential dependence (at least in the limited temperature range). In Chap. 1 we have already listed several models conventionally used to fit the data. The analysis of $\sigma(T)$ and $W(T)$ was generally done applying following models:

- Single model in a whole temperature range—it was only rarely found since temperature can overcome the effect of the charging energy as a limit of tunneling (the CELT model), Eq. (1.37), or decrease the optimal hopping distance to the nearest neighbors only (the VRH model), Eq. (1.17); this approach was usually not consistent with $W(T)$.

- Various models valid for temperature sub-intervals—expected from reasons mentioned above, one model was subsequently replaced by another one; however, there usually existed region where none of the models was satisfactory.

- Resistors (representing divers models) connected in series or parallel—assumed existence of two (or more) contributions alongside due to the inherent heterogeneous structure of CP [141]; and the complicated form of $W(T)$ could be explained within this framework [131]. Total conductivity is given by Eq. (1.45) or its parallel form or even their combination. Total $W(T)$ can be obtained easily by application of Eq. (1.23) to the total resistivity, with assumption of the temperature-independent geometrical factors f_i. For N resistors in series one obtains:

$$W(T) = \frac{\sum_{i=1}^{N} W_i f_i \rho_i}{\sum_{i=1}^{N} f_i \rho_i}, \tag{3.1}$$

  or in case of N resistors in parallel:

$$W(T) = \frac{\sum_{i=1}^{N} W_i \sigma_i / f_i}{\sum_{i=1}^{N} \sigma_i / f_i}. \tag{3.2}$$

  Explicit forms for the models used throughout the work are not presented since their derivation from individual components is straightforward. For brevity, in the rest of thesis geometrical factors are implicitly included in fitted pre-exponential factors σ_0 ($\sigma_i / f_i \to \sigma_i$). This unification could be used for explanation of the particular values obtained from the data analysis [23, 131].

Notations for the theoretical models are based on their abbreviation for single models or using conjunctions '-and-' for the serial connection and '-or-' for the parallel connection. For instance, notation MET-and-(CELT-or-ARH) has the meaning of resistor MET, Eq. (1.11), in series with the second one composed from two resistors, Eq. (1.14) with exponent 0.5 and 1, in parallel (Fig. **??**).

After fitting of the selected models to experimental data we applied the following criteria to check the consistency of obtained parameters:

- In the VRH model with increasing temperature more distant hops become less probable; hence, we have a high temperature limit for validity of VRH,

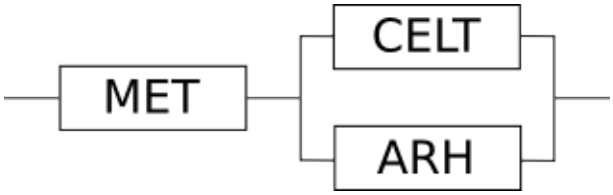

Figure 3.1: Schematic representation of the MET-and-(CELT-or-ARH) model.

particularly conditions $R_{\mathrm{hop}}/\xi > 1$ and $W_{\mathrm{hop}} > k_{\mathrm{B}}T$ have to be fulfilled. This validation can be used provided that the localization length ξ and the density of states $g(E_{\mathrm{F}})$ are known (Eq. (1.17) and Eq. (1.18)).

- In the CELT model transport of charge carriers is limited by the charging energy E_{c}, Eq. (1.37), which is supposed to be higher than the thermal energy $k_{\mathrm{B}}T$. And the optimal polaronic cluster diameter for tunneling [60]:

$$\frac{d}{a} = \frac{1}{4s/d}\left(\frac{T_0^{\mathrm{C}}}{T}\right)^{0.5}, \tag{3.3}$$

  with small clusters being important at high temperatures and large clusters contribution mainly at low temperatures. It should be noted that the approach based on s/d relationship was criticized and claimed incorrect based on the EMA calculations [61]. In order to get at least some insight into systems this former model (alongside with the exponent 0.5) was still considered in spite of its questionable validity.

- For the FIT model in the parabolic barrier approximation, Eq. (1.39), the approach in Ref. [142] was followed. In particular, a quadratic form of $g(\lambda)$, Eq. (1.43), was substituted into Eq. (1.41) in order to obtain an equation for the width of potential barrier w: [131]

$$w^2 - w\left(\nu\left((8-\pi) + \frac{T_1^{\mathrm{F}}}{2T_0^{\mathrm{F}}\chi}\right)\right) + 4\nu^2(4-\pi) = 0, \tag{3.4}$$

  where $\nu \equiv \lambda w = \frac{0.795e^2}{16\pi\epsilon_0\epsilon_{\mathrm{r}}V_0}$ and $\chi \equiv \sqrt{\frac{2m*V_0}{\hbar^2}}$. Next, for known V_0, $m*$ and ϵ_{r} the area of junction A could be obtained from Eq.(1.40) with the right-hand side multiplied by the factor $\frac{0.795+1.64\lambda-19.28\lambda^2}{4\lambda}$ [142]. Finally, the consistency check for the image forced correction parameter using Eq.(1.42) could be performed, $0.1 - 0.15 < \lambda < 0.25$.

Unfortunately, for such validity tests several assumptions had to be made on *a priori* unknown but required physical variables. Their real values in principle could have been be taken from various additional measurements such as magnetoresistance, electric field dependence, or structural investigations but in most cases it was not possible. This section is dedicated to the study of the effects of various oxidants and dopants on charge transport. These two modifications during synthesis belong to the most important ones since they offer variability of final products taking into consideration a number of available organic/inorganic acids. The overview of samples' synthesis description has been already given

in Chap. 2. They were prepared mostly in form of powders compressed thereafter into pellets with manual hydraulic press under *ca.* 540 MPa after couple of minutes. It should be noted here that granular PPy was rarely successfully compressed into the compact pellet and as such its investigation was often very limited. Occasionally, PANI thin films were studied (*e.g.* meant for gas sensing applications).

For the same material conductivity usually varied from sample to sample mainly due to I) various batches with not perfectly equal synthesis conditions, differences in post-synthesis treatment procedures (drying, washing in ethanol, acetone), *etc.* causing uncertainty within several % and II) various age of samples in the moment of measurement (this point is discussed in Sec. **??**). Particularly, the last one is important since during first few days after synthesis (and mainly after compression to pellet), decrease of conductivity of about 10 % can occur. Hence, it is important to keep this in mind whenever one goes throughout literature and checks the data. This issue reflects general disadvantage of chemical synthesis in terms of reproducibility—it contains a lot of subtle steps during synthesis/processing which are not (cannot be) fully under control but which can be reflected in the final properties of CP. Finally, measurements of σ_{RT} were conducted at ambient temperature which varied withing several degrees.

Conductivity of studied samples covers about 9 decades from poorly conducting PPy-NT-$FeCl_3$ bases, $10^{-5}\,S\,cm^{-1}$, to highly conducting PPy-Ag composites $10^{3}\,S\,cm^{-1}$, dependent on oxidant, doping level, morphology, presence of silver, *etc.* (Fig. 3.2) In this section the attention is paid on influence of oxidant and dopant, the rest of samples are investigated in following sections.

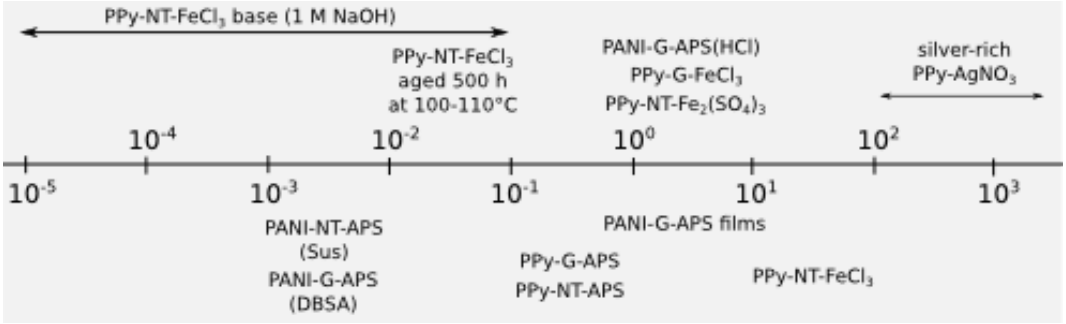

Figure 3.2: Example of σ_{RT} for various studied systems; PPy-NT and PPy-G with various oxidants [131], deprotonated PPy-NT-$FeCl_3$, silver-rich PPy-$AgNO_3$, PANI-NT(Suc), 'standard' PANI-G-APS(HCl) and reprotonated films with various sulfonic acids, PANI-G-APS(DBSA).

In case of PPy-NT other oxidants that $FeCl_3$ resulted in less conducting nanotubular samples, similar to their granular counterparts. It was suggested to be due to lower protonation level and its higher heterogeneity according to results from Raman and FTIR spectroscopies [131]. The self-assembly grown PANI-NT-APS(Sus) required weak acidic solution comparing to PANI-G-APS(HCl) [21]. Reprotonation of PANI-G-APS with DBSA resulted in decrease of conductivity.

On the other hand PANI-G-APS films[1] reprotonated with various sulfonic acids exhibit similar level of conductivity as the initial sample. In general, PANI reprotonation with sulfonic acids was found useful for their stabilization even for the price of lower conductivity [93]. The charge transport mechanism is of the main interest in this section, particularly the effect of various oxidants and dopants. We emphasize that values of fitted parameters serve only for rough orientation due to the same sources of uncertainty as mentioned for σ_{RT}. Results are presented separately for PPy pellets, PANI pellets and PANI films.

3.1.1 Polypyrrole

In case of PPy, attention is turned to PPy-NT as the promising material due to high conductivity and its stability (Chap. 4) comparing to its globular counterpart. We can consider PPy-NT-$FeCl_3$ as a kind of 'standard' since $FeCl_3$ is common oxidant for pyrrole [143–145]. There has been considerable interest in this nanotubular form of PPy [109, 146]. The analysis for PPy samples, except PPy-NT-$AgNO_3$, has been recently published [131]; hence, it is mostly only rephrased here. We evaluated $\sigma(T)$ and $W(T)$ data (Fig 3.3) according to I) several models that subsequently replace each other, VRH, PL and ARH II) sum of various model such as the VRH-and-PL model and the CELT-or-ARH model. Results are summarized in Table 3.1 and Table 3.2. Parameters obtained from the HT (high temperature) data were generally less trustworthy. Unfortunately, the LT (low temperature) data were not always available. Except PPy-NT-$FeCl_3$ none of the others PPy exhibits the exponent 0.25 typical for Mott 3D VRH and in the following charge transport in PPy-NT-$FeCl_3$ is analyzed separately to others as done in Ref. [131].

Since the slope in the double-logarithmic plot $W(T)$ is continuously changing (Fig. 3.3), a single mechanism which covers the whole temperature range can be ruled out except the FIT model. In such case a maximum is expected at T_1^{F}. For PPy-NT-$FeCl_3$ it can be ruled out but for the second group data at T_1^{F} were not available, however its satisfactory fit to only the limited temperature range witnessed against it. Despite, we believe it is instructive to estimate physical parameters of the FIT model from fitted parameters (Table 3.1) and check their consistency and relevance. According to the mentioned approach we obtained $V_0 < 0.1\,\mathrm{eV}$ and subsequently $w \sim 20\,\mathrm{nm}$ when λ was desired to remain consistent and values $0.1\,m_{\mathrm{e}}$ and 2.5 were used for effective mass m^* and dielectric constant ϵ_{r}, respectively, to model the junction [142]. Such small barrier height and large width are unreal and the FIT model is indeed unable to explain transport in our PPy samples. Next options are either several mechanisms of VRH and PL valid only within certain temperature range or a combination of at least two of them as resistances in series/parallel connection.

According to best fit results, charge transport in PPy-NT-$FeCl_3$ can be inter-

[1] These values are rather rough estimation based on the assumption of the uniform thickness of 100 nm.

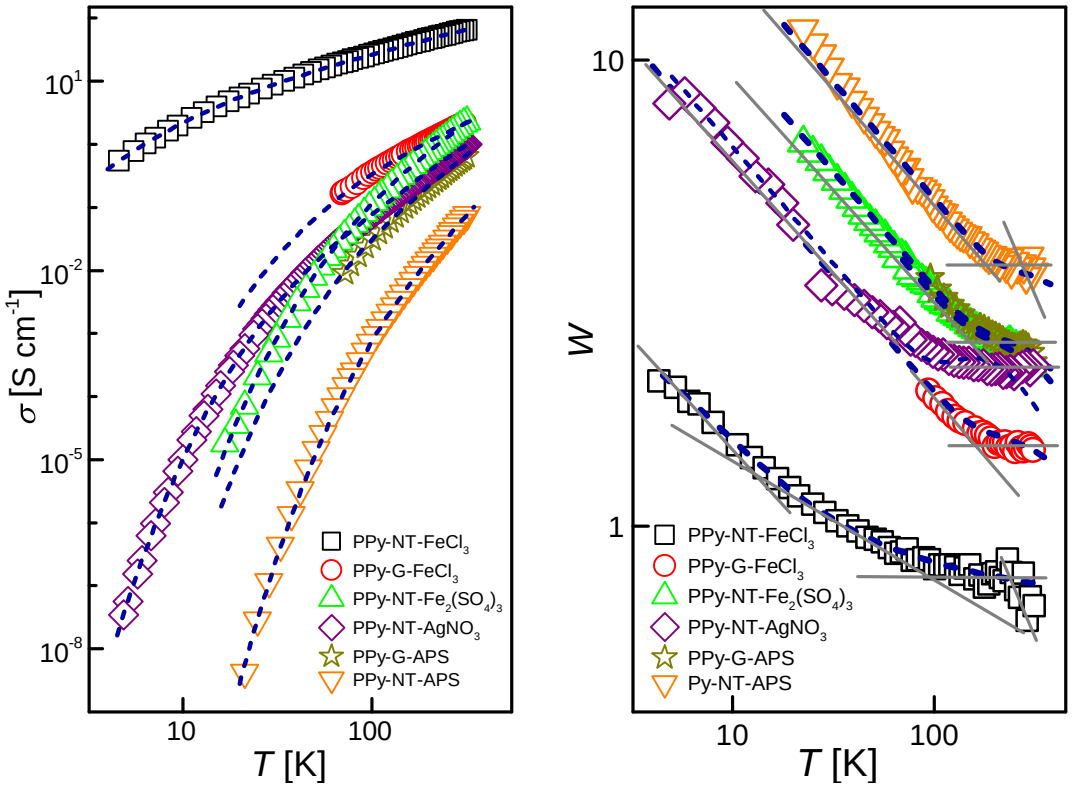

Figure 3.3: Experimental data for $\sigma(T)$ (left) and $W(T)$ (right) and best fits (see text) for PPy samples of various morphology and oxidants used. Lines are guides for single models. Adapted from Ref. [131] except PPy-NT-$AgNO_3$.

sample	σ_{RT} [S cm^{-1}]	range [K]	σ_0 [S cm^{-1}]	T_0 [K]	n	range [K]	a [S cm^{-1} K$^{-\gamma}$]	γ	range [K]	σ_0 [S cm^{-1}]	T_0 [K]	T_1 [K]
PPy-NT-$FeCl_3$	66	4–20	46	92	0.5	80–300	0.7	0.8	4–35	42	60	10
		10–100	600	9300	0.25							
		250–318	122	198	1							
PPy-NT-$Fe_2(SO_4)_3$	4.8	18–115	57	3900	0.5	140–318	1.5×10^{-6}	2.5	16–140	3	380	14
		220–318	16	630	1							
PPy-NT-APS	0.2	30–170	15	9800	0.5	120–318	2.2×10^{-11}	3.8	8–140	0.2	630	15
		220–318	2	980	1							
PPy-NT-$AgNO_3$	0.8	6.6–200	7	1900	0.5	50–318	2×10^{-6}	2.3	6.6–60	0.3	170	6
		250–300	6.9	610	1							
PPy-G-$FeCl_3$	4.2	77–180	17	1500	0.5	130–318	3.8×10^{-4}	1.5	77–280	9	560	71
		250–318	8	410	1							
PPy-G-APS	0.5	77–180	22	4400	0.5	150–318	3.9×10^{-7}	2.5	77–240	6	850	62
		250–318	5	650	1							

Table 3.1: Room temperature conductivity and fit results according to single models represented by Eq.(1.14),(1.12) and (1.39) for PPy of granular and nanotubular morphology synthesized with various oxidants. Except PPy-NT-$AgNO_3$ adopted from Ref. [131].

preted as a smooth transition from ES to Mott 3D VRH at low temperatures (smooth change of exponent from 0.5 to 0.25). This is either replaced by the PL model and the ARH model at higher temperatures or, preferably, it is connected in series with PL with exponent 0.74 (Table 3.2). The latter scenario seems reasonable when explained as alternating regions of well doped and ordered phase in critical state approaching MIT from insulating side (PL) and

more disordered regions where 3D VRH governs transport. An equally good fit was obtained without ES VRH. Combining this picture with positive quadratic MR dependence (Fig. 3.4), values for the localization length ξ and the density of states $g(E_F)$ were obtained. It seems that the weak-field regime ($L_B(6\,T)$ at 10 nm) could still be used as a good approximation as it was suggested to be valid well beyond the value of the crossover B_c [52]. With decrease of positive MR magnitude caused by higher temperature (about 15 K) a small (linear) negative MR contribution became visible. This contribution can be due to regions near MIT [15]. On the other hand, in single nanotubes in contrary to pellets, the contribution of negative MR was not observed, they exhibited only very weak positive MR and interfibrilar contacts were assumed to control MR [109, 146].

sample	model	σ_0 [S cm^{-1}]	T_0 [K]	n	a [S cm^{-1} K$^{-\gamma}$]	γ	σ_0 [S cm^{-1}]	T_0 [K]	n
PPy-NT-$FeCl_3$	ES/Mott-VRH-and-PL	83	114	0.5	1.7	0.74			
	ES/Mott-VRH-and-PL	2500	2.05×10^3	0.25	1.7	0.74			
	Mott-VRH-and-PL	6400	3.35×10^3	0.25	1.7	0.74			
PPy-NT-$Fe_2(SO_4)_3$	CELT-and-PL	103	4300	0.5	3.1×10^{-7}	3.0			
	CELT-or-ARH	58	3900	0.5			22	1200	1
PPy-NT-APS	CELT-and-PL	45	1.13×10^4	0.5	4.8×10^{-11}	3.9			
	CELT-or-ARH	18	1.02×10^4	0.5			7	2000	1
PPy-NT-$AgNO_3$	CELT-and-PL	13	1900	0.5	4.2×10^{-7}	2.8			
	CELT-or-ARH	4.5	1700	0.5			5.4	740	1
PPy-G-$FeCl_3$	CELT-and-PL	53	2000	0.5	7.9×10^{-4}	1.5			
	CELT-or-ARH	16	1500	0.5			9	1000	1
PPy-G-APS	CELT-and-PL	83	5500	0.5	7.1×10^{-7}	2.5			
	CELT-or-ARH	20	4200	0.5			9	1300	1

Table 3.2: Fit results according to the ES/Mott-VRH-and-PL model, the CELT-and-PL model or the CELT-or-ARH for PPy of granular and nanotubular morphology synthesized with various oxidants. Except PPy-NT-$AgNO_3$ adopted from Ref. [131].

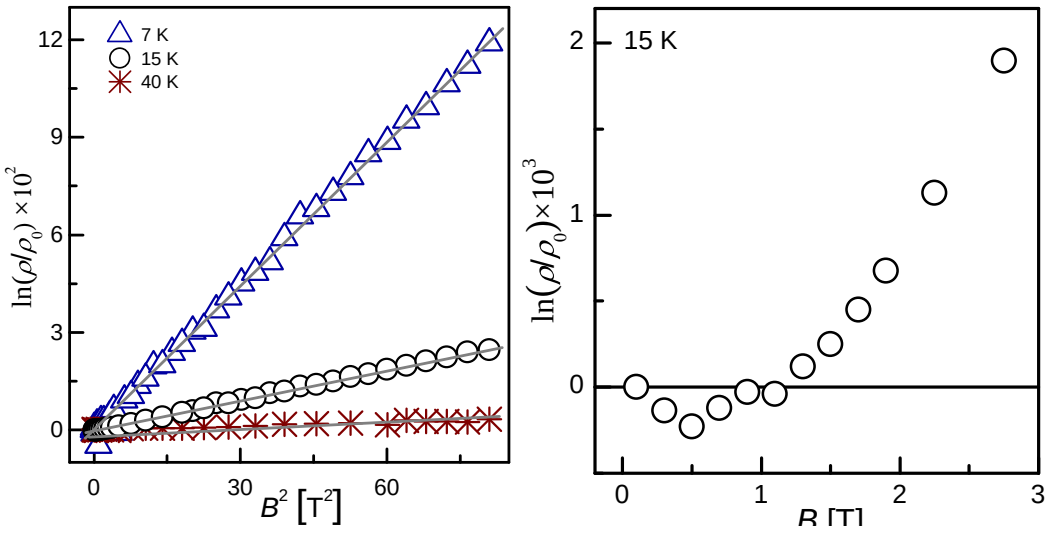

Figure 3.4: Magnetoresistence for PPy-NT-$FeCl_3$ sample. Lines are guides to eyes. Reproduced from Ref. [131].

From the ES VRH at low temperature (with assumed transition to Mott VRH at 7–20 K) we estimated the localization length to 9.7 nm (Eq. 1.26,1.20), which

is higher than, 4.7 nm, reported for the cigar-shaped PPy nanocylinders with ES-Mott VRH transition at about 5 K [147]. Similar values of 11–12 nm, were found for PPy-PF_6 not far from MIT transition [148]. The effective dielectric constant in ES VRH regime from Eq.(4), $\epsilon_r \approx 42$, is much higher than commonly used values [25,142,149] $\epsilon_\mathrm{r} \approx 2$–13.6. Moreover, high values of ϵ_r about 13 were experimental values and probably already contained impurities and charged regions, while low values around 2 reflected the molecular structure of polyconjugated materials. For subsequent T_0^{Mott} used, $g(E_\mathrm{F}) \approx 1.1 \times 10^{19}\,\mathrm{eV}^{-1}\,\mathrm{cm}^{-3}$ and $\epsilon_\mathrm{r} \approx 240$ were atteined. High value of ϵ_r is sign of the singificant contribution of localized states. The existence of the ES VRH regime in our samples can be probably ruled out, supported by the fact that expected temperature dependence of MR could not be perfectly fitted to experimental data and even fit of the heuristic function proposed by Aharony et al. [47] suggested fot the smooth ES-Mott VRH transition did not give satisfactory results. Instead, the use of solely 3D Mott VRH in series with PL was successful at whole temperature range giving $\xi = 4.7\,\mathrm{nm}$ and $g(E_\mathrm{F}) = 6.1 \times 10^{19}\,\mathrm{eV}^{-1}\,\mathrm{cm}^{-3}$ in perfect aggrement with mentioned 4.7 nm in PPy nanocylinders but without need of ES VRH [147]. The value of $g(E_\mathrm{F})$ is however small although such order was observed [150]. Within Kaiser's heterogeneous model with appropriate geometrical factors even the high value of pre-exponential factor can be explained [151]. In order to satisfy reasonable condition $\sigma_{\mathrm{VRH}} < \sigma_{\mathrm{PL}}$, a very small fractional length (*e.g.* 0.1) of VRH regions to high conducting PL regions is required. However, even in this case Mott VRH is not valid in whole temperature range but to *ca.* 240 K due to R_{hop} and W_{hop} imposed criteria. Hence, the transition to NNH at higher temperatures is inevitable. Finally, the reported 2D VRH model ($n = 0.33$) for thin PPy-NT [152] and PEDOT nanowires [146] was not confirmed here but considered only as an intermediate region in complex $W(T)$ without particular meaning. It is supported by the fact that hopping distance at 5 K was found to be 16 nm, satisfactory for 3D hopping to occur in tens of nm thick nanotubes. Nonetheless, the thickness is not always the main parameter but the doping and its homogeneity matter as well. [152] It was also assumed that interplay between geometrical and intrinsic physical properties (*e.g.* the localization length) controls the dimensionality of transport [153].

The second group (samples except PPy-NT-$FeCl_3$) exhibits lower conductivity and mostly the single exponent $n = 0.5$ can be noticed at much higher temperatures, up to about 230 K and the sum with PL affected the parameters only slightly. Exponents 2.5–3.9 for PL are incompatible with the explanation by the critical behavior of 3D systems near MIT ($\gamma < 1$). Similar issue was noticed for single PPy nanotubes and PA fibers and explained by models of charge transport in the Luttinger liquid or the Wigner crystal, but despite these attempts the origin of transport remains unclear [140]. In our case, very low values of pre-exponential factor argue against the use of the PL model. Equally good fit was achieved with parallel connection of the VRH-like model ($n = 0.5$) and the ARH model. The former one can be explained either by Q1D VRH or Zuppiroli's CELT. The Q1D VRH model seem improbable since it gives $g(E_\mathrm{F}) \approx 1.9$–$13\ \mathrm{eV}^{-1}\,\mathrm{nm}^{-1}$, about order of magnitude higher than expected [154], when $\xi = 4.7\,\mathrm{nm}$ and $z = 2$ is assumed. A lower ξ, would result in even higher $g(E_\mathrm{F})$. For the CELT model we assumed Coulomb repulsion $U = 1.56\,\mathrm{eV}$ with monomer unit of 3.7 Å and

$\epsilon_r = 2.5$ [142]. These values then give the ratio s/d within 0.08–0.23. The validity requirements based on the optimal cluster diameter provided an inferior limit for $d \approx 2.3$–3.2 nm and $s \approx 0.2$–0.7 nm. Small polaronic clusters are important at high temperatures and the larger ones at lower ones. However, stability of such small clusters is questionable [60]. Moreover, values lower than monomer width is not convincing as well. On the other hand, only these issues are not enough to rule out the CELT model itself but rather approach based on s/d constraint. Since large clusters with increasing temperature are not limited by the charging energy anymore, we can speculate that they contribute in parallel as the second resistor, ARH. Attempts of other authors to explain Arrhenius-type behavior concern, *e.g.* hopping of bipolarons among degenerate states [155] or hopping between mesoscopic metallic islands [156]. The electric field dependence of conductivity which could help to distinguish at least between the CELT model and the Q1D VRH model could not be obtained due to requirements of very high electric fields ($< 1 \times 10^4\,\mathrm{V\,cm^{-1}}$) at low temperatures. Similarly, data for permittivity for such conductive samples could not be gained. To conclude, existence of two groups of transport mechanisms is not rare, for instance thermal degradation-induced transition from the 3D Mott VRH model to the CELT model was reported for PANI [157].

3.1.2 Polyaniline

The commonly used oxidant for PANI synthesis is APS [12, 135], even though others have been reported, such as $FeCl_3$ [158], $AgNO_3$ [110]. Here we compare electrical properties of PANI prepared either by various oxidants ($FeCl_3$, APS, $AgNO_3$) or in presence of various doping acids (MSA, HCl, Sus, DBSA) (Fig. 3.5). While in case of weak doping acids nanotubular morphology is formed, stronger acids promote granular morphology [21]. We employed the same approach for data evaluation as for PPy samples and results are summarized in Tables 3.3–3.4. Influence of the molar concentration of selected dopant, MSA, is studied as well (Table 3.5, Fig. 3.6).

It should be noted that the LT data (PANI-G-$FeCl_3$(MSA), PANI-G-APS(HCl)) or the low conductivity data (PANI-G-APS(DBSA),PANI-NT-APS(Suc)) in the selected experimental window were very often not reliable and $W(T)$ was affected even more. Since these were still the best data available or the only results that were measured we had to keep them in consideration. Generally, there was no indication for the PL model (region of constant $W(T)$) and the VRH model with exponent 0.4–0.5 was reliable, followed with slope 2.5 above 280 K incompatible with the simple ARH model. The FIT model was also tried but it failed from the same reason mentioned for PPy; there is not any maximum at T_1^F in $W(T)$ plot and since molecular parameters are similar, it is expected that for these saples the FIT model is inappropriate. The exponent 0.4 is plausible within the the FTS model [45] experimentally observed for PANI [159]. Nevertheless, the parallel connection of CELT/Q1D VRH with ARH (the CELT-or-ARH model) could be fitted to data well for PANI-G-APS(HCl) and the MET-and(CELT-or-ARH)

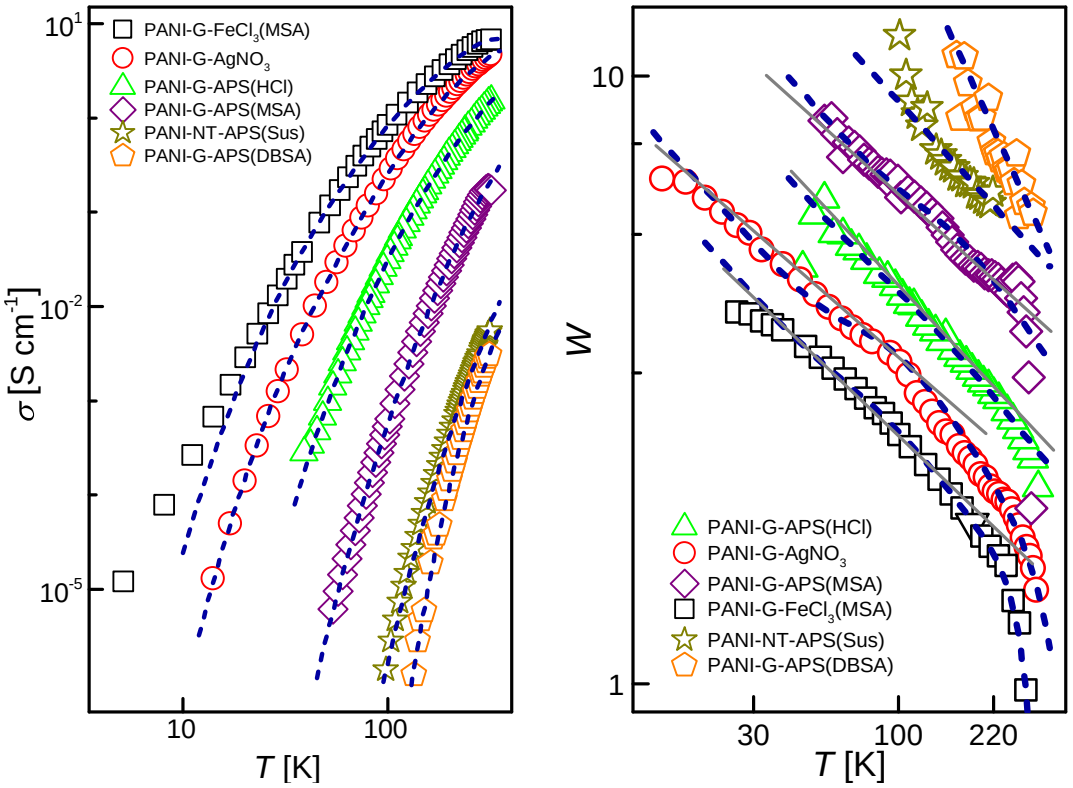

Figure 3.5: Experimental data for $\sigma(T)$ (left) and $W(T)$ (right) and best fits (see text) for granular or nanotubular PANI prepared with various oxidants.

model for samples doped with MSA. The metallic term, Eq. (1.11), was assumed due to mentioned steep decrease of $W(T)$ at higher temperatures. Such contribution was reported for PANI doped with CSA [69, 87]. Therefore, the assumption of two groups with different VRH exponents was redundant. Samples PANI-G-APS(DBSA) and PANI-NT-APS(Suc) exhibited very low conductivity and data were rather of poor confidence so we tried only the single model and any further evaluation was not possible.

Similarly to the analysis of PPy, for the CELT model s/d was found within range 0.16–0.52 when $a = 5\,\text{Å}$ [38] and the same value of $\epsilon_\text{r} = 2.5$ as for PPy were used. The inferior limit for d and s was 1.7–2.1 nm and 0.34–0.89 nm, respectively. The same issue as in the case of PPy arises for low values of s. When the Q1D VRH model was considered, $g^{Q1D}(E_\text{F}) \approx 1.4$–$9.6\ \text{eV}^{-1}\,\text{nm}^{-1}$ for assumed ξ 2.1 nm and $z = 4$ [160]. These values are in agreement with the reported range for variously doped PANI [160]. From the above the Q1D VRH model is slightly preferred in contrary to PPy, although the CELT model could not be ruled out[2].

Since $FeCl_3$ is less common oxidant for PANI we focused more on these samples, and influence of the molar concentration of MSA c_MSA on electrical properties

[2]Since neither the CELT model nor the Q1D VRH model was definitely ruled out, for simplicity we keep using notation CELT-or-ARH, however, one should always think also about its alternative in the Q1D VRH model.

sample	σ_{RT} [S cm^{-1}]	range [K]	σ_0 [S cm^{-1}]	T_0 [K]	n	range [K]	σ_0^F [S cm^{-1}]	T_0^F [K]	T_1^F [K]
PANI-G-APS(HCl)	2.4	4–20	46	92	0.5	40–280	17	870	38
		10–100	600	9300	1				
PANI-G-APS(MSA)	7.3	55–290	6700	1.1×10^6	0.4	55–280	12	1500	49
		200–300	6.7	1100	1				
PANI-G-$AgNO_3$(MSA)	4.1	14–150	780	2.1×10^4	0.4	14–110	7.6	450	20
		4–20	46	92	1				
PANI-G-$FeCl_3$(MSA)	6.5	20–220	500	1.1×10^4	0.5	5–200	20	380	22
		125–300	21	340	1				
PANI-G-APS(DBSA)	3.3×10^{-3}	135–318	1	1800	1				
PANI-NT-APS(Sus)	6.6×10^{-3}	90–318	280	3.6×10^4	0.5	77–260	0.3	1400	11

Table 3.3: Room temperature conductivity and results of fitting according single models represented by Eq.(1.14),(1.12) and (1.39) for PANI of granular and nanotubular morphology synthesized with various oxidants.

sample	σ_0^C [S cm^{-1}]	T_0^C [K]	σ_0^A [S cm^{-1}]	T_0^A [K]	σ_0^{MET} [S cm^{-1}]	T_0^A [K]
PANI-G-APS(HCl)	164	7400	2.2	760	–	–
PANI-G-APS(MSA)	167	1.6×10^4	3.4	1200	–	–
PANI-G-$AgNO_3$(MSA)	65	3400	11	520	0.5	1800
PANI-G-$FeCl_3$(MSA)	85	2300	6.3	410	3.4×10^{-3}	2400

Table 3.4: Results of fitting according to the CELT-or-ARH model or the MET-and-(CELT-or-ARH) model for PANI-G samples synthesized with various oxidants. Related physical quantities are presented as well.

were investigated (Fig. 3.6). In agreement with previous analysis we used the model MET-and-(CELT-or-ARH) to fit the data. It should be noted that only for two concentrations LT data were available (with limited confidence below 40 K probably due to technical problems). The results are summarized in Table 3.5.

c_{MSA} [M]	σ_{RT} [S cm^{-1}]	σ_0^C [S cm^{-1}]	T_0^C [K]	σ_0^A [S cm^{-1}]	T_0^A [K]	σ_0^{MET} [S cm^{-1}]	T_0^{MET} [K]
0	1.3	50	5100	1.7	500	–	–
0.1	1.3	71	5500	1.5	450	3.5	580
0.2	2.1	89	4800	2.9	460	0.17	1800
0.5	6.5	85	2300	6.3	410	3.4×10^{-3}	2400
1.0	2.7	32	3900	5.1	480	2.2×10^{-4}	3900

Table 3.5: Results of fitting according to the MET-and-(CELT-or-ARH) model for PANI-G-$FeCl_3$(MSA) synthesized with various c_{MSA} (0–1 M) according to MET-and-(CELT-or-ARH) model.

Obviously, the dependence of conductivity on molar concentration is not monotonic (Fig. 3.7). Pre-exponential factors for the semiconducting models, ARH and

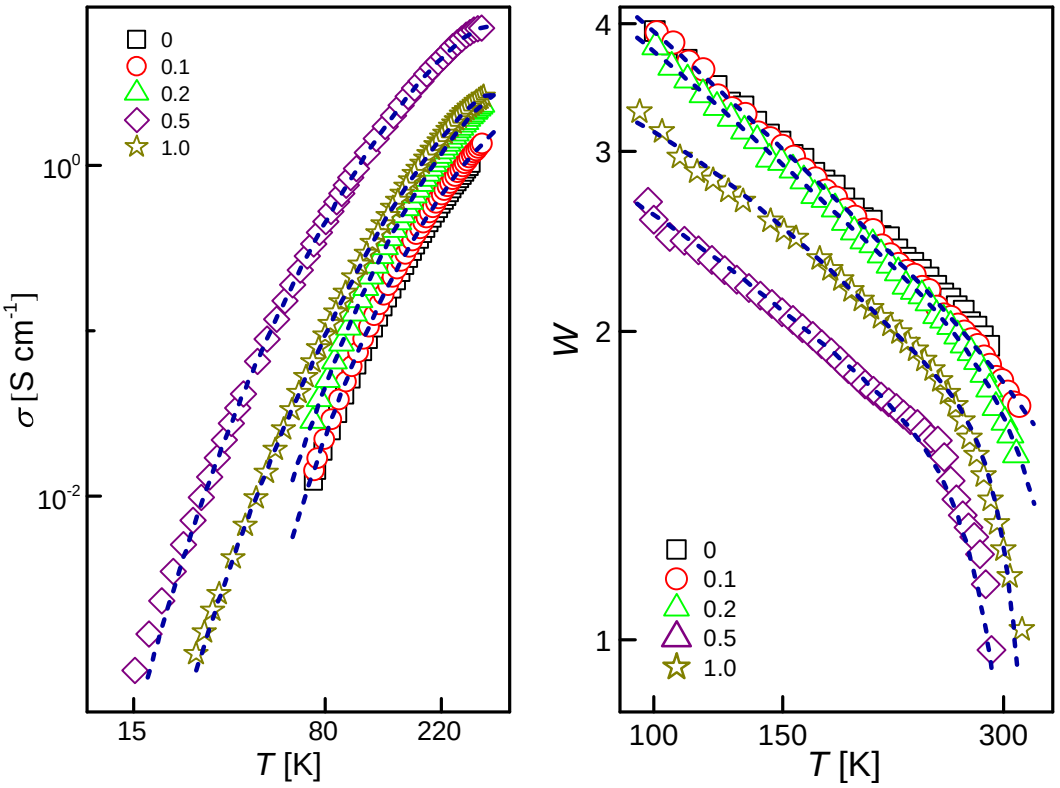

Figure 3.6: Experimental data for $\sigma(T)$ (left) and $W(T)$ (right) and fits according to the MET-and-(CELT-or-ARH) for PANI-G-$FeCl_3$(MSA) and various molar concentration of MSA.

CELT/Q1D VRH, mimic room temperature conductivity, while prefactor for the metallic part logarithmically decreases with concentration. Disorder parameter T_0 is constant for the ARH model and decreases for the CELT/Q1D VRH model in agreement with enhanced conductivity. In the case of the MET model it increases with concentration, again as the sign of better order. Indeed this system could be technologically interesting provided that the metallic regions are enhanced at expense of disordered structure. This could be a direction for future investigation.

Thin PANI films were all prepared with APS oxidant in standard HCl aqeous solution, then converted to base form in 1 M NH_4OH solution and again reprotonated in aqueous solutions of various sulfonic acids (MSA, FCA, DBSA, PSSA, PAMPSA). The aim of such reprotonation with large organic molecules was to ensure better stability [93] and as such for sensor testing (Sec. 4.4). Experimental data, $\sigma(T)$ are plotted at Fig. 3.8. Unfortunately, only the HT data were obtained, which were usually scattered and less trustworthy. Following the previous approach, the single ARH model, the CELT model and their combination in parallel were tried to fit the data but result (Table 3.6) were of limited reliability. However, contrary to pellets, the inconsitency of small clusters and spacing is lifted due 1–2 orders of magnitude higher T_0^{C}.

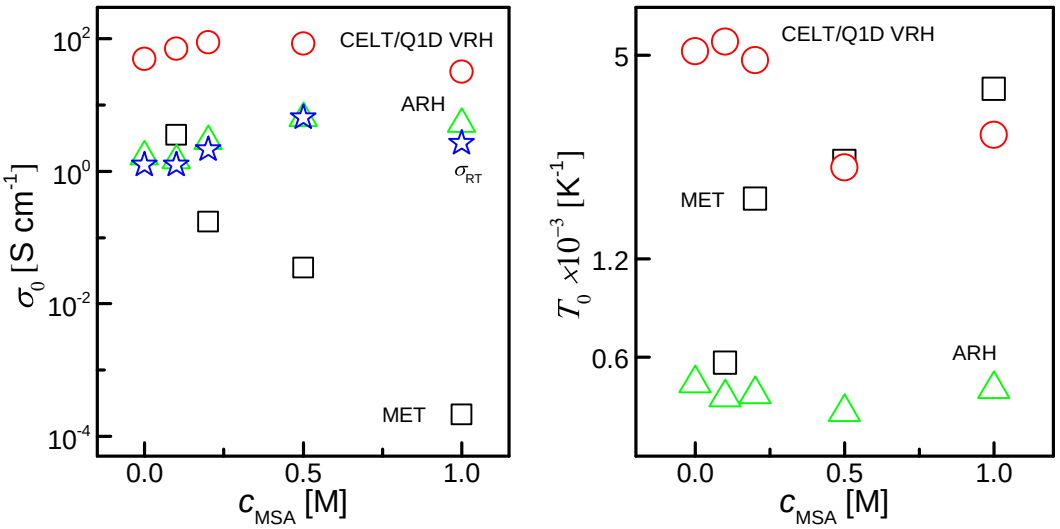

Figure 3.7: Dependence of σ_{RT} and fit parameteres, σ_0 (left) and T_O (right), on molar concentration of MSA.

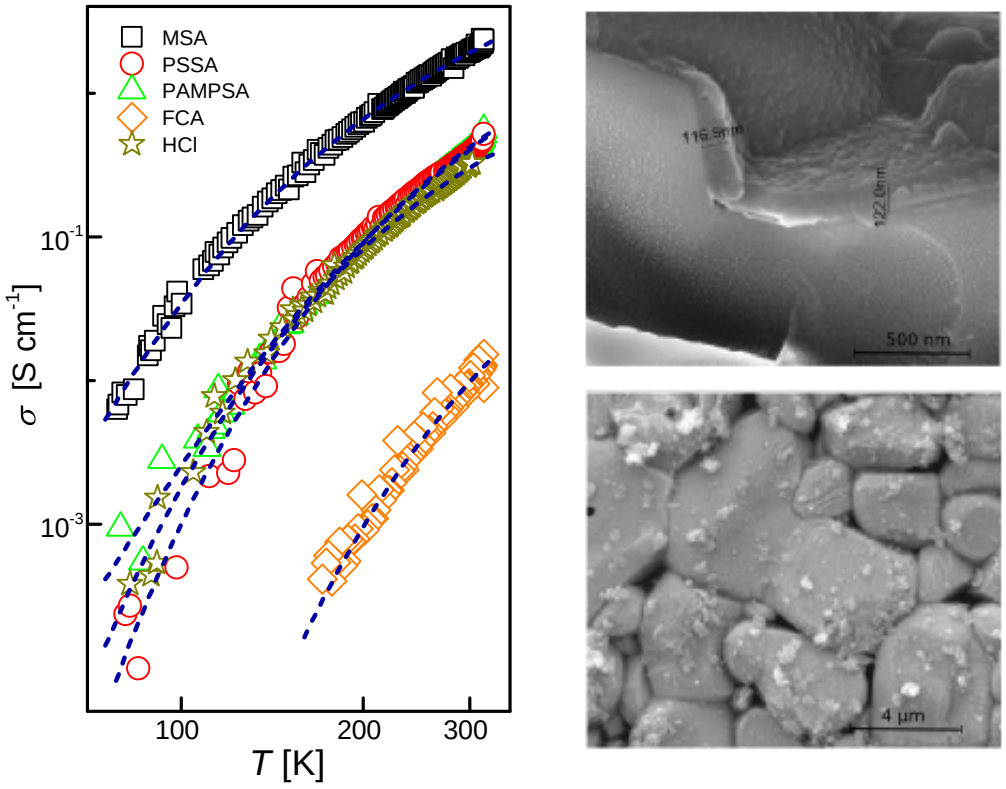

Figure 3.8: Temperature dependence of conductivity for thin PANI films reprotonated by various sulfonic acids (left) and SEM image of film roughness (right).

3.1.3 Summary I

We found that from conductivity point of view iron(III) chloride was the best oxidant for both, PPy and PANI. In this case, nanotubular morphology of PPy even increased conductivity providing well doped and ordered regions close to

acid	model	range [K]	σ_0 [S cm^{-1}]	T_0 [K]	n
HCl	ARH	80–310	14	770	1
	CELT	120–310	1.2	1.3×10^4	0.5
	CELT-or-ARH	110–310	3.7	770	1
		110–310	15	1.4×10^4	0.5
MSA	ARH	170–318	17	690	1
	CELT	110–318	1.2	8400	0.5
	CELT-or-ARH	80–318	10	600	1
		80–318	144	9.5×10^3	0.5
PSSA	ARH	150–310	7.6	820	1
	CELT	80–310	6.6	1.2×10^4	0.5
	CELT-or-ARH	80–310	8.1	910	1
		150–318	95	2.0×10^4	0.5
PAMPSA	ARH	150–310	9.5	990	1
	CELT	110–310	60	1.9×10^4	0.5
	CELT-or-ARH	80–318	3.7	980	1
		80–318	140	1.2×10^4	0.5
FCA	ARH	170–300	1.0	1400	1

Table 3.6: Results of fitting for PANI thin films reprotonated with various sulfonic acids according to the CELT model and the ARH model, and their combination (CELT-or-ARH).

MIT or with 3D VRH. The model based on their serial connection was found to explain the experimental data, both $\sigma(T)$ and corresponding $W(T)$. On the other hand, self-assembled PANI-NT prepared in presence of weak acids and APS as oxidant were only poorly conducting. When silver nitrate was used instead of common oxidants for PPy and PANI, conductivity decreased. However, metallic silver was reduced and silver-decorated conducting polymers were formed. A whole Sec.3.3 is dedicated to these systems. Charge transport in the less conducting samples with $\sigma_{RT} < 10\,\mathrm{S\,cm^{-1}}$ was explained by combination of tho parallel resistors representing the CELT model or the Q1D VRH model and the ARH model. Their origin was assumed to come from (bi)polaronic clusters of various sizes when the GM model was preffered over the Q1D VRH model in case of PPy according to the analysis of parameters. In case of PANI, the situation was opposite. Nevertheless, for discrimination between models, study of the dependence of conductivity on the electric field should follow.

Methanesulfonic acid appeared to be a good candidate for doping but non-monotonous concentration dependence of conductivity was found. Apart of disordered regions represented by the GM models a metallic term was introduced to fit mainly high temperature region with steep decrease of $W(T)$.

Finally, PANI films despite of their importance in applications (contrary to

pellets), their measurements and evaluation turned out to be more difficult due to non-uniform thickness and mostly scattered conductivity data in the limited temperature range. Inspired by their bulk counterparts we employed the same theoretical model to explain charge transport. Again, MSA turned out to be the best dopant since these PANI films exhibited the highest conductivity.

3.2 Effect of polymerization temperature and template

This section is dedicated to other variations in chemical synthesis than are discussed in Sec. 3.1 but which can be also important from the conductivity point of view, an effect of polymerization temperature (T_p), the molar concentration of methyl orange (c_{MO}) and various azo dyes (methyl orange, acid red, orange G, sunset yellow) as templates are investigated. The charge trasport evaluation is built up on the results from previous section for both PPy and PANI. Hence, in the following we skip the evaluation of the FIT model and subsequent single models in limited temperature range.

3.2.1 Polymerization temperature

The effect of polymerization temperature on conductivity in this thesis is studied on the 'standard' PANI-G-APS(HCl) samples although its effect was found also for PPy-NT-$FeCl_3$ polymerized at room temperature [161] which exhibited lower conductivity than our 'standard' samples synthesizes at 5 °C. For PANI samples T_p within range −20–40 °C were investigated. It should be noted that T_p has the meaning of initial temperature since during chemical reaction temperature changes (exothermic reaction) [137]. The influence of T_p on σ_{RT} was found negligible in contrary to other properties such as molecular weight [162]. However, the detailed study of the charge transport mechanism was not presented. Alongside to the spectroscopic study it was the main goal of the recent study [137]. These data are plotted at Fig. 3.9, for clarity reasons only at LT region where the difference in $\sigma(T)$ is more pronounced. Moreover, the $W(T)$ data were of rather poor quality. For the analysis of transport we employed the CELT-or-ARH in agreement with previous section. This analysis extends the preliminary reported results. A departure from the model was found for the lowest T_p where exponent 0.4 had to be used instead. Since this is in principle allowed by the FTS hopping model [45], the VRH model seems again more appropriate then CELT. This sample exhibited unusually high position of the quinoid band maximum attributed to possible higher regularity of chains [137]. Although differences in conductivity at room temperature were negligible, as large as two orders of magnitude at LT region were observed. The effect of thermostat (sample 20 vs. 20-N) during polymerization on final conductivity was found negligible. In general, the higher reaction temperature the steeper decrease of conductivity with tempera-

ture. It resulted in decrease of σ_0 and T_0 with lowering T_p except $-20\,°C$ where the exponent was changed. This observation could be correlated with decrease of structural defects (albeit unspecified), increase of crystallinity, toughness and compactness of of PANI microparticles [137]. These factors could be important in the suggested model.

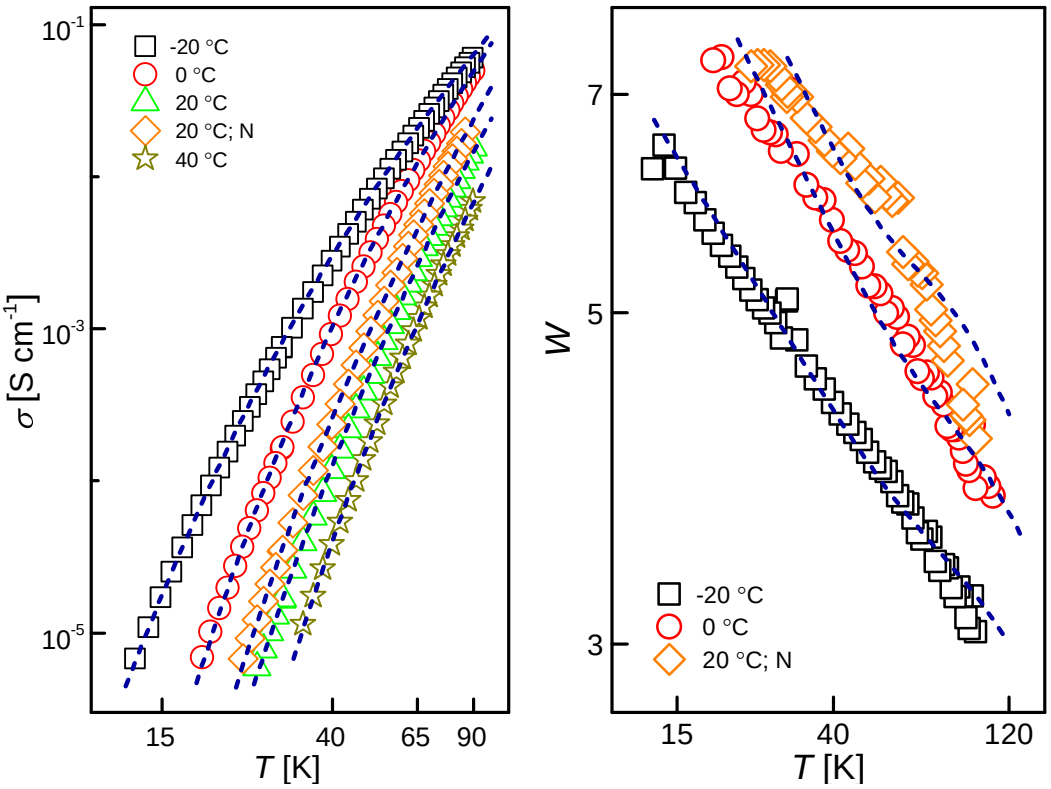

Figure 3.9: Experimental data for $\sigma(T)$ (left, adopted from Ref. [137]) and $W(T)$ (right) and fits according to the CELT-or-ARH model for PANI prepared at various T_p.

T_p °C	σ_{RT} [S cm^{-1}]	σ_0 [S cm^{-1}]	T_0 [K]	n	σ_0^A [S cm^{-1}]	T_0^A [K]
40	0.9	170	8900	0.5	1.6	630
20	2.1	150	6900	0.5	5.4	550
20-N	1.7	140	6600	0.5	9.7	640
0	1.8	83	5100	0.5	6.3	640
-20	1.5	140	15100	0.4	2.0	550

Table 3.7: Room temperature conductivity and results of fitting of $\sigma(T)$ for PANI-G-APS(HCl) synthesized at various T_p according to the model CELT-or-ARH.

3.2.2 Influence of template

Besides various dopants/oxidants the influence of morphology is important as well. We showed that T_p had only slight influence on morphology and conductivity. In the following the attention is turned to template-synthesized PPy and the effect of template. Various azo dyes were used as structure-guiding agents; methyl orange, acid red , orange G and sunset yellow . Their chemical structure can be found elsewhere [132]. The final structure differs in induced morphology and the content of granular phase. Nanotubes were found only for MO, while other azo dyes rather form nano(micro)plates. Granular phase increases in the direction MO→OG→SY→AR. The influence of template on morphology still deserves more research.

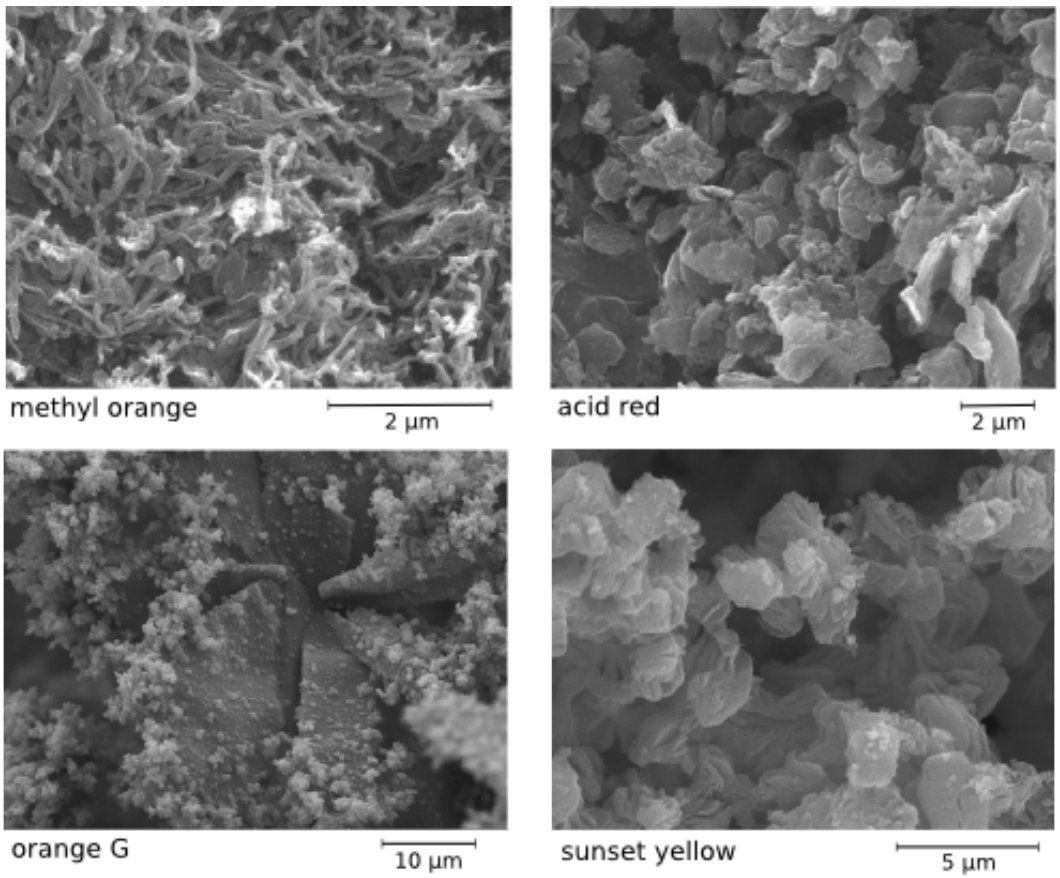

Figure 3.10: Morphology (SEM) of PPy prepared with various azo dyes.

The previous finding that granular morphology yields results in lower conductivity (Sec.3.1) was confirmed, σ_{RT} varied 2.2 S cm^{-1}–54 S cm^{-1} (Table 3.8). We should keep in mind that these values could differ from sample to sample due to different age. However, even within 20 % confidence interval three groups can be noted. The use of the Mott-3D-VRH-and-PL model was previously successfully employed for explanation of charge transport in PPy-NT. This model, however, gave exponent in PL slightly out of range (> 1). Since conductivity is close to that for granular PPy these samples are probably close to transition to the GM regime.

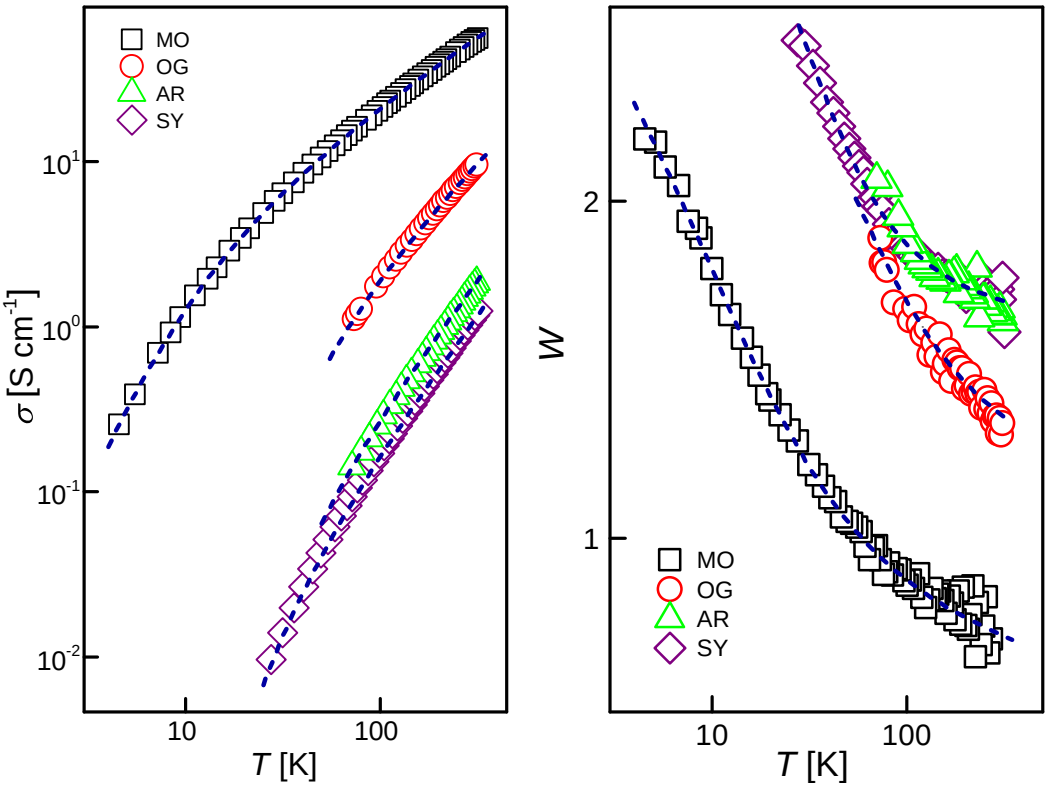

Figure 3.11: Experimental data for $\sigma(T)$ (left) and $W(T)$ (right) and fits according to the Mott-3D-VRH-and-PL model for PPy prepared with various templates.

template	σ_{RT} [S cm^{-1}]	σ_0 [S cm^{-1}]	T_0 [K]	a [S cm^{-1} K$^{-\gamma}$]	γ
MO	54	6300	4.6×10^4	1.3	0.80
SY	3.2	9300	8.9×10^5	1.7×10^{-4}	1.6
AR	2.2	8010	7.9×10^5	4.6×10^{-4}	1.5
OG	10	17200	5.1×10^5	1.9×10^{-2}	1.1

Table 3.8: Room temperature conductivity and results of fitting of $\sigma(T)$ and $W(T)$ for PPy-$FeCl_3$ synthesized with various templates (azo dyes) according the Mott-3D-VRH-and-PL model.

The conductivity can be modified also by the concentration of template [130]. We focused on MO as the most promising azo dye. The molar concentration c_{MO} was varied from 0.44 to 20 mM. The subsequent dependence of conductivity is not monotonous and exhibits maximum at 0.5 (Fig. 3.13). The experimental data for $\sigma(T)$ (Fig. 3.12) were evaluated using the Mott-3D-VRH-and-PL model (Table 3.9) which was found consistent for well conducting samples (σ_{RT} >20 S cm^{-1}). Surprisingly, the extremal value of fit parameters is shifted to higher concentration comparing to σ_{RT}. On the other hand, only HT data were available for some samples which could be the reason for inaccurately estimated parameters. Also low values of the PL exponent are rather suspicious. For the rest of samples the fit

to the model was rather artificial and the transition to the GM regime probably occurred. This could be related to higher content of granular phase which was found in these samples (Fig. 3.14). Please note that obtained fit parameters for all samples are probably higher than expected for fresh samples due to various age of samples at the time of measurement, the same is true of σ_{RT} which is slightly lower then previously reported [130]. In summary, there are indications for non-monotonous dependence of transport parameters on template concentration but more research is still needed to obtain full picture, mainly possible crossover to other regime.

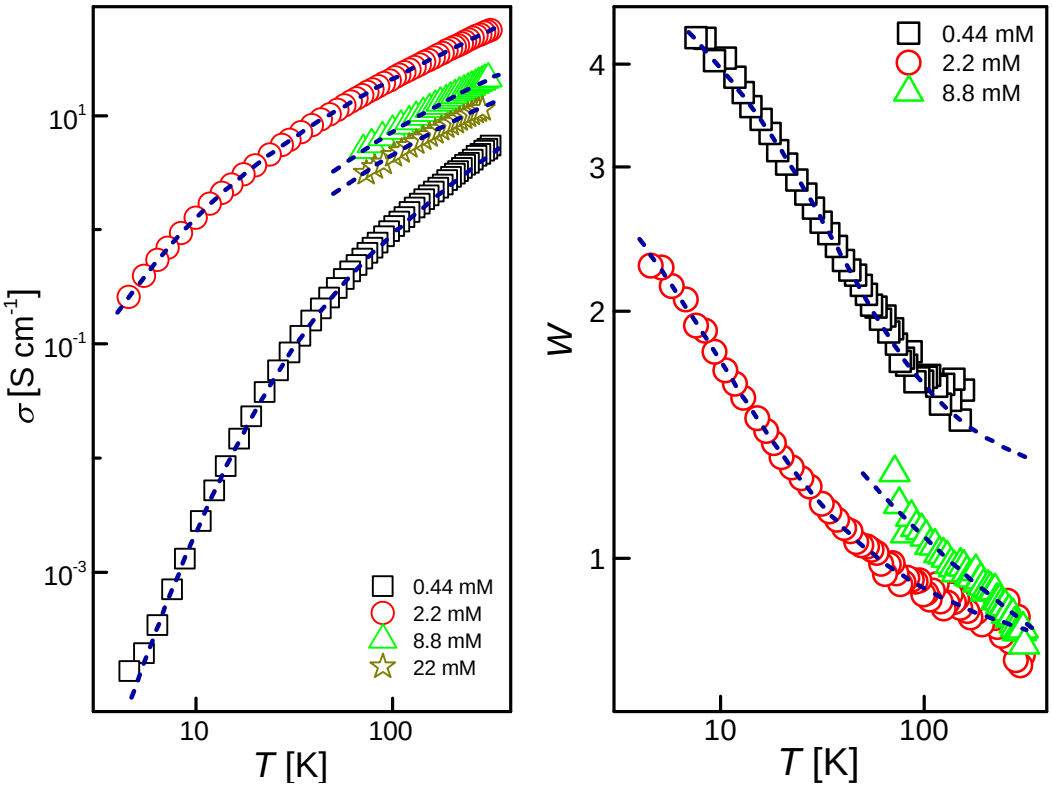

Figure 3.12: Experimental data for $\sigma(T)$ (left) and $W(T)$ (right) and fits according to the Mott-3D-VRH-and-PL model for PPy-NT-$FeCl_3$ prepared with various c_{MO}.

c_{MO} [mM]	σ_{RT} [S cm^{-1}]	σ_0 [S cm^{-1}]	T_0 [K]	a [S cm^{-1} K$^{-\gamma}$]	γ
0.44	5	2.2×10^4	6.7×10^5	5.6×10^{-3}	1.2
2.2	54	6.4×10^3	4.6×10^4	0.79	0.80
4.4	46	1.4×10^3	2.9×10^4	2.7	0.79
8.8	20	1.0×10^3	4.7×10^4	0.99	0.74
22	12	1.4×10^3	8.0×10^4	0.72	0.60

Table 3.9: Room temperature conductivity and results of fitting according to the Mott-3D-VRH-and-PL model for PPy-NT-$FeCl_3$ synthesized with various c_{MO}.

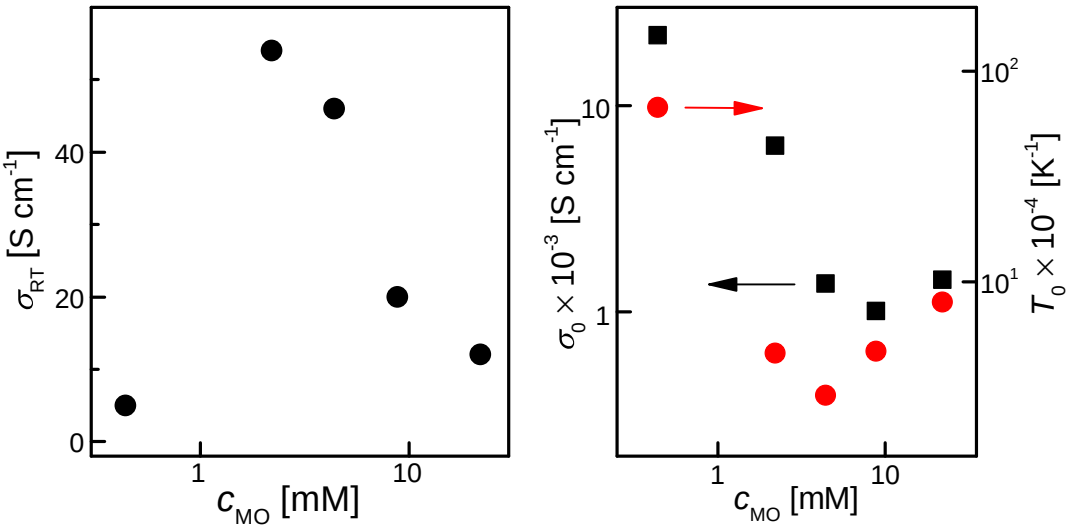

Figure 3.13: Dependence of σ_{RT} (left) and fit parameters of the Mott-3D-VRH-and-PL model (right) for PPy-NT-$FeCl_3$ prepared with various c_{MO}.

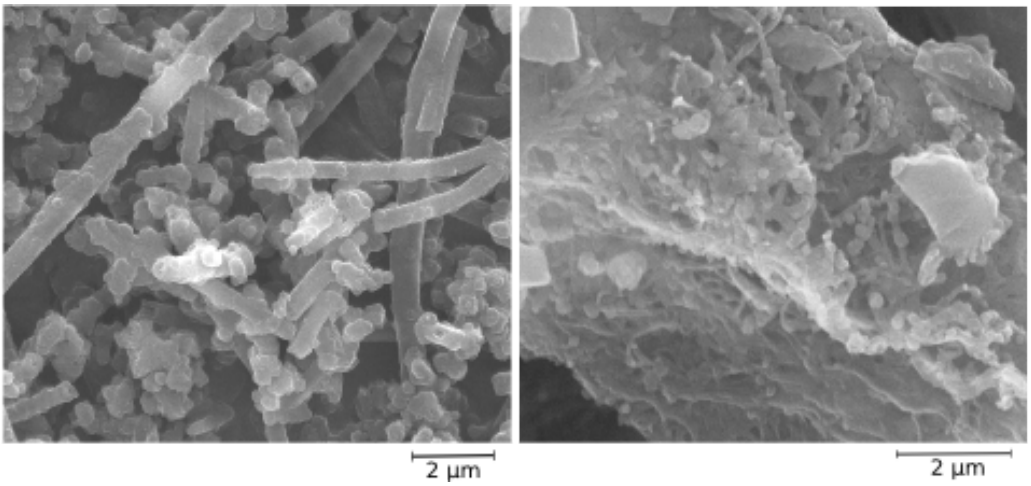

Figure 3.14: Morphology (SEM) of PPy prepared with concentration 0.44 mM (left) and 22 mM (right) of MO.

3.2.3 Summary II

In this section the influence of polymerization temperature and template on conductivity and charge transport was investigated. Only small effect of T_p in case of PANI-G samples with the trend of slight enhancement of transport with decreasing temperature was found. In contrary, in the case of template-synthesized samples (PPy) decrease of conductivity and possible transition from the VRH regime to the GM regime was observed. This is believed to be due to increasing content of granular phase caused either by different azo dyes than MO or low/high concentration of MO. Further investigation of such transition can be useful for better understanding of structure-property relationship in these materials. Consequently, it could be useful for their tailoring and functional material design.

3.3 Effect of silver decoration

This section is dedicated to study of silver-decorated polymer composites. Such composites were produced in-situ by chemical reduction of silver cations from the oxidant $AgNO_3$ during polymerization. Interestingly, from originally two non-conducting components (aniline/pyrrole, silver nitrate) the conducting product is obtained with tunable silver content and conductivity. It has been showed that aniline is able to reduce silver ions [110] and that the silver content can be controlled by mixing with APS oxidant [138]. Silver can be also reduced on previously prepared (double-step synthesis) PANI [110] and PPy [133]. Silver with the highest electrical conductivity among metals, reasonable price, antibacterial properties, *etc.*, was considered as a good choice for such composites. Achievements and visions for PANI-silver composites have recently been reviewed [110].

In the following we present the charge transport study for PANI-silver and PPy-silver composites depending on the silver volume content[3] and morphology as comparable parameters (Fig. 3.3) since the conditions for their synthesis differ. As mentioned, PANI-Ag samples with variable silver content were achieved with mixed oxidants APS and $AgNO_3$ with various ratio [138] while the same for PPy-Ag was provided by various molar concentration of MO with constant ratio of pyrrole and $AgNO_3$ being either equimolar or stoichiometric. The second approach however suffers from the changes of morphology and intrinsic properties of polymers matrix with variable c_{MO} as we reported in Sec. 3.2. The higher was template concentration the lower silver content was achieved. In the case of PPy-Ag-s the granular form with large silver clusters prevailed contrary to mostly nanotubular form with smaller silver decoration in PPy-Ag-e samples [134]. Hence, changing the monomer to oxidant ratio different systems were obtained.

In general samples can be divided into the two groups exhibiting semiconducting and metallic behavior, respectively. The latter begins when σ_{RT} is of order $10^2\,S\,cm^{-1}$. Some preliminary results for PANI-silver composites, $\sigma(T)$ analysis based on the HT data and influence of aging have been already reported [163,164]. Here we add the LT data and the transport analysis is revisited with help of $W(T)$; the results are merged with PPy-silver composites and discussed from a wider perspective. Some general features can be noted for all conducting samples (polymer salts) regardless of details (polymer matrix, morphology): I) decrease of conductivity with increasing silver content, II) subsequent increase of conductivity after some 'critical' volume concentration is achieved. The absence of first region for the polymer base form has some consequences. Particularly, conductivity in the first region conductivity is 2-3 orders of magnitude higher than for typical PANI base [12] probably due to tunneling of electrons between silver metallic islands (the GM model) and conductivity for salts-silver composites is determined by the intrinsic conductivity of polymer salt which is disrupted by non-conducting silver decoration, most probably due to decrease of the overall

[3]Determined from silver weight as the ash residuum. Colleagues who made measurements at IMC AS CR are fully acknowledged

conducting phase. Abrupt conductivity increase of the percolation-like behavior for base form is modified to only 2-3 order of magnitude increase due to conductivity in polymer salts. In both case a connected pathways of metallic silver is assumed since conductivity is much higher than that of common semiconducting CP. A direct comparison with standard percolation systems hardly can be made due to very wide (unknown) dispersion of metallic silver ranging from tens of nm to several µm (Fig. 3.15). Moreover, matrix presented by CP itself contains regions that are conducting and separated by amorphous insulating phase. Nevertheless, in order to have some insight we fitted the data with two power law functions; the first region using a phenomenological expression in form of Eq. (1.47) with negative exponent s, and the second region with expression for percolating systems above threshold Eq. (1.46). Results are summarized in Table 3.10. For PANI-Ag base form the exponent is negative which is nothing else than percolation equation below threshold, Eq. (1.47). Finally, the last typical feature of composites besides wide distribution of silver particles sizes is the very limited reproducibility (in terms of various batches). Both are probably the price for the simplicity of their synthesis. In the following we focus more on the charge transport mechanism.

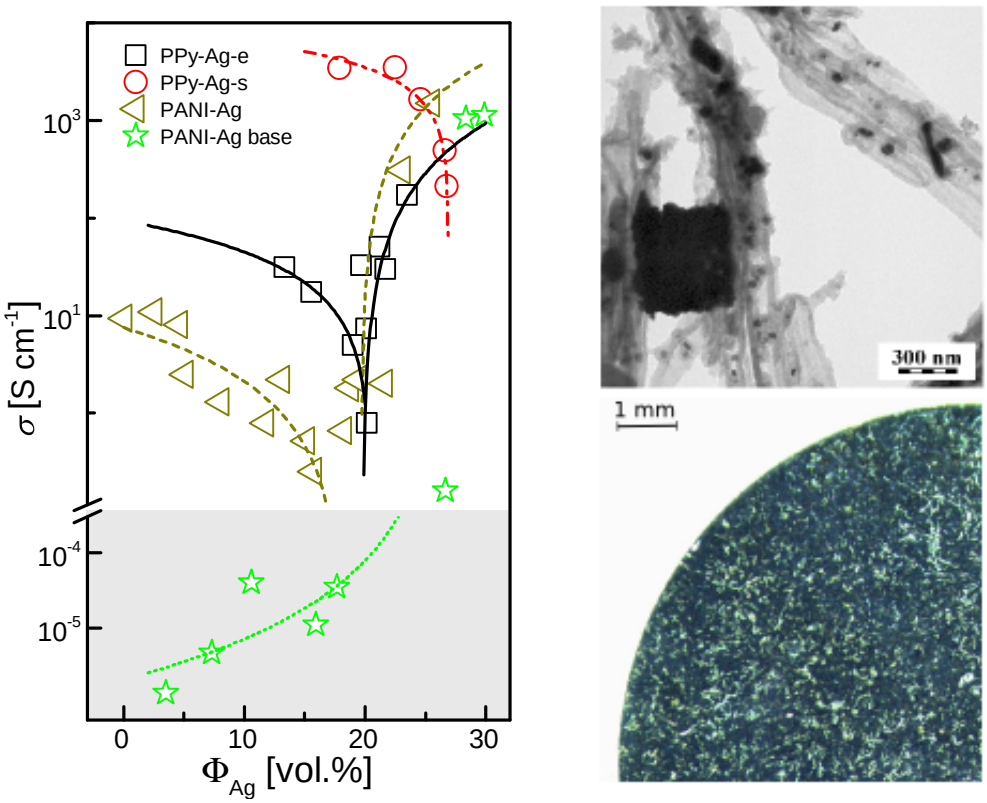

Figure 3.15: Dependence of conductivity on silver volume fraction (left) for various silver decorated systems based on PANI-G [163,164] and PPy-NT with corresponding fits. Typical structure of polymer-silver composites on microscale and macroscale (right).

sample	σ_0 [S cm^{-1}]	Φ_C [vol.%]	s	σ_0 [S cm^{-1}]	Φ_C [vol.%]	t
PANI-Ag	110	18.1	-1.58	1.5×10^5	19.7	1.6
PANI-Ag base	6.0×10^{-8}	27.0	2.7			
PPy-Ag-e	540	20.4	-1.10	5.1×10^4	19.8	1.75
PPy-Ag-s	2.2×10^4	26.9	-0.69			

Table 3.10: Results of fits for σ_{RT} with power law functions Eq. (1.46) and Eq. (1.47) for various polymer-silver systems.

3.3.1 Semiconducting regime

According to the model selected in Sec. 3.1 we analyzed PPy-Ag-e composites using the CELT-or-ARH model. The same was initially chosen for PANI-silver samples [163, 164] but the steep decrease of $W(T)$ at high temperatures indicated some other mechanism. The metallic term was assumed due to presence of MSA dopant in analogy with results for PANI-$FeCl_3$(MSA) samples resulting in use of the MET-and-(CELT-or-ARH) model. Fit results are summarized in Table 3.11. For brevity only selected samples are presented at Fig. 3.16.

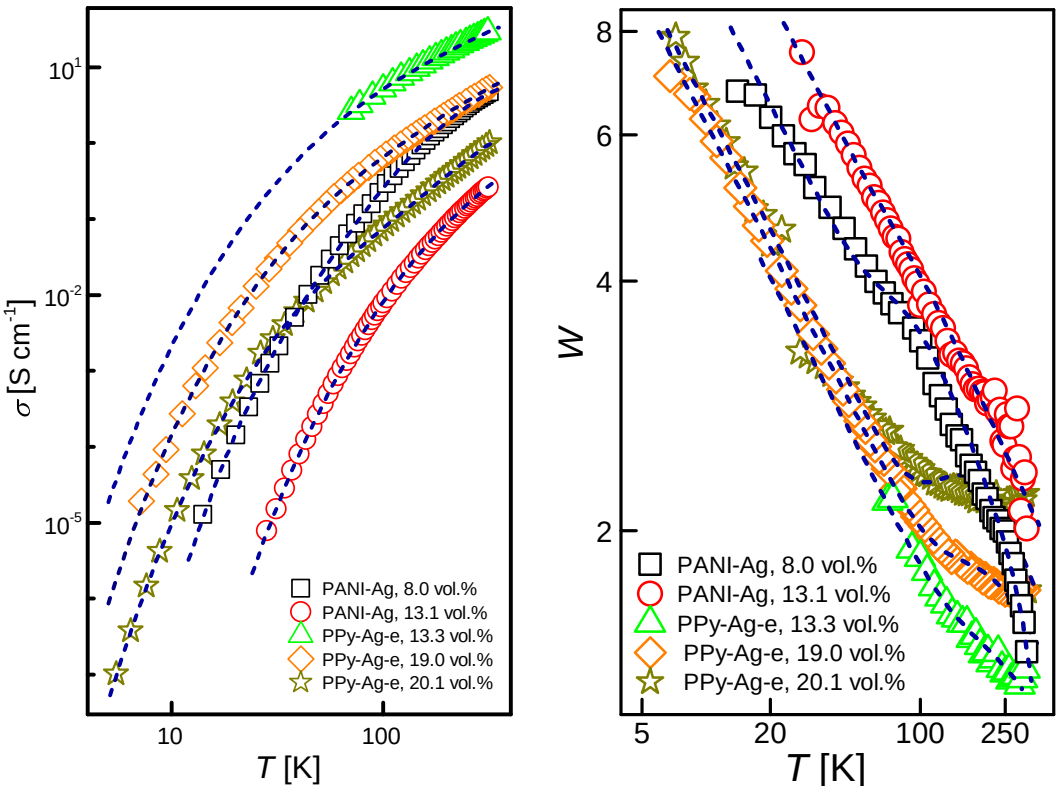

Figure 3.16: Experimental results $\sigma(T)$ (left) and $W(T)$ (right) for semiconducting PANI-silver and PPy-silver composites with corresponding fits.

For PPy-Ag-e samples pre-exponential factors follow the dependence of σ_{RT}

sample	Φ_{Ag} [vol.%]	σ_{RT} [S cm^{-1}]	σ_0^C [S cm^{-1}]	T_0^C [K]	σ_0^M [S cm^{-1}]	T_0^M [K]	σ_0^A [S cm^{-1}]	T_0^A [K]
PANI-Ag	0	9.4	170	3700	0.4	1800	2.5	240
PANI-Ag	4.6	8.1	100	2200	0.5	2000	2.5	280
PANI-Ag	8.0	1.3	65	3400	0.5	1800	11	520
PANI-Ag	13.1	2.2	20	6200	0.2	620	15	1700
PANI-Ag	15.2	0.52	54	7000	0.7	120	58	1800
PANI-Ag	15.7	0.25	42	6700	1.5	50	83	1900
PANI-Ag	21.6	2	12	5600	0.7	700	2.5	1100
PPy-Ag-e	13.3	31	190	1300	–	–	63	840
PPy-Ag-e	19.0	5.0	33	1500	–	–	20	800
PPy-Ag-e	20.1	0.79	4.5	1700	–	–	5.4	760
PPy-Ag-e	21.2	51	400	1500	–	–	220	1300

Table 3.11: Room temperature conductivity (for PANI-ag taken from Refs. [163, 164]) and results of fit according to the model MET-and-(CELT-or-ARH) for PANI-Ag and the CELT-or-ARH model for PPy-Ag-e samples with various Φ_{Ag}.

on silver volume, T_0^A remains almost constant below Φ_C and then increases, and finally T_0^C increases below Φ_C and then decreases reflecting the level of disorder in samples (Fig. 3.17). In PANI-Ag the confidence in fitted parameters is reduced due to extended set of parameters coming from the metallic term. Nevertheless, with the increasing silver content the prefactor σ_0^C decreases, σ_0^A increases in contrary to PPy-Ag-e and finally, σ_0^M slightly increases. Increase of T_0^C and T_0^A reflects increasing disorder up to Φ_C. The same trend is reflected in T_0^M which correspondingly decreases. Obviously the transport parameters are influenced by the volume content of silver, however, they are all related to transport in CP itself. It is questionable how disorder in CP which is determined on lengthscale of maximally tens of nm according to models can be affected by coarse grain character of silver clusters and aggregates. One can think of presence of much smaller silver decoration (tens of nm) but its actual part in the overall silver volume is unknown. It should be kept in mind that except silver content there are other parameters that vary, *e.g.* ratio of oxidants or MO content and morphology. But an alternative explanation based solely on transport in CP affected these parameters is questionable as well since the changes here are more pronounced than we observed for instance in PPy-NT-$FeCl_3$ samples with varying c_{MO}. Maybe both approaches could be used but to this point the transport in semiconducting CP decorated by silver remains puzzling.

3.3.2 Metallic regime

Samples with $\sigma_{RT} > 10^2$ S cm^{-1}, here only PPy-Ag-s were subject of study, exhibits metallic or mixed behavior. The former one is well described by metallic term, Eq. (1.9), which is common approximation for noble metals above ca. 100 K

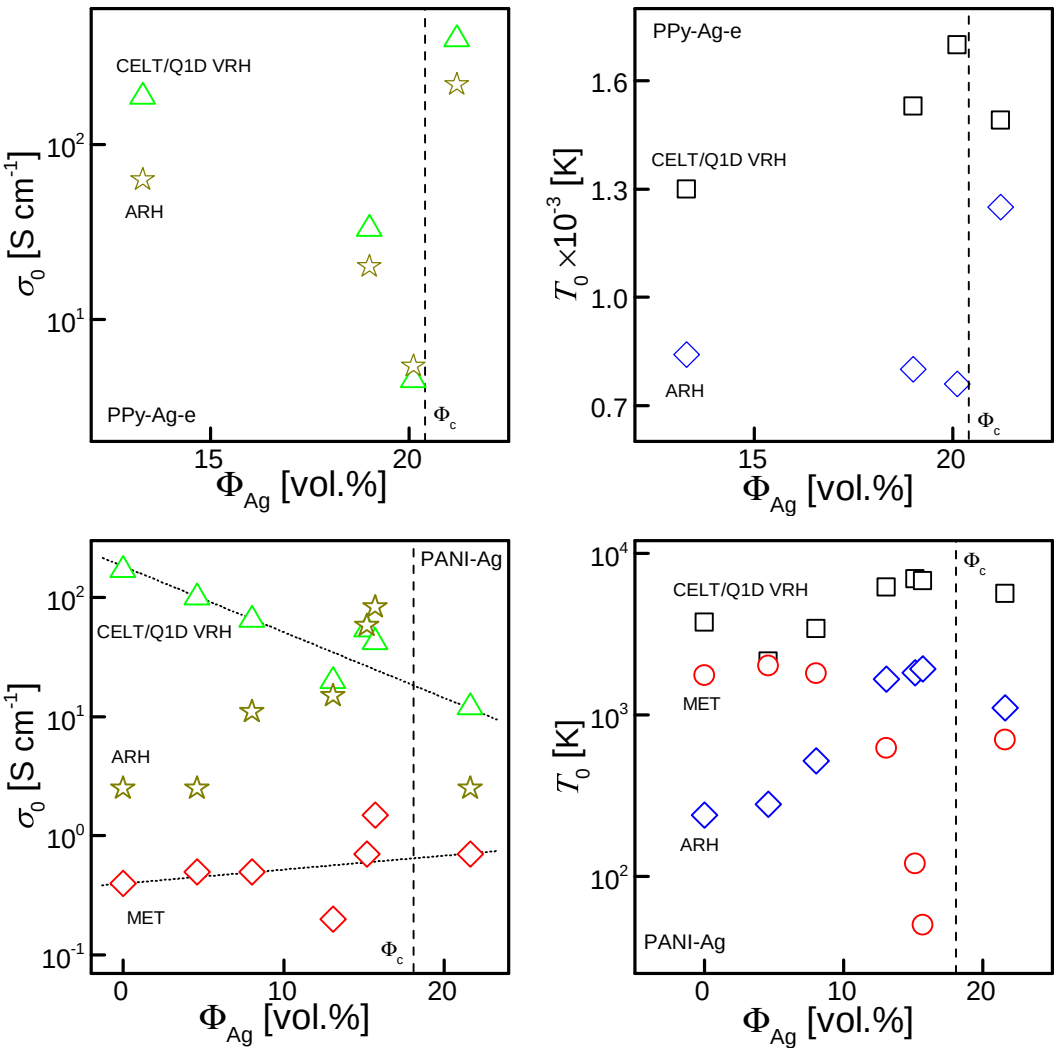

Figure 3.17: Fit parameters σ_0 (left) and T_0 (right) corresponding to the CELT-or-ARH model or the MET-and(CELT-or-ARH) model for PANI-Ag and PPy-Ag-e.

[165]. The latter, mixed conductivity, requires the semiconducting term, which was assumed in the PL form, Eq. (1.12). The power law is typical in critical region of MIT [27, 166]. The results of the METAL-or-PL model fit are summarized in Table 3.12. We assume that the metallic term is due to presence of large connected silver macro/microaggregates and conductivity decreases with temperature due to scattering of electrons on phonons, or eventually on metal-matrix interfaces [58]. We believe that value of conductivity, still two orders of magnitude lower than is typical for bulk silver, and the temperature coefficient of resistivity are linked with connectedness of silver aggregates and a large number of scattering spots at interfaces. Obtained exponent 0.72 would mean that system is rather closer to insulating region provided that the PL scenario is valid. We believe large disconnected silver clusters are the cause of this contribution alongside with fully-connected silver aggregates. We do not claim that there is not any contribution from PPy but for so highly conductive samples it would be substantially lower and thus hidden behind silver contribution. From this point of view charge transport in polymer-silver composites was considered to be fully driven by silver and the

term 'silver decoration' is maybe not adequate anymore.

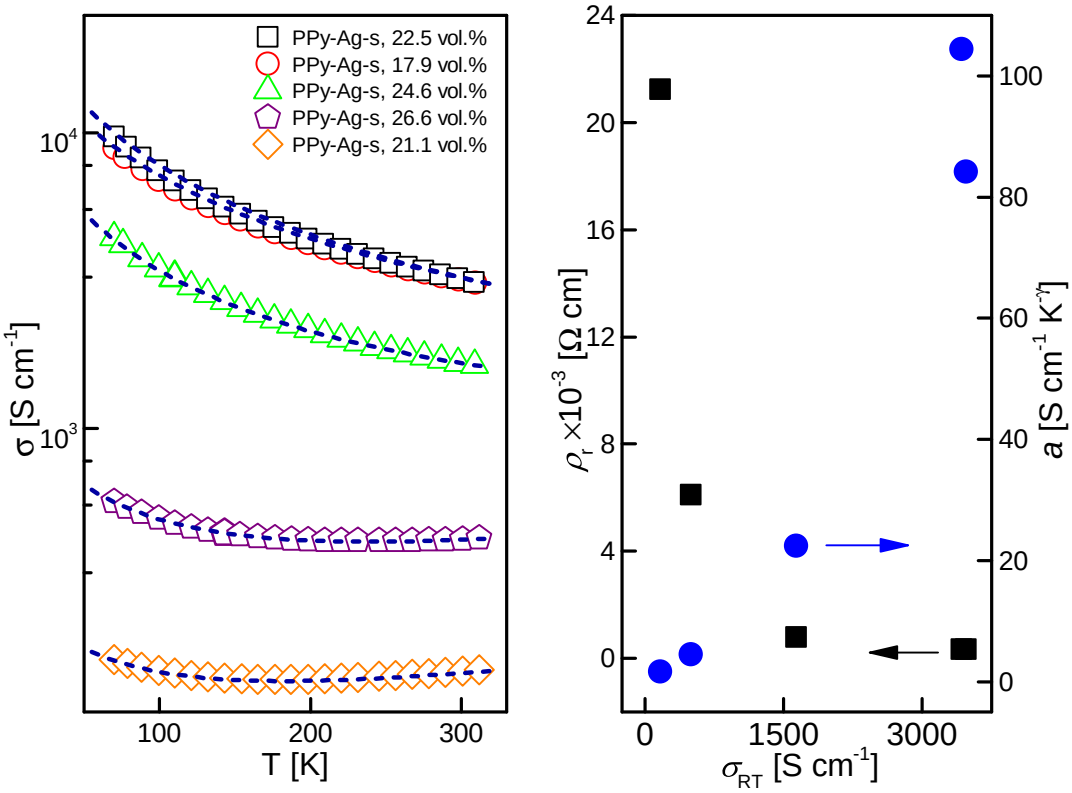

Figure 3.18: Experimental data $\sigma(T)$ (left) with corresponding fits according to the METAL-or-PL model for PPy-Ag-s composites. Dependence of fitted parameters on σ_{RT} (right).

sample	Φ_{Ag} [vol.%]	σ_{RT} [S cm^{-1}]	ρ_{r} [S cm^{-1}]	α_{r} [K^{-1}]	a [S cm^{-1} K$^{-\gamma}$]	γ
PPy-Ag-s	17.9	3400	3.4×10^{-4}	3.0×10^{-3}	50	0.33
PPy-Ag-s	21.1	160	1.8×10^{-2}	3.4×10^{-3}	1.6	0.73
PPy-Ag-s	22.5	3500	3.2×10^{-4}	3.1×10^{-3}	34	0.33
PPy-Ag-s	24.6	1600	7.8×10^{-4}	3.1×10^{-3}	22	0.51
PPy-Ag-s	26.6	490	6.1×10^{-3}	3.0×10^{-3}	4.3	0.72

Table 3.12: Room temperature conductivity and results of fit of $\sigma(T)$ according to the METAL-or-PL model for PPy-Ag-s composites.

Since for some samples their conductivity does not meet expected dependence of silver volume (e.g. 21.1 vol.%) a plot of parameters against σ_{RT} was suggested instead (Fig. 3.18). Not surprisingly, both prefactors correspondingly follows the trend of increasing σ_{RT}. For very conducting samples (about 350 S cm^{-1}) the parameters of the PL model are less confident (with exponent forced to 0.33). Temperature coefficient of resistivity remains almost constant, ca. 3.1×10^{-3} K^{-1}. For PANI-Ag it was found higher, 4.2×10^{-3} K^{-1}.

3.3.3 Summary III

Two regions were observed in dependence of conductivity on silver volume ratio for various polymer-silver composites. First conductivity decreased (except insulating PANI-Ag base) up to Φ_c then it increased. Both regions were fitted with power law expressions, former with the phenomenological one, latter with the percolation law. For all systems Φ_c was found in range 18–27 vol.%. Samples exhibited either semiconducting behavior when CP determined transport or metallic when silver dominated.

Charge transport in semiconducting samples was explained within the heterogeneous CELT-or-ARH model for PPy-Ag and the MET-and-(CELT-or-ARH) model for PANI-Ag. The additional metallic term was suggested due to presence of MSA as dopant in agreement in previous results. Generally, higher level of disorder was observed with increasing content of silver. Effect of small decorating silver clusters enhancing heterogeneity and disorder in polymer matrix was suggested. Alternative explanation of changes in transport assumed the effect of varying oxidants ratios and template concentrations or variety of polymer morphology. However, both hypotheses alone seemed not very convincing to account for observed changes and more research is still needed to clarify dominating factor.

In metallic regime charge transport was explained within METAL-or-PL model fully driven by silver. Two contributions were assumed, first one characteristic for metallic silver well connected throughout samples and second one coming from large clusters probably near MIT transition. Even though conductivity could be directly related to presence of silver it was lower with its increasing volume content. Also change in polymer matrix morphology due to various synthesis conditions could be important despite its direct contribution to overall conductivity is negligible.

4. Stability of conducting polymers

4.1 Effect of water removal

Upon insertion of sample into vacuum, water is removed from sample. We believe the better understanding of the underlying physics/chemistry could be useful for the application of conducting polymers in electrical devices such as gas sensors but not limited to since all devices operate at ambient atmosphere with varying humidity and conductivity is one of the key property of CP.

4.1.1 Bulk materials

Decrease of conductivity in the majority of cases can be well correlated with escape of water from sample due to evaporation and diffusion. Since evaporation from sample surface occurs almost immediately, the process should be limited by the water diffusion. Then, the diffusion equation for the water content density ρ_c with appropriate boundary conditions[1], *e.g.* escape of water to vacuum from all side but one (the bottom side), has to be solved [167]:

$$\frac{1}{D}\frac{\partial \rho_c}{\partial t} = \frac{1}{r}\frac{\partial}{\partial r}\left(r\frac{\partial \rho_c}{\partial r}\right) + \frac{1}{r^2}\frac{\partial^2 \rho_c}{\partial \varphi^2} + \frac{\partial^2 \rho_c}{\partial z^2}. \tag{4.1}$$

in case of pellets (cylindrical coordinates) with boundary conditions for the height h and the radius R:

$$\rho_c(r,\varphi,z,t) = 0 \quad \text{when } z = h, \text{ or } r = R, \tag{4.2}$$

$$\frac{\partial \rho_c}{\partial z} = 0 \quad \text{for } z = 0. \tag{4.3}$$

The solution with initial spatially homogeneous water content c_0 reads [167]:

$$\begin{aligned}\rho_c(r,\varphi,z,t) =& \frac{8c_0}{\pi^2 R^2 h}\sum_{m=1}^{\infty}\frac{\mathrm{J}_0\left(\frac{\alpha_m}{R}r\right)}{\alpha_m\,\mathrm{J}_1(\alpha_m)}\exp\left[-\left(\frac{\alpha_m}{R}\right)^2 Dt\right] \\ &\times\sum_{n=0}^{\infty}\frac{(-1)^n}{2n+1}\cos\left[(2n+1)\frac{\pi z}{2h}\right]\exp\left[-\left((2n+1)\frac{\pi}{2h}\right)^2 Dt\right],\end{aligned} \tag{4.4}$$

[1]For notifications on the solutions of the diffusion equations and stimulating discussion Dr. A. Ryabov is fully acknowledged.

where α_m are the zeros of Bessel function J_0. After space integration the time dependence of the total amount of water in sample $c(t)$ (in wt.%) is given by:

$$c(t) = c_0 \frac{8}{\pi^2} \sum_{n=0}^{\infty} \left(\frac{1}{2n+1} \right)^2 \exp\left[- \left((2n+1) \frac{\pi}{2h} \right)^2 Dt \right] \times \sum_{m=1}^{\infty} \left(\frac{2}{\alpha_m} \right)^2 \exp\left[- \left(\frac{\alpha_m}{R} \right)^2 Dt \right], \tag{4.5}$$

which in the long-time limit is reduced to the simple exponential decay:

$$c(t) \sim c_0 \frac{8}{\pi^2} \left(\frac{2}{\alpha_1} \right)^2 \exp\left\{ - \left[\left(\frac{\alpha_1}{R} \right)^2 + \left(\frac{\pi}{2h} \right)^2 \right] Dt \right\}, \tag{4.6}$$

For instance, according to TGA results on PPy-NT in continuous He flow, the initial content of water was about 4 wt.% provided that complete water removal was assumed [168].

In addition to knowledge of water distribution inside a pellet, a link between $c(t, x, y, z)$ and $\sigma(t, x, y, z)$ had to be established. As the easiest way to link conductivity and water content the linear relationship with the 'strength' constant k was assumed:

$$\sigma(x, y, z) = \sigma_\infty + kc(x, y, z), \tag{4.7}$$

where σ_∞ has the meaning of asymptotic value, in particular, the conductivity in the absolutely dry state. The time dependence of conductivity is assumed to be solely given by $c(t)$ provided that all relaxation mechanisms related to conductivity changes are much faster. The form of Eq. 4.7 can be understood as the first-order approximation of general $\sigma(c(x, y, z))$ dependence, which should be valid for low values of water concentration. In order to obtain macroscopic (integral) value of conductivity numerical calculations by FEM were employed. In the method, the differential equation, Eq. (1.1), with appropriate boundary conditions was solved in weak form (the Galerkin method) [169] using mesh generator packed gmsh [170] and solver getdp [171]. A typical example of such simulation on mesh of pellet required known conductivity spatial distribution (e.g. (4.7)) and constant total currents at two current electrodes. As a result potential and current density maps were obtained (Fig. 4.1). The ideal positions of point-like probes were placed at corners of imaginary square. Since the concentration profile had an axial symmetry, the rotation of contacts could be omitted. Therefore, besides dimensions, only the total current (1 mA) and the total voltage ('measured') are needed to obtain the macroscopic conductivity according to Eq. (**??**).

Interestingly, the same linear relationship between the water content and the conductivity retained at the macroscopic level:

$$\sigma(t) = \sigma_\infty + kc(t). \tag{4.8}$$

This implies that the local distribution of water inside of pellet is irrelevant and the macroscopic measurement provides averaging. This is probably due to very smooth spatial variations of $c(x, y, z)$. In the following we analyzed the

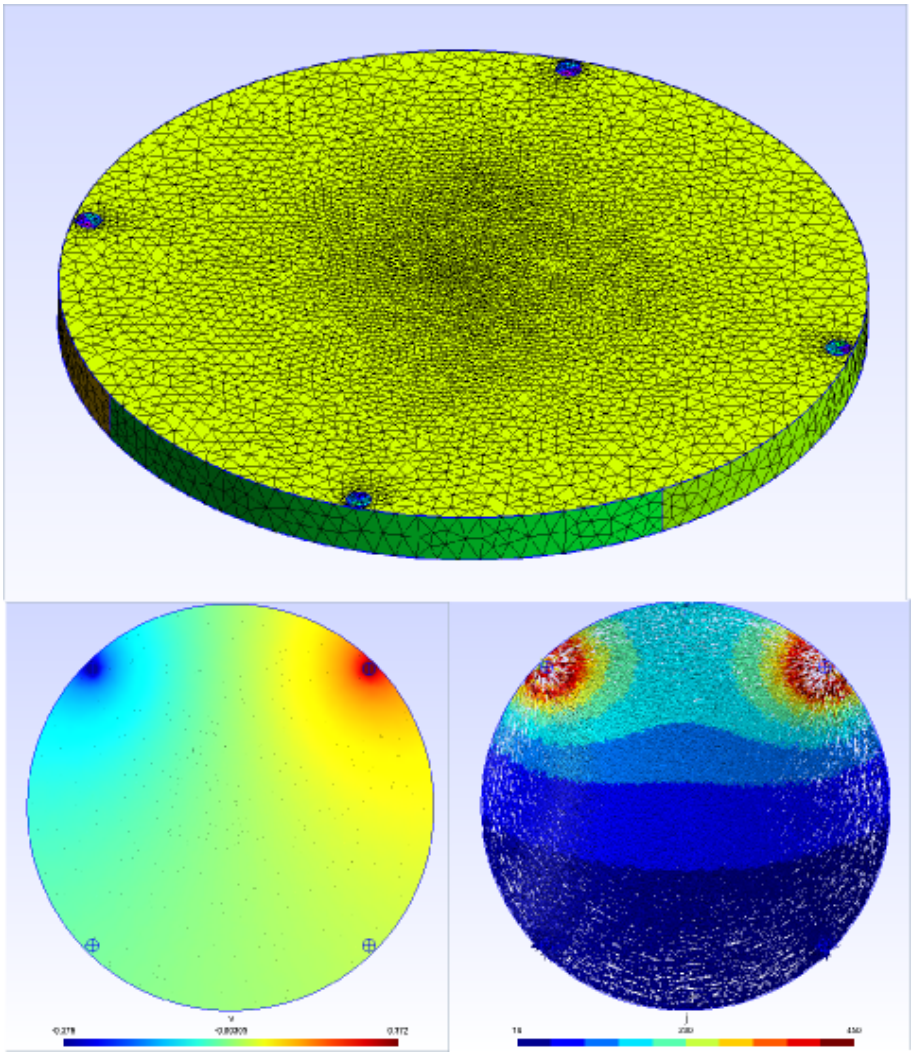

Figure 4.1: FEM solution of conductivity-water problem, $\sigma(c(x, y, z))$, in pellet. Example of mesh (top) and results in form of potential and current density maps (bottom).

long-term region with the simple exponential decay and the non-zero asymptotic conductivity σ_∞:

$$\sigma(t) = \sigma_\infty + \sigma_{\mathrm{kc}} \exp\left(-\frac{t}{\tau}\right), \tag{4.9}$$

where the pre-exponential factor σ_{kc} is proportional to product of the coupling constant and the initial water content kc_0. From relaxation time τ the diffusion constant was easily calculated D (Eq. (4.6), Eq. (4.7)) provided that thickness h was known.

Three regimes are apparent in a typical response to continuous pumping (Fig. 4.2), more pronounced in the first derivative; first, almost immediate conductivity drop related to the large change of pressure (and hence humidity) in the chamber. Second, the main conductivity decay accompanied with slow pressure decrease. Finally, conductivity decrease at almost constant pressure. In the last regime, application of the diffusion equation combined with the FEM calculation resulted in an excellent agreement between simulation and experiment, both in

full form of Eq. (4.8) and in the long-time limit, Eq. (4.12). This allowed estimation of the diffusion coefficient D, σ_∞ and σ_{kc} from the latter simple exponential function. In our samples D of order $10^{-7}\,cm^2\,s^{-1}$ was obtained. The second regime could not be explained within the proposed model. However, there are at least two shortcomings in this diffusion-based model since it does not account for pressure change (albeit small), and it assumes only linear relationship between conductivity and water concentration. The model could be further extended to account for time-dependent boundary conditions (Eq. (4.2)) and higher order (at least quadratic) terms in Eq. (4.8). In the following we focus mainly on the long-time limit to obtain D and σ_∞ for various samples and the results are summarized in Table 4.1.

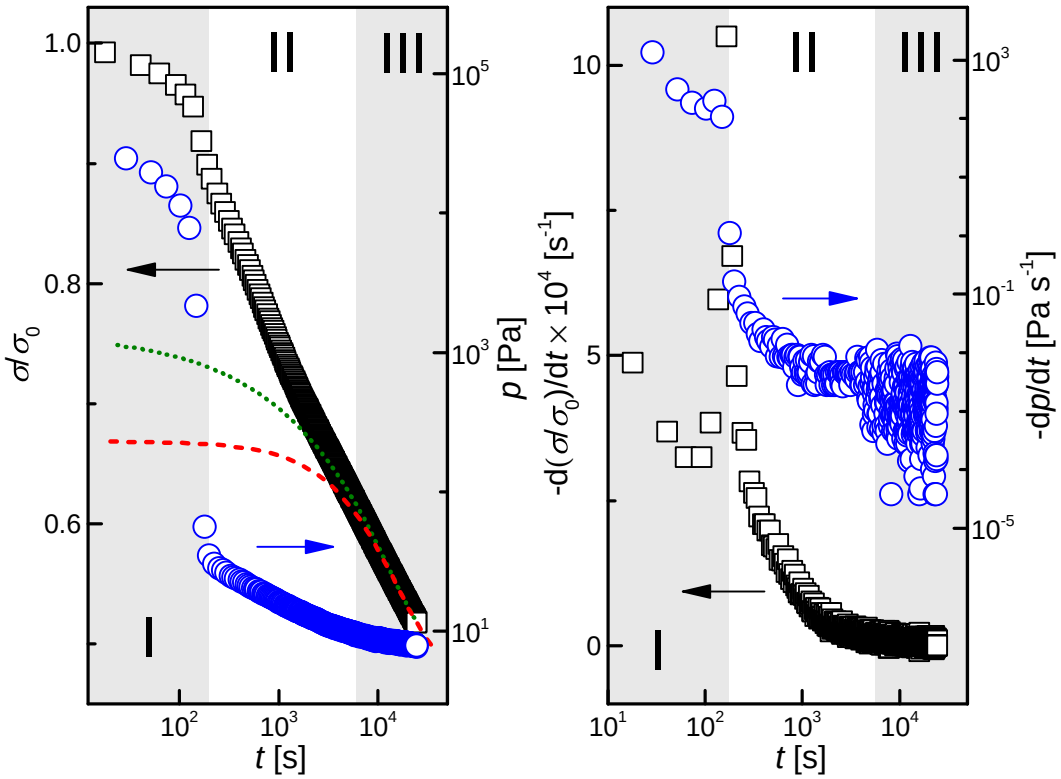

Figure 4.2: Typical response of conductivity $\sigma(t)$ (left) to dynamic vacuum (with $p(t)$) with fit to the diffusion-based model represented by Eq. (4.8) (dot) or to its long-time limit, Eq. (4.12) (dash). The time derivative of response (right).

The response of three subsequent runs (with about one week interval) can give insight of the water release (Fig. 4.3). The first run had the smallest response. It seems that water reabsorbed is released faster in next runs. Another conclusion from repeated measurements is that conductivity never recovers its initial value after drying process and subsequent water reabsorption. The new equilibrium state thus differs from the previous one, maybe due to some structural relaxations. The estimated value of $D = 1.8 \times 10^{-7}\,cm^2\,s^{-1}$ is only for orientation since it varies. The same is true for asymptote since it was found as low as 0.5 for sample from another batch (Fig. 4.2, 4.3).

The common conductivity drop to 50-60% of initial conductivity for PANI prepared at various T_p (Fig. 4.4) is in the agreement with previous. The rea-

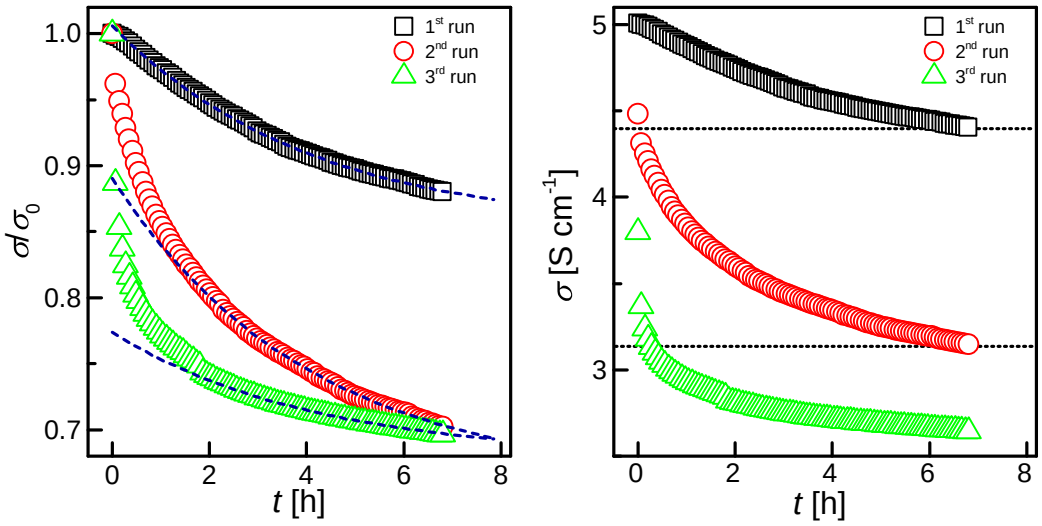

Figure 4.3: Evolution of conductivity in dynamic vacuum $\sigma(t)$ for PANI-G-APS for three subsequent runs (left), and normalized to initial value (right).

sons for two discrepancies are not obvious. We can only speculate about slighter decrease in the case of $-20\,^{\circ}\mathrm{C}$ due to the different structure, *e.g.* a higher crystalline/amorphous phase ratio [137]. The same is true for PANI-$FeCl_3$-MSA samples doped at various acid concentrations. The exception is the highest one which is practically constant. Among others it exhibits the highest order in sense of T_0^{M}. In PANI we thus observe generally the same behavior regardless the synthesis conditions with only hypothetical exceptions in case of more ordered samples.

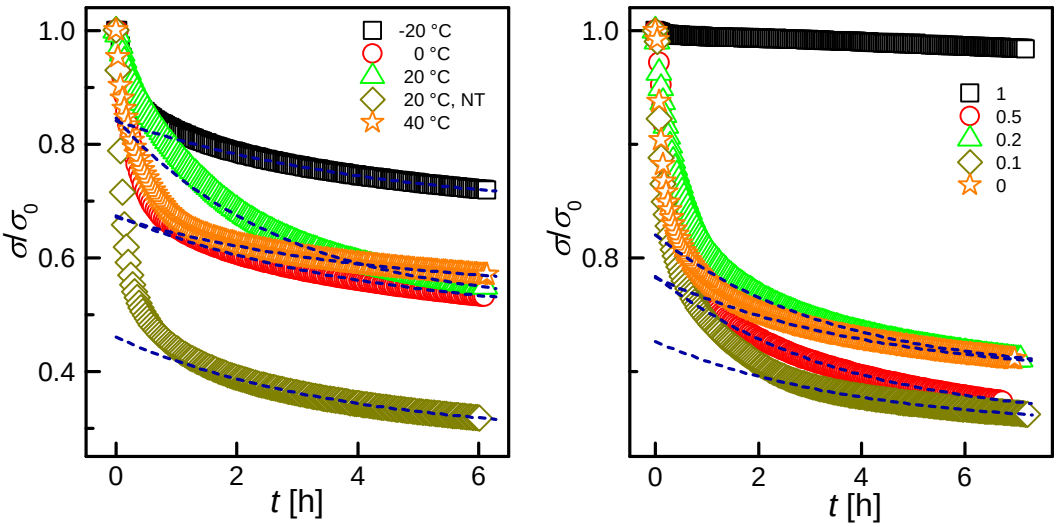

Figure 4.4: Evolution of conductivity in dynamic vacuum $\sigma(t)$ for PANI-G-APS prepared at various T_{p} (left, adopted from Ref. [137]), and for PANI-G-$FeCl_3$ with various c_{MSA} (right).

For PPy samples the situation is different for granular and nanotubular samples (Fig. 4.5). While granular ones show similar trend as PANI samples the nanotubular form is very stable with only negligible increase. It is not the value of conductivity which determines the response since two PPy-NT vary in conductivity in one order of magnitude. Further complication is slight conductivity

increase of unknown origin in both PPy-NT-APS and PPy-G-APS. Decrease of PPy conductivity due to the presence of water in atmosphere was also reported in electropolymerized PPy tetrafluoroborate [172]. The concept of granularity as the key parameter in dynamic vacuum response seems to be supported by measurements on PPy synthesized with various template where some portion of the granular phase was found. It was pronounced mainly when sunset yellow is used (Fig. 3.11) what can be here related to the highest response to drying.

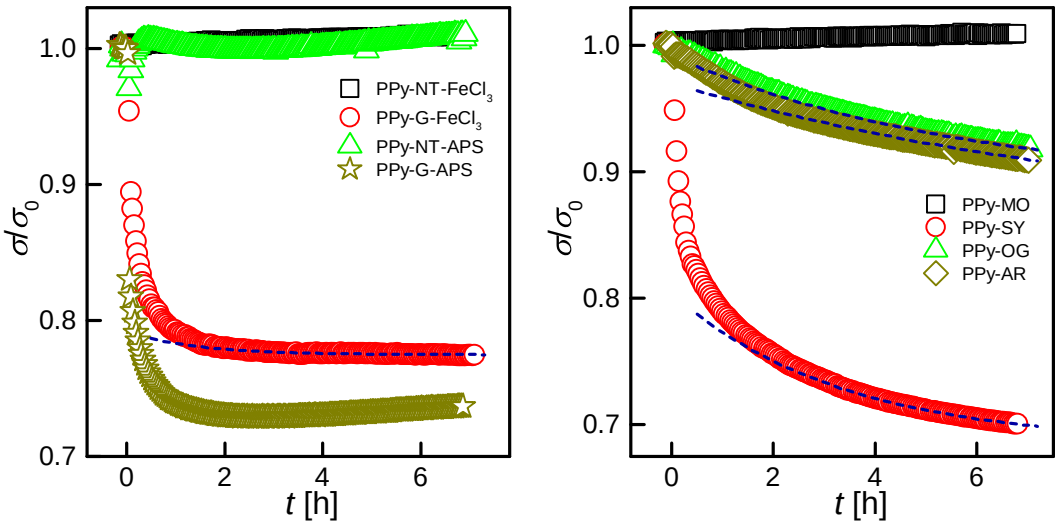

Figure 4.5: Evolution of conductivity in dynamic vacuum $\sigma(t)$ for PPy prepared at with various oxidants (left), and for PPy prepared with various templates (right).

To conclude, samples subjected to simple exponential decay fit (with an exception of PPy-G-$FeCl_3$ with generally worse fit) had D within the same order of magnitude regardless of synthesis details. It seems that water is similarly trapped (or bounded) in PANI and PPy of granular morphology.

4.1.2 Thin films

Effect of water removal turned out even more important for thin films probably due to the large surface-volume ratio. Two experiments were performed, drying in a nitrogen flow scanned with two probe measurement and drying in dynamical vacuum scanned with the four probe measurement (vdP). Apparently, different time profile is due to different experimental conditions. The asymptotic value varies significantly (also for other acids, not shown), but up to now, it is not clear whether it comes from experimental conditions or from variability in samples. Similarly to bulk materials there are two regions of conductivity decrease (Fig. 4.6). The conductivity drop can be about 0.1 or 0.01 of initial value (Fig. 4.6), significantly larger than in pellets. We present results for various dopants used for reprotonation, on first look there is a tendency, the larger sulfonic acid the larger drop. However, one should be careful in overestimation of such result since the response can vary from sample to sample due to various

sample	σ_0 [S cm^{-1}]	σ_∞ [S cm^{-1}]	σ_{kc} [S cm^{-1}]	τ [h]	D [cm^2 s^{-1}]
PANI-APS: 1st run	5.0	4.3	0.77	4.1	1.8×10^{-7}
PANI-APS: 2nd run	4.5	3.0	1.0	4.0	1.9×10^{-7}
PANI-APS: 3rd run	3.8	2.6	0.36	4.1	1.8×10^{-7}
PANI-APS-T_p: −20 °C	2.1	1.4	0.34	4.5	3.7×10^{-7}
PANI-APS-T_p: 0 °C	3.9	1.9	0.73	4.2	3.0×10^{-7}
PANI-APS-T_p: 20 °C	4.2	2.2	1.4	2.8	1.8×10^{-7}
PANI-APS-T_p:20 °C, NT	5.6	1.7	1.0	3.7	5.7×10^{-7}
PANI-APS-T_p:40 °C	1.7	0.9	0.22	4.1	4.0×10^{-7}
PANI-$FeCl_3$-MSA:0	1.5	1.1	0.14	4.3	4.3×10^{-7}
PANI-$FeCl_3$-MSA:0.1	1.8	1.2	0.14	3.9	5.7×10^{-7}
PANI-$FeCl_3$-MSA:0.2	3.0	2.1	0.37	3.4	2.2×10^{-7}
PANI-$FeCl_3$-MSA:0.5	11	7.4	1.4	3.6	3.6×10^{-7}
PPy-SY	1.3	0.7	0.12	3.3	6.5×10^{-7}
PPy-OG	8.6	0.9	0.10	5.7	3.3×10^{-7}
PPy-AR	2.0	0.9	0.12	9.7	2.1×10^{-7}
PPy-G-$FeCl_3$	2.1	0.8	0.02	1.4	2.1×10^{-6}

Table 4.1: Initial conductivity (for PANI-APS-T_p reproduced from [137]), fit parameters of conductivity exponential decay and related diffusion coefficient D for various PANI and PPy samples.

initial water content what we believe that is hardly possible to control during CP synthesis.

Analogously to pellets, for thin films solving the Eq. (4.1) in appropriate coordinates with boundary conditions and spatial integration for the long-time limit one obtains for the total amount of water $c(t)$ [167]:

$$c(t) \sim c_0 \frac{64}{\pi^3} \exp\left\{ -\left[\left(\frac{\pi}{2h}\right)^2 + \left(\frac{\pi}{l_x}\right)^2 + \left(\frac{\pi}{l_y}\right)^2 \right] Dt \right\}, \tag{4.10}$$

with lateral dimensions of sample l_x and l_y. Hence, we expected corresponding conductivity to be in the same form of Eq. (4.12). The application of this diffusion model, is however rather questionable, it covers only very small change in conductivity, and due to tiny thickness (≈ 100 nm) the diffusion coefficient is of order 10^{-14} cm^2 s^{-1} which is unreal value. Obviously, the real diffusion in films is much faster (and thus undetectable) and the real underlying process remains unknown. Moreover, in the model we neglected the film's significant roughness (Fig. 3.8). Another important question to address is the real role of water molecules in the charge transport in CP. Only recently, based on the atomistic simulations (bridged with FEM) it has been suggested that the main effect of water is enhancement of doping level due to stabilization of protonated sites [100]. Albeit good agreement

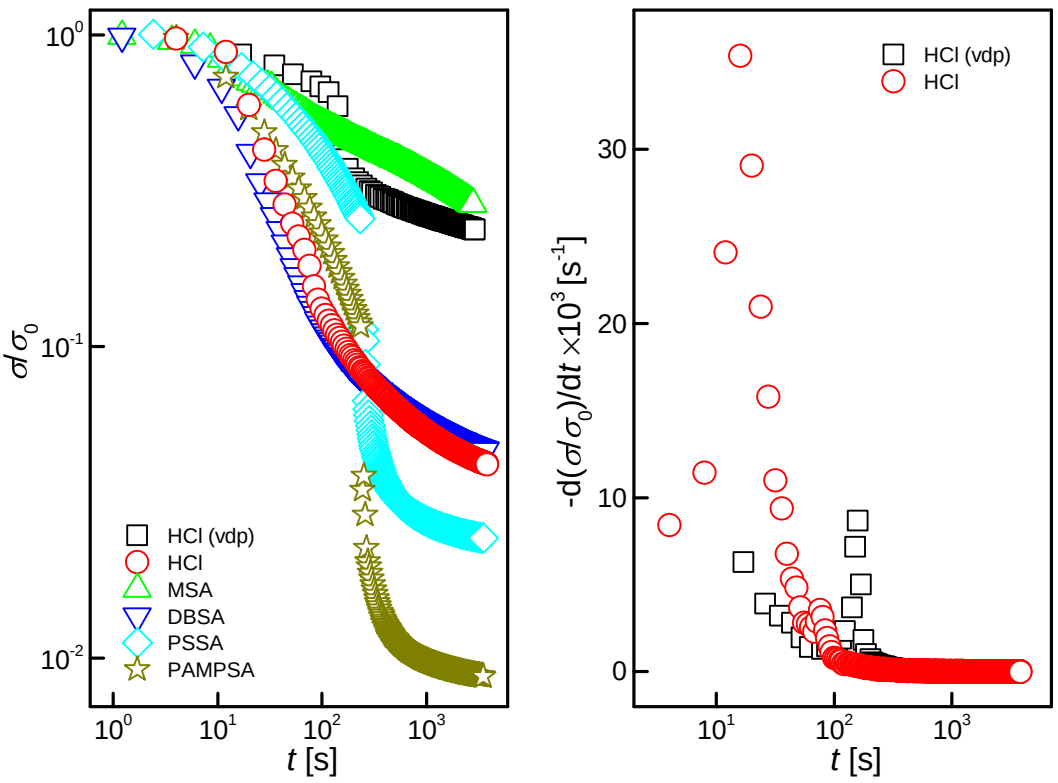

Figure 4.6: Time dependence of conductivity $\sigma(t)$ during drying for PANI films reprotonated with various sulfonic acids (left), and its time derivative (right).

between theory and experiment, the diffusion coefficient extracted from the model was $10^{-11}\,\mathrm{cm^2\,s^{-1}}$. It is questionable that only stabilization of protonated sites (with no other deprotonation mechanism) could be the cause of one-two orders of magnitude change in conductivity. We believe, alternative explanation should still be found but the bridging of various multiscale approaches seems promising and it is encouraging that the field is still scientifically active.

4.1.3 Summary IV

The effect of water removal, achieved by either dynamic vacuum or a dry nitrogen flow, on conductivity was discussed in this section. Three regions were observed, first one with almost immediate conductivity drop connected to orders of magnitude pressure drop, followed by slower but intense conductivity decay with small pressure decrease ended up with slow and slight conductivity decay at almost constant pressure. In the case of bulk materials (pellets), the solution of the diffusion equation for water which provided the local concentration $c(x, y, z, t)$ was combined with the local conductivity $\sigma(x, y, z, t)$ in FEM simulations with assumption of simple linear relationship. As a result, the same link was observed between the total water content and the overall conductivity. This model was used to explain the third regime and good agreement was achieved especially in the long-time limit. A diffusion constant of order $10^{-7}\,\mathrm{cm^2\,s^{-1}}$ was estimated from experimental data. However, in case of thin films, this discrepancy was

much larger and alongside with unrealistic $D \approx 10^{-14}\,\mathrm{cm^2\,s^{-1}}$ from the long-time limit, validity of such diffusion-based model was seriously questioned.

From the three subsequent measurements on sample which was after each measurement left at ambient condition we found out that conductivity was never fully recovered and new equilibrium state is established after such treatment and that the first stage of conductivity drop became faster, probably due to only loosely trapped reabsorbed water. From the analysis of various PANI samples it turned out that the similar response to water loss is always present with only few exceptions, probably for more ordered samples. In case of PPy, samples with nanotubular morphology turned out to be stable in vacuum and with increasing granular phase, the behavior similar to PANI was observed. Measurements on thin films revealed much stronger effect of water on conductivity comparing to compressed powder.

4.2 Effect of deprotonation in alkaline media

Since the deprotonation for PANI is more or less known [12] (and routinely applied for reprotonation [93]) in the following we focus mainly on PPy-NT which seem more promising in their conducting state and the deprotonation of bulk material is up to our knowledge far less common, since the most of investigations were carried out on electropolymerized films as were mentioned in Chap. 1. For investigation of the electrical properties, both DC (vdP method) and AC measurements (capacitor-like measurements) were employed. The results for PPy-NT immersed in aqueous solutions of NaOH or NH_4OH with various molar concentration within 0.01 M–14.7 M are plotted in Fig. 4.7. Conductivity is obviously dependent on a strength of alkaline media, and it seems that both have their unique dependence. However, the tendency is slightly disrupted by the effect of aging (about 2 weeks), since the conductivity is rapidly decreasing with time as discussed in the next Sec. 4.3. High frequency ϵ'(at 1 MHz, −150 °C) is used as a kind of conductive state probe since for more conducting samples it departs more from the ϵ'_∞ limit. For instance, the dielectric constant reflects the contribution of the localized states when the VRH model is considered [39].

4.2.1 Charge transport in DC regime

For less deprotonated samples $\sigma(T)$ was measured by the vdP method (Fig. 4.8), for the rest of samples DC conductivity was extracted only from $\epsilon''(f)$ spectra and is discussed later (Fig. 4.11). The vdP data were evaluated using the CELT-or-ARH model in agreement with less conducting PPy samples (Sec. 3.1). For comparison, sample treated in water is included. Interestingly, PPy-NT immersed in water exhibit similar conductivity than as salt forms with other oxidants used for synthesis. As expected, disorder parameters T_0^{C} and T_0^{A} are increasing with the higher level of deprotonation. Particularly, the ratio s/d related to (bi)polaronic

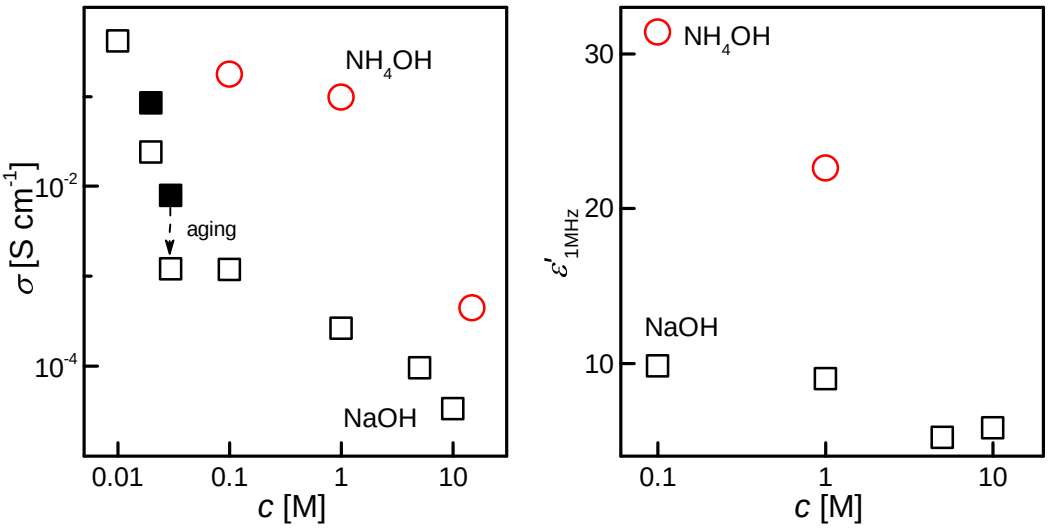

Figure 4.7: Dependence of conductivity (left) and high frequency permittivity (right) on the molar concentration of alkaline media.

clusters and their spacing increases when we admit the validity of the Zuppiroli's CELT model. Alongside, the activation energy for the second contribution increases. The values of these parameters are similar to reprotonated PANI films. It seems that PPy-NT are highly resistive to deprotonation since they still exhibit the transport comparable to PANI salts. The precision of fitted parameters is, however, highly limited due to HT region only. The less confident fit is particularly emphasized at $W(T)$ plot.

alkaline medium	σ_{300} [S cm^{-1}]	σ_0^{C} [S cm^{-1}]	T_0^{C} [K]	σ_0^{A} [S cm^{-1}]	T_0^{A} [K]
none (H_2O)	4.2	85	3300	38	1050
NaOH-0.01 M	0.45	340	1.5×10^4	74	1900
NH_4OH-0.1 M	6.6×10^{-2}	110	2.1×10^4	26	1900
NaOH-0.015 M	1.8×10^{-2}	280	3.3×10^4	28	2400
NaOH-0.1 M	1.3×10^{-3}	1400	6.6×10^4	40	3200
NaOH-1 M	2.4×10^{-4}	8.8×10^4	1.2×10^5	–	–

Table 4.2: Results of fitting according the CELT-or-ARH model for deprotonated PPy-NT.

4.2.2 Charge transport in AC regime

The frequency dependence of complex conductivity, in principle, could have been modeled with the 'universal' power law with the onset frequency f_c and subsequent interpretation of the exponent s according to the variety of microscopic models. The fit of real part, $\sigma'(f)$, was almost satisfactory achieved (Fig. 4.9). However, the fit of the imaginary part, $\sigma''(f)$, turned out to be problematic for the

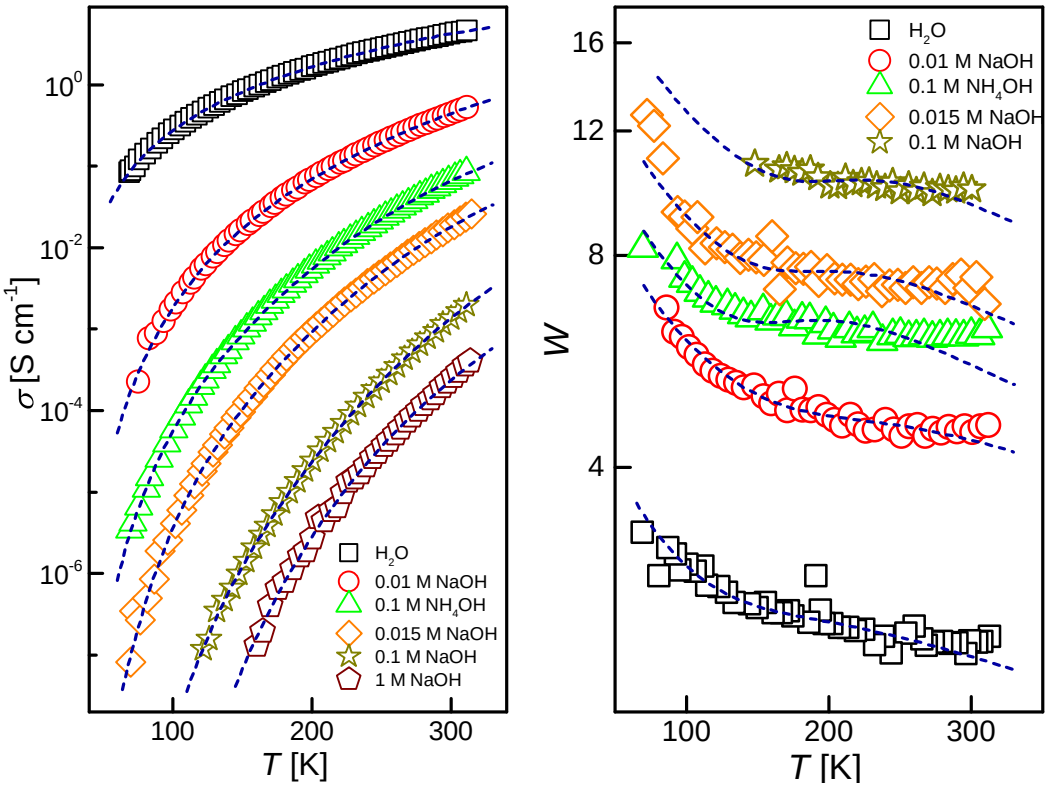

Figure 4.8: Experimental data for $\sigma(T)$ (left) and $W(T)$ (right) and the fit according to the CELT-or-ARH model for PPy-NT deprotonated with various alkaline solutions or water.

RFEB model (Eq. (1.35)), its generalization in the GM framework by EMA in the Bianchi's model (Eq. (1.44)). The same was true for the VRH model, moreover, with the issue of the inconsistent temperature dependence of s exponent with the prediction of the model. The precise determination of the exponent was not possible mainly at higher temperatures due to narrow frequency-dependent region. The onset frequency was found proportional to the DC conductivity (Fig. 4.10) as it is commonly observed [70].

An alternative technique is the use of phenomenological description by complex dielectric function of the HN type (Eq. (1.50)). Since 2-3 such functions had to be used for satisfactory fit, the symmetrical response of CC was chosen in order to reduce the number of adjustable parameters. This approach resulted in reasonable fit of both, the real and the imaginary part of permittivity for the price of the lost connection to the particular microscopic model. Apart of significant DC conductivity contribution, the most prominent peak I (Fig. 4.11) with the dielectric strength, $\Delta\epsilon \approx 23$–$60$ was observed in ϵ'' spectra. The second one (II) with $\Delta\epsilon \approx 10^3$ was deduced only from ϵ' spectra where it was not masked by σ_{DC}. Another contribution was found at higher frequencies with considerably smaller $\Delta\epsilon \approx 10^{-1}$. While first two relaxations can be regarded as consequence of conducting regions, the third one is probably of the dipolar origin. Only the first peak was possible to observe at reasonably wide temperature and frequency range. Hence, attention is paid to this particular one (Table 4.3). The activation energy for both, relaxation process and DC conductivity, was determined from

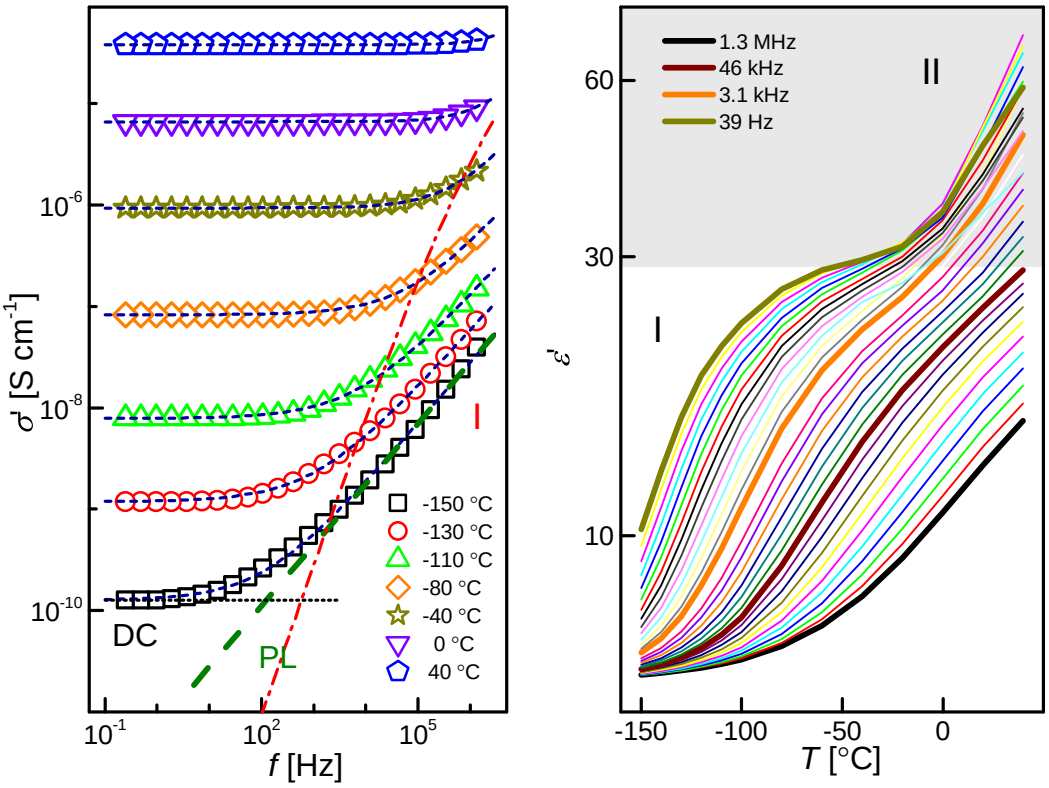

Figure 4.9: Experimental results for $\sigma'(f)$ with corresponding fits to the power law model with DC plateau compared to the CC model fit (I) (left) and $\epsilon'(T)$ (right) for PPy-NT deprotonated in 10 M NaOH.

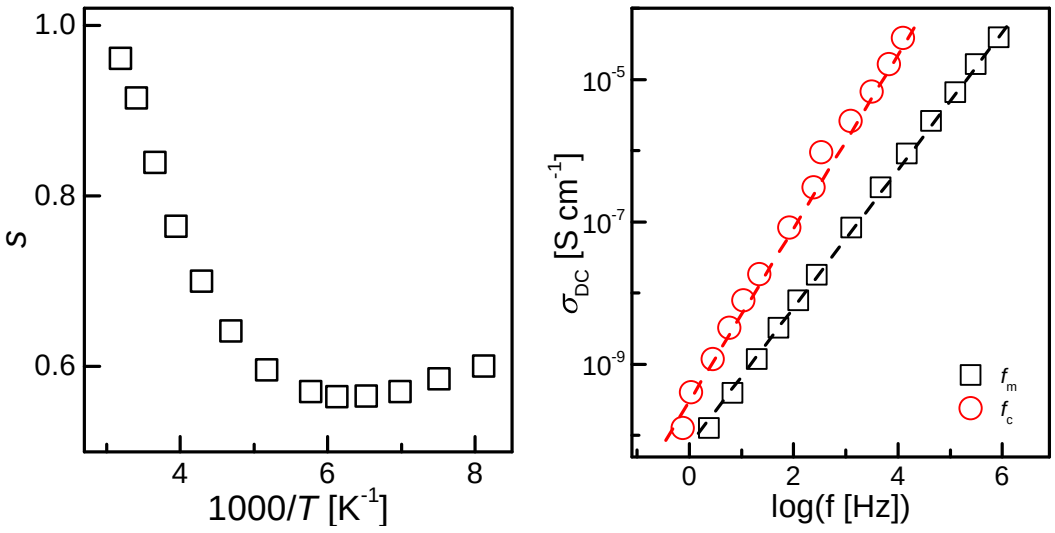

Figure 4.10: Results of fitting for PPy-NT prepared in 10 M NaOH. Temperature dependence of the power law exponent (left) and relationship between σ_{DC} and the characteristic frequency f_{c} and f_{m} (right) for the power law model and the CC model, respectively.

the so-called Arrhenius plot according to Eq. (1.51) (Fig. 4.13). Similar values of E_{A} for both processes are apparent from their proportionality (Fig. 4.10). Thus, they have the same origin. An example of dependence of AC response on alkaline

concentration is shown at least for −120 °C at Fig. 4.12. While f_m and σ_{DC} could be easily related to the strength of alkaline media, the dielectric strength does not exhibit this trend. The Arrhenius plot (Fig. **??**) was constructed from all available temperature scans and activation energies were obtained.

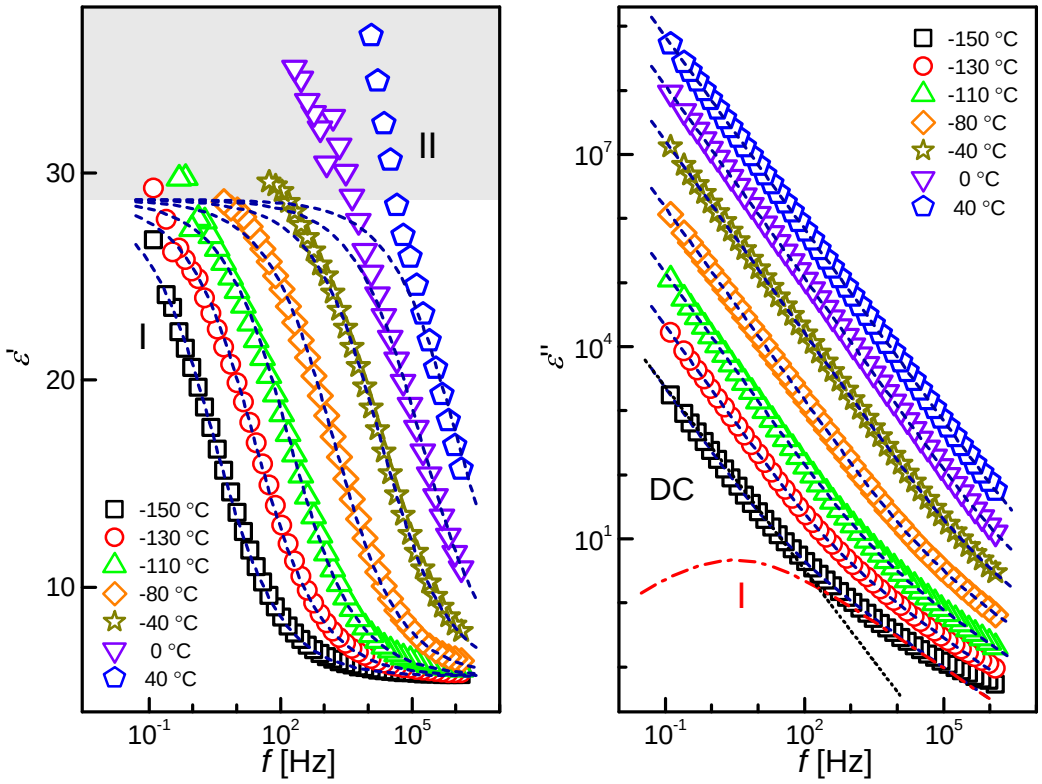

Figure 4.11: Experimental results for $\epsilon'(f)$ (left) and $\epsilon''(f)$ (right) with corresponding fits to the CC model with σ_{DC} contribution for PPy-NT deprotonated in 10 M NaOH.

Despite the lack of knowledge of appropriate microscopic model, the presence of relaxation behavior in AC spectra was attributed to intrachain and interchain (or inter/intragrain) hopping [92]. These two contributions were split either by pressure or by aging [92]. However, it is not probably not our case of peak I and II. We obtained almost the same E_A for DC conductivity contribution and AC relaxation as commonly observed [71] but in contrast to Ref. [90]. The activation energies are probably temperature dependent, the existance of two regions is only approximation. From vdP measurements we found DC conductivity well explained by the CELT-or-ARH model, and similar complex temperature dependence is expected of the AC response. We believe that the AC response is due to granular structure of material induced by deprotonation but the particular non-empirical model was not found since the commonly used microscopic models failed.

alkaline medium	T [°C]	σ_{DC} [S cm^{-1}]	log f_m	$\Delta\epsilon$	ϵ_∞	α	E_A^f [eV]	E_A^s [eV]	s	log f_c
NaOH 10M	40	3.9×10^{-5}	6.0	23	5.7	0.49	0.32	0.33	0.60	-0.02
	20	1.6×10^{-5}	5.6	23	5.7	0.49	0.32	0.33	0.59	0.13
	0	6.6×10^{-6}	5.2	23	5.7	0.49	0.32	0.33	0.57	0.56
	-20	2.6×10^{-6}	4.7	23	5.7	0.49	0.32	0.33	0.57	0.88
	-40	9.1×10^{-7}	4.3	23	5.7	0.49	0.32	0.33	0.56	1.17
	-60	3.0×10^{-7}	3.8	23	5.7	0.49	0.32	0.33	0.57	1.31
	-80	8.2×10^{-8}	3.2	23	5.7	0.49	0.32	0.33	0.60	1.46
	-100	1.8×10^{-8}	2.5	23	5.7	0.49	0.18	0.33	0.64	2.63
	-110	7.9×10^{-9}	2.2	23	5.7	0.49	0.18	0.18	0.70	2.77
	-120	3.2×10^{-9}	1.8	23	5.7	0.49	0.18	0.18	0.76	2.92
	-130	1.2×10^{-9}	1.4	23	5.7	0.49	0.18	0.18	0.84	3.08
	-140	4.0×10^{-10}	0.9	23	5.7	0.49	0.18	0.18	0.91	3.78
	-150	1.3×10^{-10}	0.5	23	5.7	0.49	0.18	0.18	0.96	4.09
NaOH 1M	40	2.6×10^{-4}	6.2	56	12	0.51	0.28	0.31	–	–
	20	1.1×10^{-4}	5.9	56	12	0.51	0.28	0.31	–	–
	0	4.7×10^{-5}	5.5	56	12	0.51	0.28	0.31	–	–
	-20	1.8×10^{-5}	5.0	56	12	0.51	0.28	0.31	–	–
	-40	6.0×10^{-6}	4.4	56	12	0.51	0.28	0.22	–	–
	-80	5.7×10^{-7}	3.6	56	12	0.51	–	0.22	–	–
	-100	1.2×10^{-7}	2.9	56	12	0.51	–	0.22	–	–
	-120	1.7×10^{-8}	2.1	60	12	0.51	–	0.22	–	–
	-140	1.4×10^{-9}	1.1	60	12	0.51	–	0.22	–	–
NaOH 0.1M	30	1.1×10^{-3}	–	35	13	0.53	0.20	0.24	–	–
	0	3.5×10^{-4}	6.7	35	13	0.53	0.20	0.24	–	–
	-30	9.7×10^{-5}	6.2	35	13	0.53	0.20	0.24	–	–
	-60	2.3×10^{-5}	5.6	35	13	0.53	0.20	0.24	–	–
	-90	3.8×10^{-6}	4.8	35	13	0.53	–	0.17	–	–
	-120	3.4×10^{-7}	3.9	35	13	0.53	–	0.17	–	–
	-150	1.4×10^{-8}	2.6	35	13	0.53	–	0.17	–	–

Table 4.3: Results of fit of $\epsilon^*(f, T)$ according to the CC model with σ_{DC} contribution for various PPy-NT bases and results of fit according to the power law model for sample prepared in 10 M NaOH.

4.2.3 Summary V

The stability of PPy-NT in various alkaline media was tested. Conductivity decreased from initial 10^1 to 10^{-4} S cm^{-1} in very strong solutions of NaOH. This is much more resistive than PANI in much weaker alkaline solution [12]. The charge transport in the DC regime was interpreted withing the CELT-or-ARH model, generally found for less conducting PPy samples. In the AC regime, besides significant DC contribution, at least two relaxation mechanism were found and fitted with the phenomenological CC formula since other models failed. According to the strength of relaxations $\Delta\epsilon \approx 10^1$ and 10^3 it was assumed to be connected with conducting phenomena rather than dipolar one. It was confirmed with by

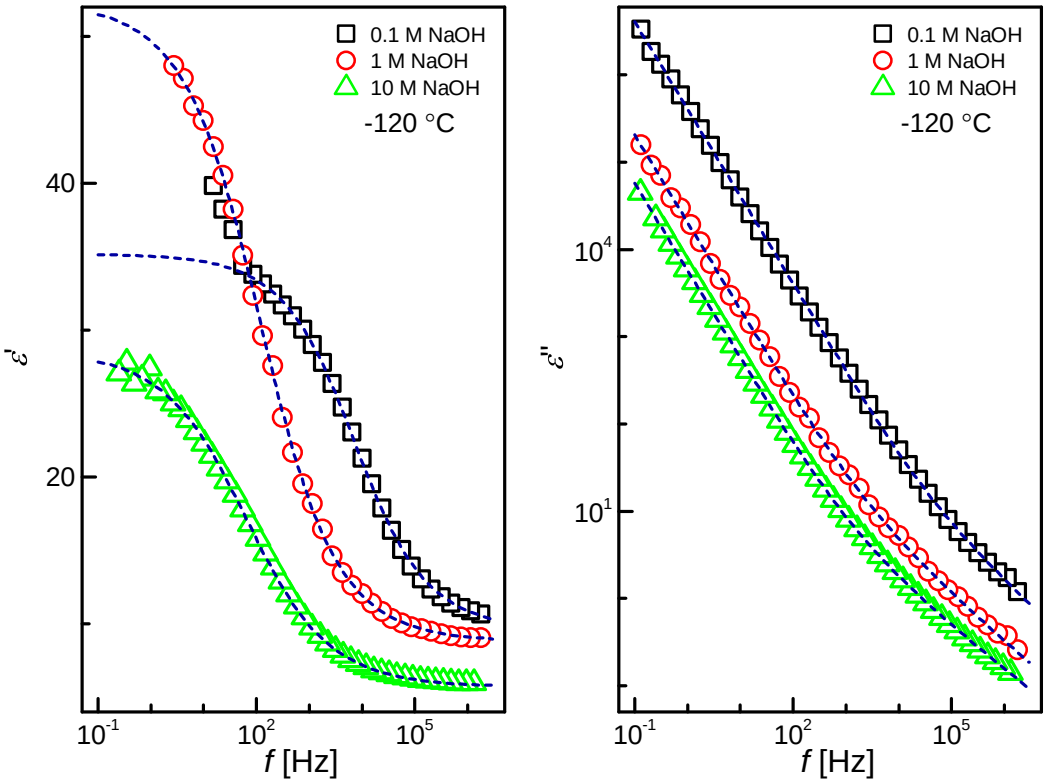

Figure 4.12: Experimental results at $-120\,^{\circ}\mathrm{C}$ for $\epsilon'(f)$ (left) and $\epsilon''(f)$ (right) with corresponding fits to the CC model with σ_{DC} contribution for PPy-NT deprotonated in various NaOH concentrations.

the proportionality with the DC contribution and the same activation energies. These were found to be temperature dependent and in the first approximation, two regions of constant value were marked. Higher values were found for stronger solutions. From DC measurements it was found that deprotonation results in heterogeneous structure but in AC domain, the corresponding model which could help to clarify the underlying process is still missing.

4.3 Decay of conductivity due to aging

The long-term stability of material is important from the application point of view. In this section we report both, long-term aging ranging two years at natural ambient and accelerated aging induced by elevated temperatures. Again, PPy-NT are of the main interest here, occasionally compared to 'standard' PANI-G-APS(HCl). We discuss separately treatment at mild temperatures, below $70\,^{\circ}\mathrm{C}$, and higher temperatures, above $100\,^{\circ}\mathrm{C}$. Apart of the speed of aging which is influenced by temperature, different processes were assumed at mild and high temperatures for PPy [84].

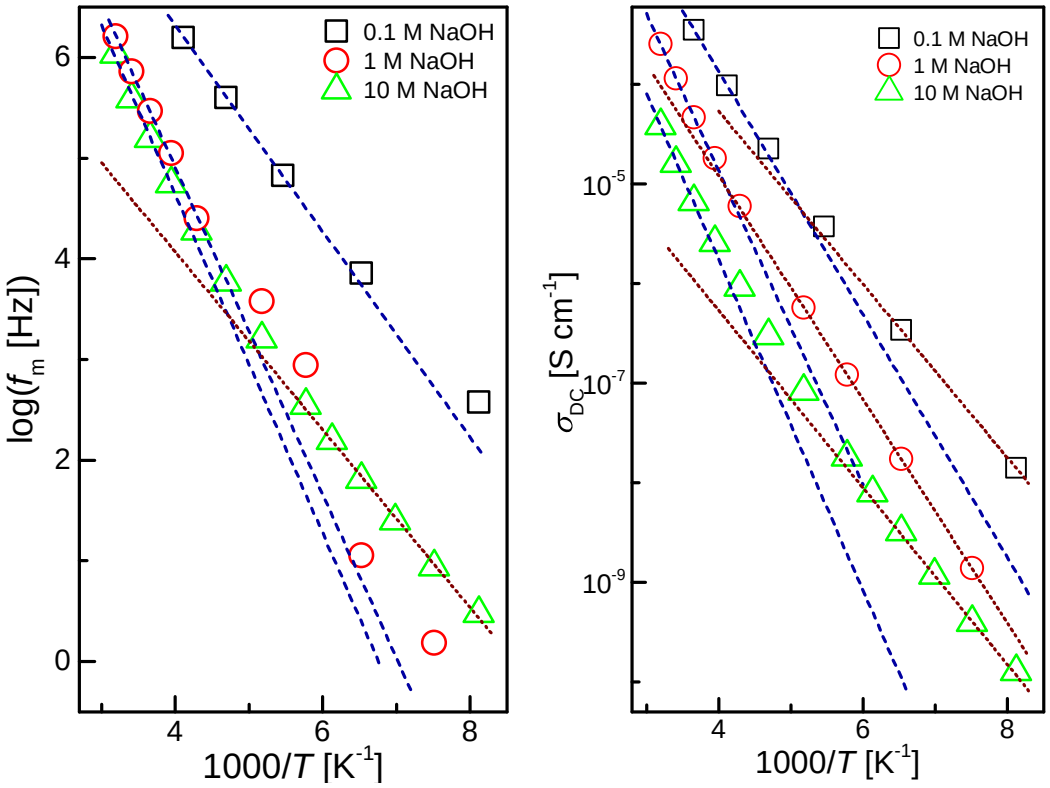

Figure 4.13: The Arrhenius plot for the frequency maxima of loss peak (left) and σ_{DC} (right) for PPy-NT deprotonated in various NaOH concentrations

4.3.1 Natural aging at ambient atmosphere

The time evolution of conductivity was analyzed either by fitting the stretched-exponential form [173] adapted in form:

$$\sigma(t)/\sigma_0 = A \exp\left(\left(-\frac{t}{\tau}\right)^n\right), \tag{4.11}$$

with the characteristic decay time τ. Additional dimension-less parameter A was included for better fit agreement when n was fixed. Alternatively, the simple exponential decay observed experimentally was used [82]:

$$\sigma(t)/\sigma_0 = \exp\left(-\frac{t}{\tau}\right), \tag{4.12}$$

which can be obtained from various approaches such as decay due to increase of intergrain defects with the linear rate of their creation [88] or the diffusion process as we previously showed for water.

The evolution of conductivity in time at natural ambient storage (variations in temperature, humidity, sunlight) for PPy-NT and corresponding base form (prepared with various alkaline solutions) for period about 1–2 years is summarized on Fig. 4.14. If the simple exponential decay is assumed, Eq. (1.52), the initial aging could not be fitted, however, longer times exhibited good agreement except salt form where after some time a new decay phase began. The data for

PPy-NT salt form are little scattered due to compilation of samples from various batches with uncertain date of synthesis, on the other hand it is statistically stronger result that for base form, where particular samples were selected and re-measured from time to time. The trend of steeper conductivity decay is apparent for less conducting samples. Other important observation is that sample already in compact form (pellet) is generally aging faster than corresponding powder. The results for simple exponential decay with asymptotic value σ_∞ are summarized in Table 4.4. The dependence on the alkaline molar concentration is more continuous than reported in previous section, hence the disruption was indeed caused by aging. Moreover, it seems that at strong solutions conductivity tends to saturate and further deprotonation can not be achieved. The half life time for PPy-NT bases could not be reliably determined due to missing short-term aging data. The characteristic time of relaxation (aging) process is generally in order of several months (with two exceptions where long-term data were not available).

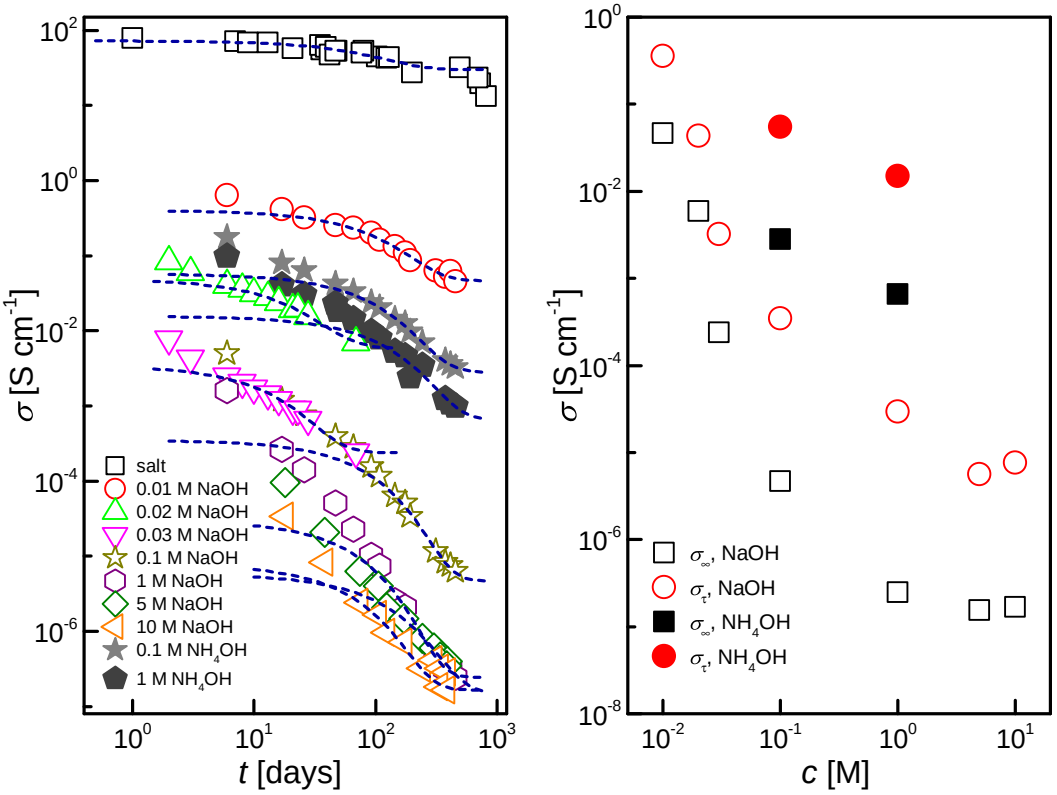

Figure 4.14: Decay of σ_{RT} for various PPy-NT sample due to aging at ambient conditions (left) and dependence of fit parameters on the molar concentration of alkaline solution.

The effect of natural aging within on PPy-NT base was probed with dielectric spectroscopy as well. For brevity, only one temperature is selected (Fig. 4.15). In analogy to the previous analysis, the CC model with DC contribution were used and the Arrhenius plot (Fig. 4.16) was constructed from all measured data as summarized in Table 4.5. General feature of aging is slight decrease in the width of loss peak related to α, decrase of DC conductivity and increase of $\Delta\epsilon$. If we assume the GM picture, hypothetically, decrease in the size conducting islands which account for the decay of DC conductivity due to aging [86] can change the

alkaline medium	σ_∞ [S cm^{-1}]	σ_0 [S cm^{-1}]	τ [days]	$t_{0.5}$ [days]
NaOH-0.01 M	4.6×10^{-2}	3.5×10^{-1}	100	–
NaOH-0.02 M	5.9×10^{-3}	4.3×10^{-2}	19	5.3
NaOH-0.03 M	2.4×10^{-4}	3.2×10^{-3}	14	3.9
NaOH-0.1 M	4.7×10^{-6}	3.4×10^{-4}	82	–
NaOH-1 M	2.5×10^{-7}	3.0×10^{-5}	63	–
NaOH-5 M	1.5×10^{-7}	5.6×10^{-5}	116	–
NH_4OH-0.1 M	2.8×10^{-3}	4.4×10^{-2}	96	–
NH_4OH-1 M	6.6×10^{-4}	1.5×10^{-2}	120	–
none	30	43	90	133

Table 4.4: Effect of natural aging for various deprotonated PPy-NT. Fit parameters of the model of simple exponential decay and the half-life time.

effective interface in the sample and thus cause the higher polarization. However, to be verified, an appropriate model for the AC response should be find first.

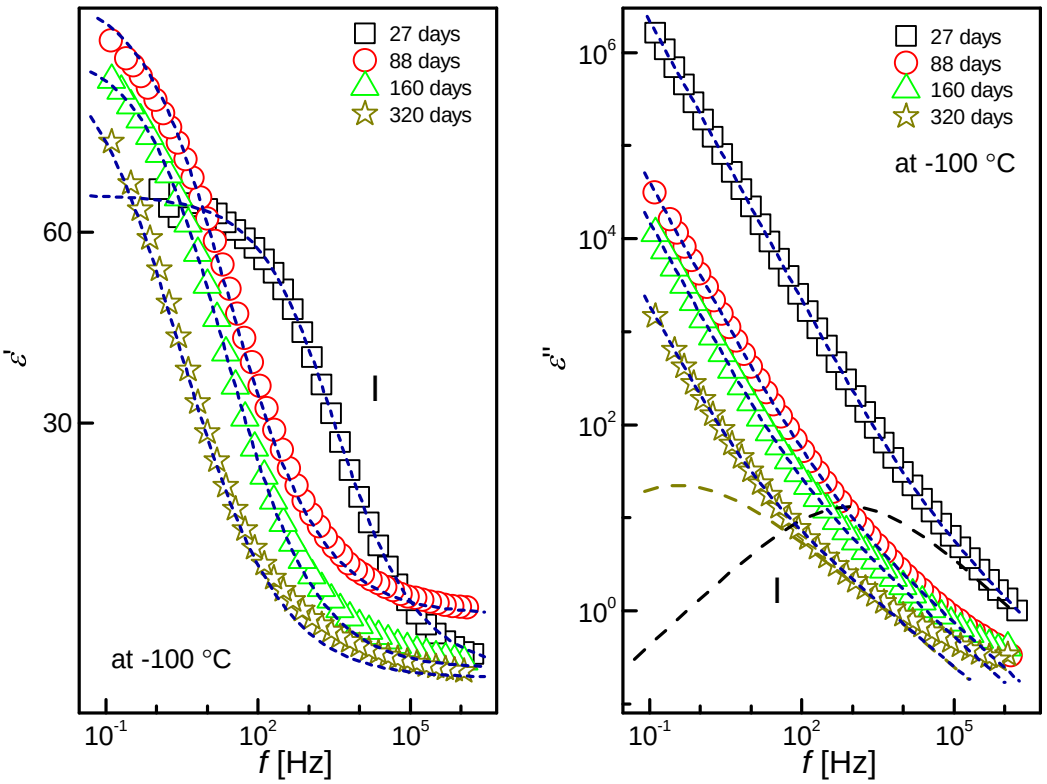

Figure 4.15

Since in previous analysis of charge transport by means of $\sigma(T)$ and $W(T)$ we neglected the age of sample within reasonable confidence interval, it is interesting to investigate aging effect in more details. Several samples were studied at different age and evaluated in the same way as presented in Sec. 3.1, using the Mott-3D-VRH-and-PL model. Since the differences are rather small, for brevity

age [day]	T [°C]	σ_{DC} [S cm^{-1}]	log f_m	$\Delta\epsilon$	ϵ_∞	α	age [day]	T [°C]	σ_{DC} [S cm^{-1}]	log f_m	$\Delta\epsilon$	ϵ_∞	α
27	40	2.56×10^{-4}	6.2	56.3	12	0.51	88	40	1.91×10^{-5}	4.4	129	15	0.48
	20	1.14×10^{-4}	5.9	56.3	12	0.51		20	7.66×10^{-6}	4.1	129	15	0.48
	0	4.69×10^{-5}	5.5	56.3	12	0.51		0	2.67×10^{-6}	3.7	129	15	0.48
	-20	1.81×10^{-5}	5.0	56.3	12	0.51		-20	8.67×10^{-7}	3.1	129	15	0.48
	-40	6.02×10^{-6}	4.4	56.3	12	0.51		-40	2.48×10^{-7}	2.7	129	15	0.48
								-60	6.34×10^{-8}	2.0	129	15	0.48
	-80	5.74×10^{-7}	3.6	56.3	12	0.51		-80	1.38×10^{-8}	1.3	129	15	0.48
	-100	1.22×10^{-7}	2.9	56.3	12	0.51		-100	2.26×10^{-9}	0.6	129	15	0.48
								-110	8.50×10^{-10}	0.2	129	15	0.48
	-120	1.73×10^{-8}	2.1	59.6	12	0.51		-120	2.92×10^{-10}	-0.2	129	15	0.48
								-130	9.11×10^{-11}	-0.7	129	15	0.48
	-140	1.38×10^{-9}	1.1	59.6	12	0.51		-140	2.50×10^{-11}	-1.2	129	15	0.48
								-150	6.66×10^{-12}	-1.8	129	15	0.48
160	40	5.31×10^{-6}	4.1	104	15	0.49	320	40	1.14×10^{-6}	3.2	107	15	0.46
	20	2.11×10^{-6}	3.7	104	15	0.49		20	4.35×10^{-7}	2.9	107	15	0.46
	0	7.85×10^{-7}	3.4	104	15	0.49		0	1.51×10^{-7}	2.5	107	15	0.46
	-20	2.64×10^{-7}	2.9	104	15	0.49		-20	4.69×10^{-8}	2.2	107	14	0.46
	-40	8.20×10^{-8}	2.5	104	12	0.49		-40	1.33×10^{-8}	1.6	107	14	0.46
	-60	2.33×10^{-8}	1.9	104	12	0.49		-60	3.27×10^{-9}	1.1	107	12	0.46
	-80	4.95×10^{-9}	1.2	104	12	0.49		-80	6.78×10^{-10}	0.4	107	12	0.46
	-100	8.48×10^{-10}	0.5	104	12	0.49		-100	1.07×10^{-10}	-0.4	107	12	0.46
	-110	3.18×10^{-10}	0.1	104	12	0.49		-110	3.79×10^{-11}	-0.9	107	12	0.46
	-120	1.07×10^{-10}	-0.3	104	12	0.49		-120	1.17×10^{-11}	-1.3	107	12	0.46
	-130	3.12×10^{-11}	-0.9	104	12	0.49		-130	3.35×10^{-12}	-1.9	107	12	0.46
	-140	7.58×10^{-12}	-1.5	104	12	0.49		-140	7.90×10^{-13}	-2.6	107	12	0.46
	-150	1.29×10^{-12}	-2.2	104	12	0.49		-150	1.11×10^{-13}	-3.2	107	12	0.46

Table 4.5: Fit results of $\epsilon^*(f, T)$ according to the CC model with σ_{DC} contribution for PPy-NT deprotonated with 1 M NaOH at various age.

we plotted only selected samples in the LT region at Fig. 4.17. Fit results are summarized in Table 4.6.

age [months]	σ_{RT} [S cm^{-1}]	σ_0 [S cm^{-1}]	T_0 [K]	a [S cm^{-1} K$^{-\gamma}$]	γ
1.5	63	6400	3.4×10^4	1.7	0.74
1.9	54	6500	4.6×10^4	0.8	0.80
2.4	51	7500	5.2×10^4	0.7	0.80
4.6	44	7000	6.7×10^4	0.6	0.82
6.4	35	7600	9.6×10^4	0.4	0.86
6.9	27	8700	1.4×10^5	0.2	0.90

Table 4.6: Effect of natural aging on room temperature conductivity and fit parameters of the model Mott-3D-VRH-and-PL for PPy-NT. The youngest sample is taken from Ref. [131].

Interestingly, we could construct a plot of fitted parameters against σ_{RT}, as depicted at Fig. 4.18. Such plot eliminated uncertainty in the aging decay function of $\sigma(t)$. Obtained parameters were fitted with phenomenological functions

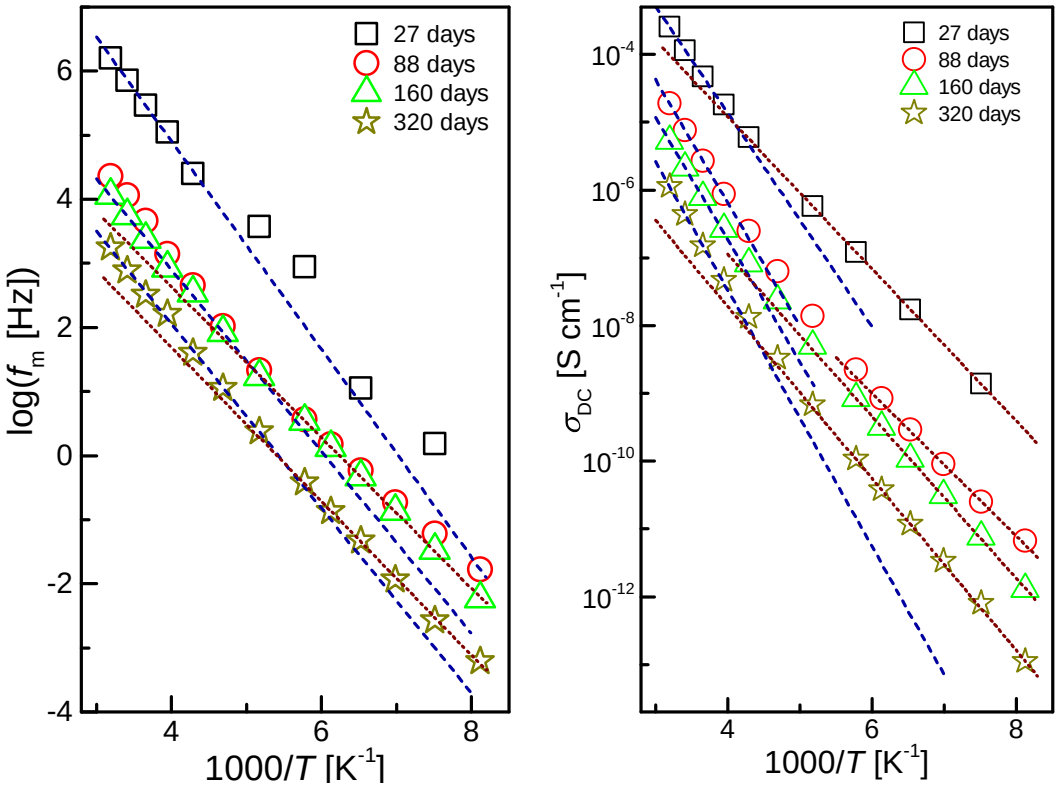

Figure 4.16

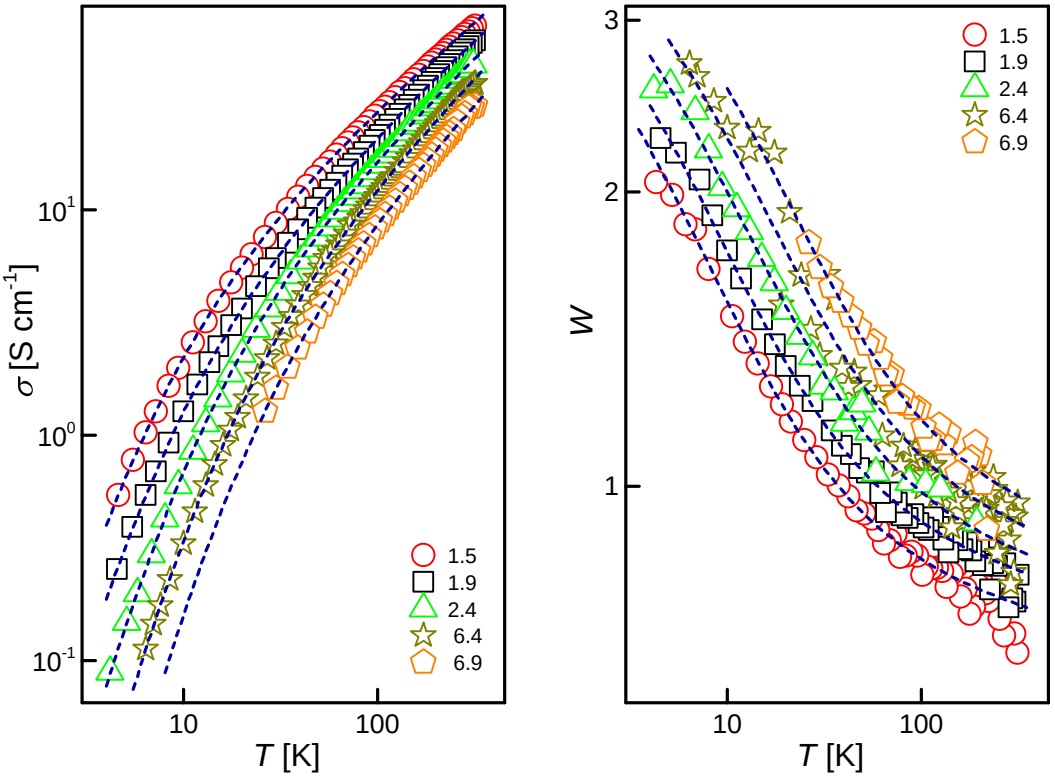

Figure 4.17: Experimental data $\sigma(T)$ (left) and $W(T)$ (right) for PPy-NT at different age.

$\sigma_0^{\mathrm{Mott}} = 8100 - 0.5\exp\left(-\frac{2500}{\sigma_{\mathrm{RT}}+185}\right)$ and $T_0^{\mathrm{Mott}} = 5.2\times10^5\exp\left(-\frac{\sigma_{\mathrm{RT}}}{21}\right)$ for the Mott 3D VRH model and $a = -0.13 + 0.13\exp\left(\frac{\sigma_{\mathrm{RT}}}{26}\right)$ for the PL model with linear decrease of $\gamma = 1.06 - 0.005\sigma_{\mathrm{RT}}$. It is worth to note that while a in the PL model decreases with aging time (decay of σ_{RT}), the pre-exponential factor σ_o^{Mott} increases. We recall the fact that they contain scaling geometric parameters f which could change during aging. At the same time the exponent γ is approaching unity as the sign of departure from MIT closer to the insulating side. The VRH phase becomes more insulating as well since T_0^{Mott} increases; the reason is either decrease of $g(E_{\mathrm{F}})$ or increase of ξ (or both). In this case magnetoresistance measurements would bring this missing information.

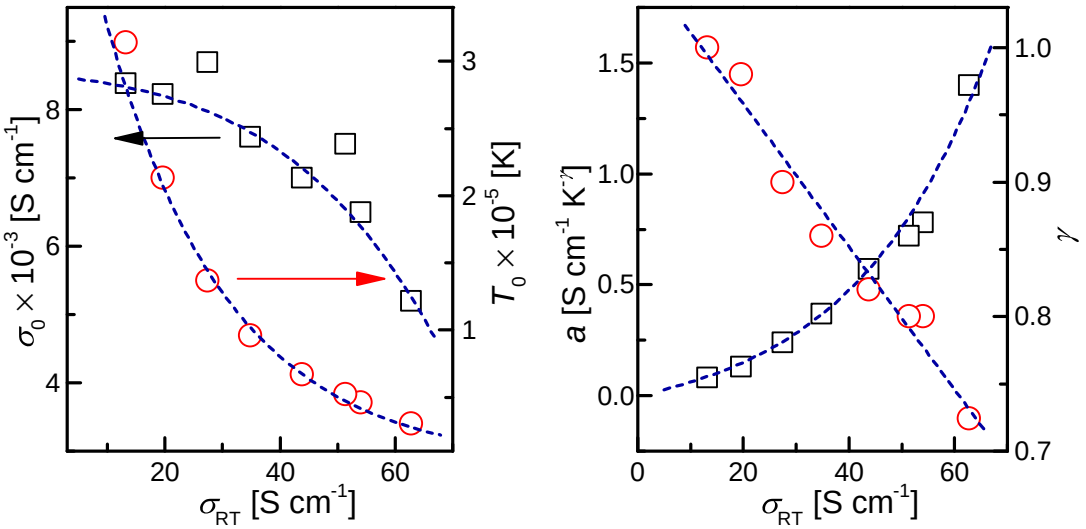

Figure 4.18: Dependence of VRH (left) and PL (right) fit parameters on σ_{RT} for PPy-NT and the transport model Mott-3D-VRH-and-PL.

4.3.2 Accelerated aging at elevated temperatures

Conductivity measurements at short times were conducted in connection to the dilatometric and TG experiments [168]. Two regions are typical: I) heating from RT up to T_{A} followed by 10 hours of isothermal measurement at T_{A} (grey area at Fig. 4.19), II) cooling down to 32 °C,followed by 10 hours of isothermal measurement (white area at Fig. 4.19). Heating and cooling parts reflect only semiconducting nature of samples and will not be discussed more. In longer experiments, for mid-term aging, isothermal measurement at various T_{A} was extended to 10^2 hours.

Obvious difference between PANI-G and PPy-NT is at the isothermal stage. While conductivity of the first decreases, the conductivity of the second surprisingly increases. The loss of conductivity in PANI is believed to be directly linked to water escape as follows from TG experiments [174] and was discussed in Sec. 4.1. The reason for the rise of conductivity remains unknown. The water accounts for only slight increase (Sec. 4.1). The increase is more pronounced with temperature and conductivity. In more conducting samples residual impurities

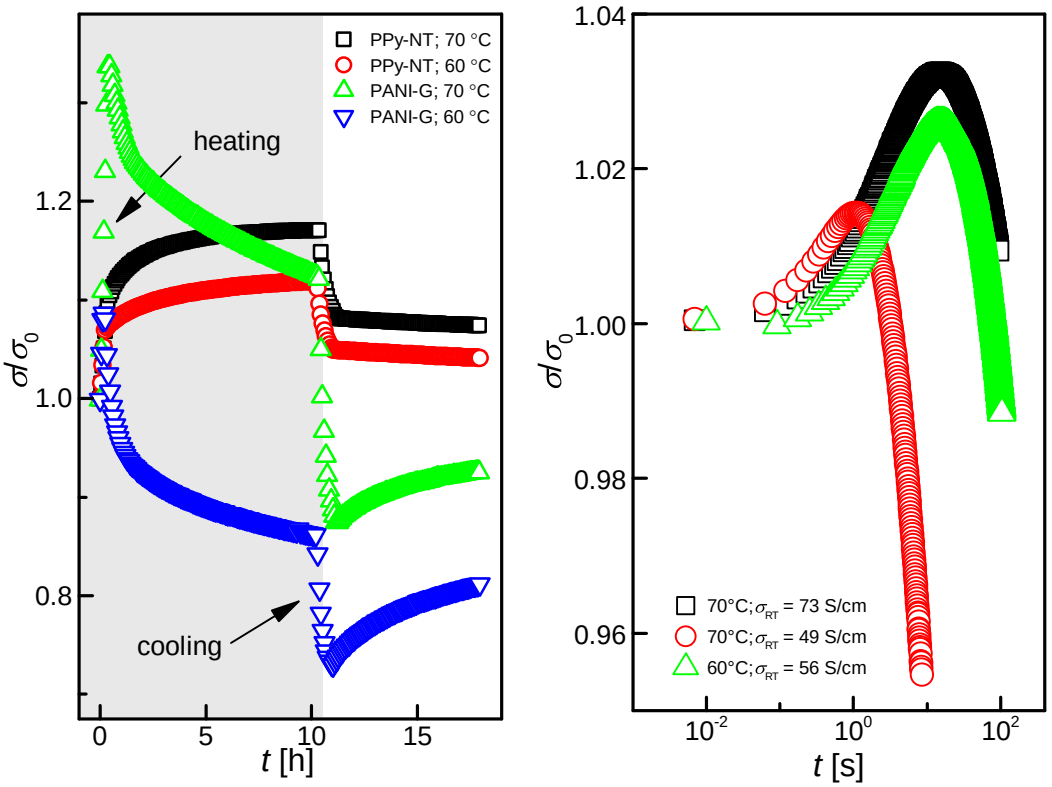

Figure 4.19: Short-term thermal aging of PPy-NT and PANI-G at moderate temperatures (left) and mid-term aging for PPy-NT (right).

including methyl orange were not removed. Thus, it is not know which process can takes place during this thermal 'curing'. After cooling down, partial recovery of PANI conductivity is due to partial reabsorption of water [174] and opposite for PPy-NT [168]. In the extended (mid-term) measurement the aging term causes the non-monotonic dependence. The curing part takes place probably only several hours.

For high $T_A > 100\,°C$ the stretched-exponential function, Eq. (1.55), with changed exponent was found suitable to fit the data of accelerated aging with slightly increasing exponent with T_A (Table. 4.7). In order to compare the characteristic decay time for various temperatures, we fixed the exponent to 0.6. This is in contrast to observed 0.5 [87] but still feasible in the generalized CELT model [61]. For $T_A > 130\,°C$ discrepancy of fit at the short-time region was observed. In general, longer measurements for these T_A were not available due to technical problems of mechanical nature in experiments. The wider experimental window is important to obtain a more confident fit. On the other hand, at $T_A < 120\,°C$, the long-time behavior, from ca. 250 h, can be reproduced by the simple exponential decay. Probably, the limiting underlying aging process changes. Results of analysis concerning fits and the half-life time, $t_{0.5}$ (a horizontal line in the normalized plot), are summarized in Table 4.7. Both, the half-life time and the decay time in stretched exponential function follow the Arrhenius law (Fig. 4.20) with activation energy 0.66 eV and 0.9 eV, respectively. From the activation energy we estimated $t_{0.5}$(RT) =205 days which is higher than 112 days obtained from natural aging. It seems than accelerated aging can not be used for natural ag-

ing estimates, probably due to different aging conditions related to humidity and sunlight which are not taken into account. In real world applications situation can get even more complicated, for instance with season cycles.

T_A [°C]	$t_{0.5}$ [h]	range [h]	A	τ [h]	n
100	27	0–170	1	48	0.63
		0–500	1.03	45	0.6
		>250	0.26	171	1
110	15	0–69	1	26	0.66
		2–280	1.10	21	0.6
		>280	0.1	120	1
120	9.6	0–69	1	16	0.71
		9–240	1.3	10.6	0.6
		>260	0.05	73	1
130	7.5	0–55	1	12	0.78
		16–130	1.41	6	0.6
140	3.6	0–20	1	5.6	0.76
		3–20	1.56	3.1	0.6

Table 4.7: Fit parameters of the conductivity decay with time at various T_A for PPy-NT.

The effect of accelerated aging on $\sigma(T)$ of sample is demonstrated as the steeper decrease of conductivity (Fig. 4.21). The data were analyzed within models Mott-3D-VRH-and-PL and CELT-or-ARH. In comparison with natural aging, the induced disorder is much higher and for long-term-aged samples the transition to the GM regime occurred. The shortly-aged sample at 140 °C is near this transition as the PL exponent is higher than 1 and T_0^{Mott} increased one order of magnitude (Table 4.7). It seems that thermal degradation provides a way how to investigate transition region in more details by variation of T_A and t_A. In contrary to Ref. [86] we were not able to construct single function $\sigma(t, T)$ due to different exponents. Apparently, both $\sigma(T)$ and $\sigma(t)$ are more complicated to be expressed by a single stretched exponential function.

sample	model	σ_0 [S cm^{-1}]	T_0 [K]	n	a [S cm^{-1} K$^{-\gamma}$]	γ	σ_0 [S cm^{-1}]	T_0 [K]	n
non-aged	VRH-and-PL	1700	38400	0.25	1.4	0.9			
30 h at 140 °C	VRH-and-PL	4.5×10^5	1.3×10^6	0.25	1.5×10^{-3}	1.4			
511 h at 100 °C	CELT-or-ARH	100	9200	0.5			0.15	300	1
492 h at 110 °C	CELT-or-ARH	65	17400	0.5			0.01	460	1

Table 4.8: Results of fitting of $\sigma(T)$ and $W(T)$ for thermally aged PPy-NT according the models VRH-and-PL or CELT-or-ARH.

Since conductivity significantly decreases during thermal treatment, impedance spectroscopy could be used to investigate aged samples as well. As an example

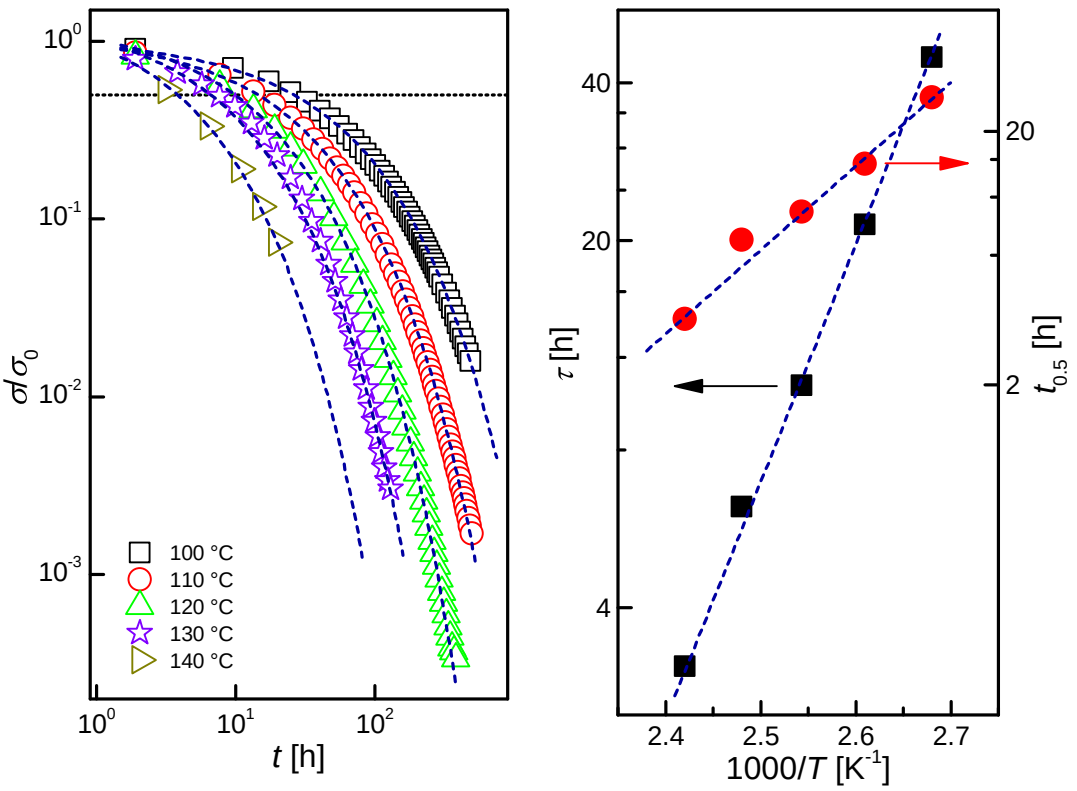

Figure 4.20: Accelerated aging of conductivity (left) of PPy-NT at high temperatures, 100 °C–140 °C, and the Arrhenius plot of the characteristic decay time (for $n = 0.6$) and the half-life time (right).

complex permittivity at −80 °C for aged PPy-NT at 125 °C for 270 hours is plotted at Fig. 4.22. Initially very conducting PPy-NT salt exhibits after aging behavior similar to less deprotonated bases. High permittivity is probably due to interfacial polarization on conducting grains. Obviously, effect of aging carries the same features as deprotonation. Detailed analysis which would require broader temperature range and systematic selection of aged samples is left for a further study, nevertheless AC measurements seem to be a promising tool.

4.3.3 Summary VI

In this section we investigated the stability of conductivity, particularly of PPy-NT in alkaline media, and during aging, both, natural and accelerated at elevated temperatures. The following concluding remarks can be listed:

- PPy-NT was found stable against deprotonation in alkaline media, it decreased only to 10^{-4} S cm^{-1} in alkaline as strong as 10 M NaOH. This implies they potential applicability in such aggressive media.

- The speed of decay at natural aging depends the on value of conductivity, PPy-NT bases degrades faster, for PPy-NT salt it half-life time was estimated to approximately 133 days.

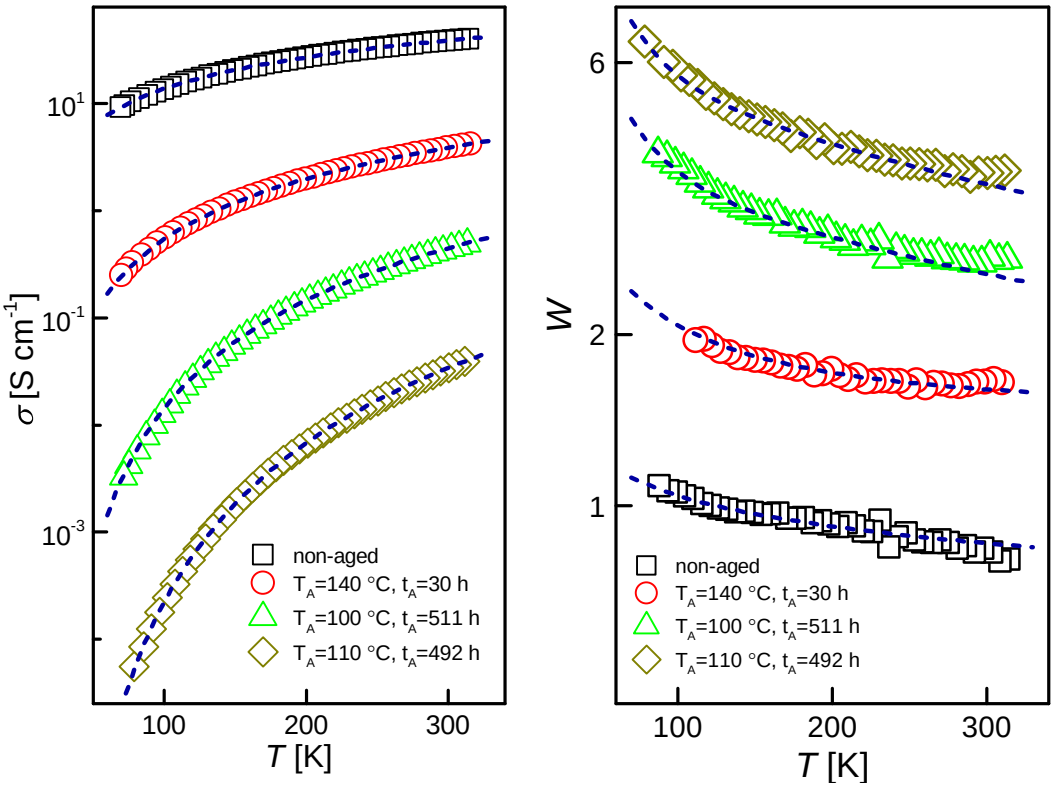

Figure 4.21: Experimental results $\sigma(T)$ (left) and $W(T)$ (right) with corresponding fits (see text) for thermally aged PPy-NT.

- Aging at mild temperatures (below 70 °C) revealed initial increase of conductivity of PPy-NT in contrast to PANI-G. The conductivity decrease in PANI is believed to be caused by fast drying. After several hours even in PPy-NT conductivity decay was found but rather due to thermal aging.

- Aging at high temperatures (above 100 °C) was characterized by the stretched exponential decay with exponent 0.6. Both, the characteristic decay time and the conductivity half life time were found to follow Arrhenius law. Application of such model however could not be transmitted to room temperature aging which is faster, probably due to additional different factors such as higher humidity and sunlight.

- The transport mechanism in aged samples was studied in the framework of the VRH-and-PL model and the CELT-or-ARH model. For samples aged for a long time (about 500 h) the transition from the former to the latter model was found. After all, accelerated aging seems to be a promising tool for such transition studies.

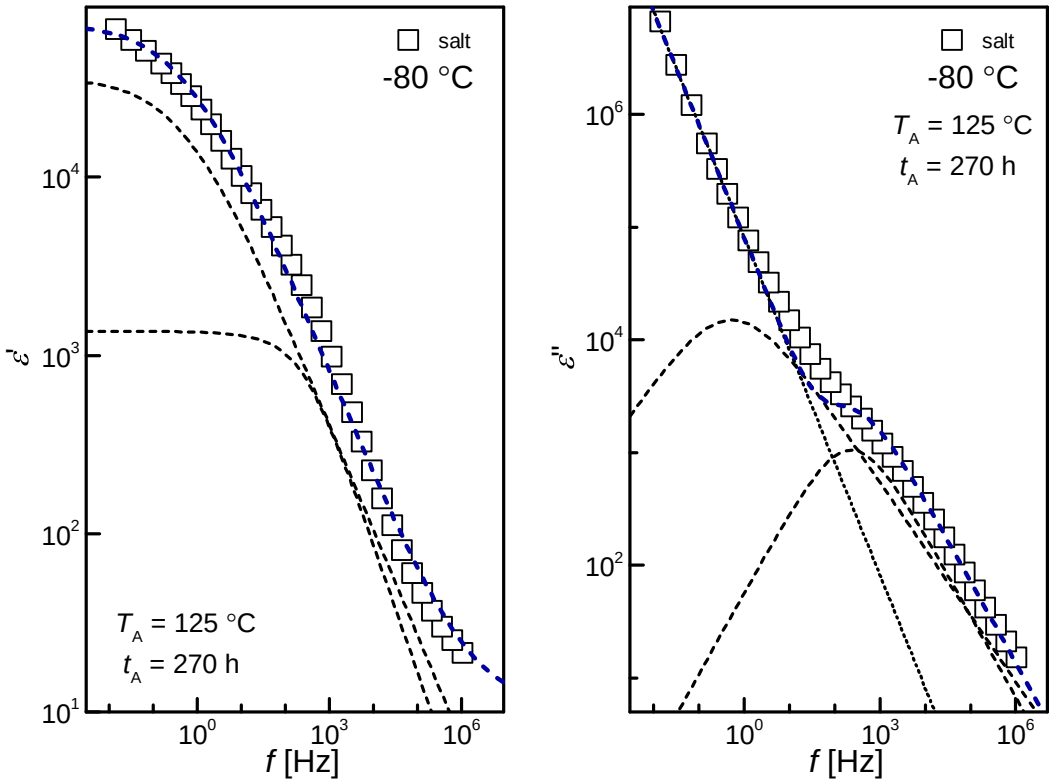

Figure 4.22: Real (left) and imaginary (right) part of complex permittivity for PPy-NT aged at 125 °C.

4.4 Application example: PANI as a gas sensor

One of promising low cost application of conducting polymers is gas sensing, but issues of long-term stability, low selectivity and irreversibility have to be overcome [116]. In the following we present the response of PANI thin films on NH_3, commonly used malicious gas, *e.g.* [117]. PANI was doped (reprotonated) with various sulphonic acids which are believed to enhance stability [93]. The charge transport properties were discussed in Sec. 3.1 and response to drying in Sec. 4.1.

4.4.1 Preliminary testing and search for experimental protocol

Prior to the 'standardized' measurements for sensor testing and investigation of dopant effects on sensor response, various preliminary measurements were performed to gain general insight. Several configurations were tried by means of number and position of electrodes in respect to the PANI layer. The results for bottom/top and two/four electrode configurations are summarized in Fig. 4.23. Tests were performed at NH_3 concentration 500 ppm.

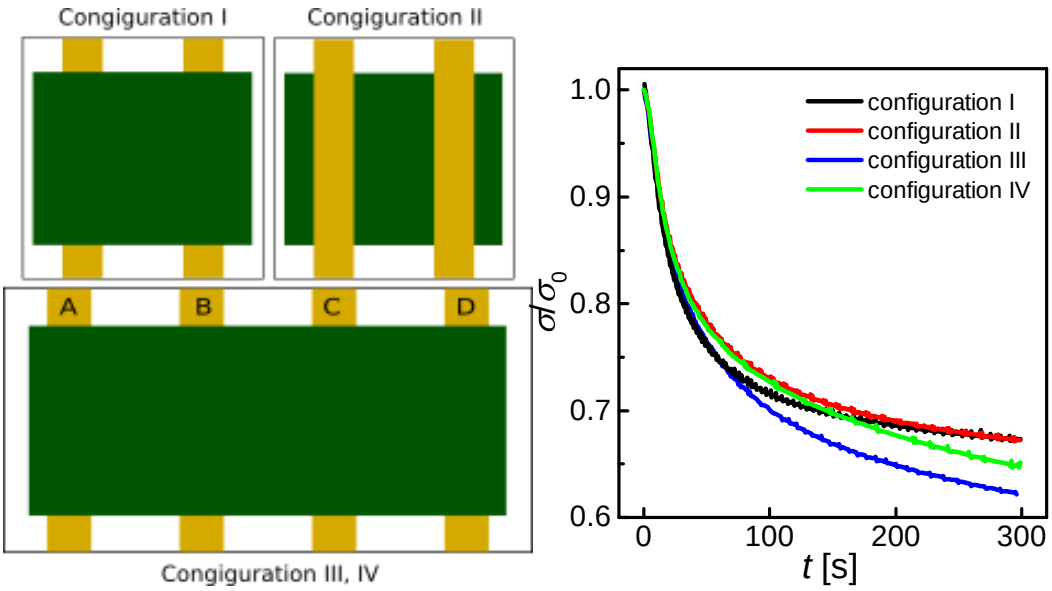

Figure 4.23: Various experimental configurations (left) and the response to 500 ppm concentration of NH_3 (right).

Initial assumption that sputtering of gold electrodes on already prepared polymer film would affect its top layer and the overall conductivity or the response to gas would decrease was not confirmed. The sputtered electrodes (configuration I) were generally very thin, in order of tens of nm. The response is almost identical to the configuration II with two electrodes below the PANI film. The next test was performed for configuration III, the two probe measurement between position A and D at the bottom side. Moreover, only small difference between the two probe or the four probe measurement (configuration IV) was found. In the four probe method, current was applied through electrodes A and D and the voltage drop was measured at positions D and D. All observed differences were considered small to be considered in the next discussion taking into account that majority of results were obtained at configuration I or II.

Three more observations deserve attention before discussion on the response of various PANI samples. The typical experimental protocol for gas sensing consisted from four stages (Fig.4.24). At the beginning (I), there is a drying stage with sample expossed to dry N_2 flow in order to obtain a stable baseline. We recall the fact that the response to humidity is much higher (order of magnitude) than for NH_3 (Fig. 4.6), it is thus very important to be aware of operating conditions in real world applications. Understanding of the humidity effect on conductivity is thus of vital importance besides of its utility for humidity sensing. Next stage (II) is a general prerequisite of preliminary treatment with high dose of NH_3 to prepare a 'more defined' state. In our case the concentration of 2000 ppm for about 45 min was empirically found to serve the best. The lower concentration led to long gradual deprotonation of film without any saturation, and the higher one destroyed the conductivity instantly. The reason for such treatment has not been clarified yet. Please note, that this response is higher than the regular pulse of 2000 ppm. The initial value of conductivity is generally not recovered after this NH_3 treatment, therefore a new baseline is established. The sensor, in principle,

can be recovered by annealing at elevated temperatures when the exposure time was not too long (more than one hour in a strong ammonia ambient) [117]. The third stage (III) is the repeatability test by means of four pulses sequence with concentration 500 ppm (arbitrarily chosen). And finally, the main measurement itself (IV) is represented by the sequence of NH_3 pulses with various concentration. A typical response (PANI-DBSA) after normalization to initial value is plotted at Fig. 4.24.

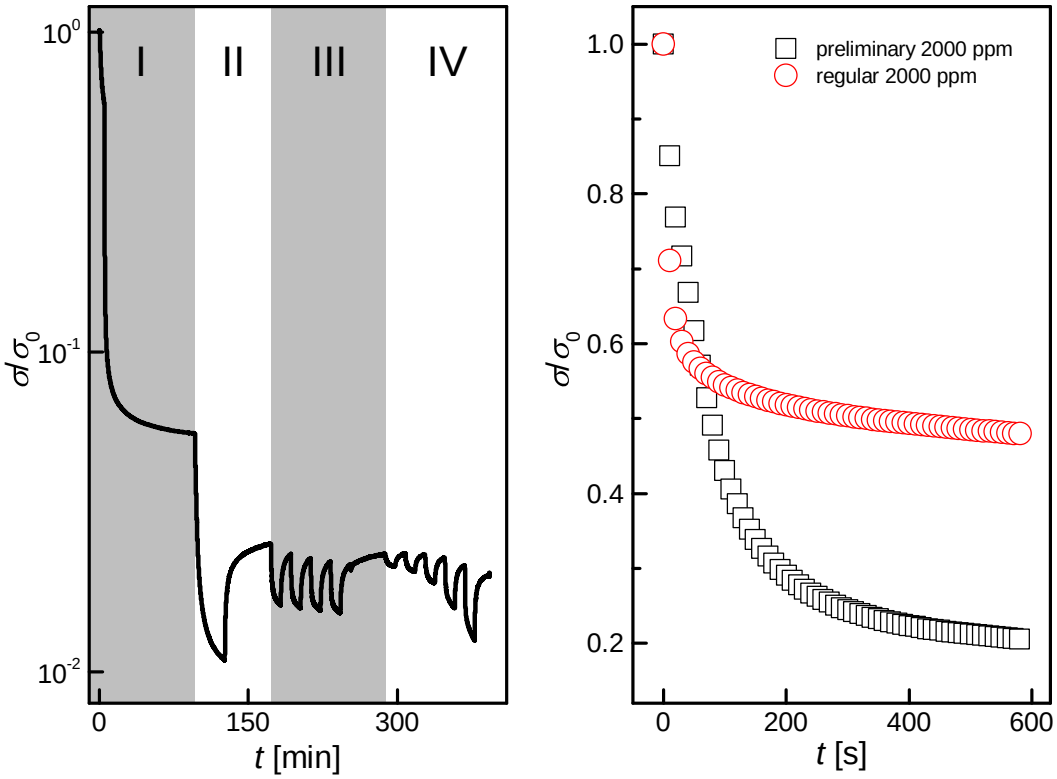

Figure 4.24: Typical sample test (left) and comparison of the preliminary treatment and the regular treatment for 2000 ppm concentration of NH_3 (right).

4.4.2 Effect of dopant on sensor response

In the quantitative analysis we focused on the long-time limit which was fitted (Fig. 4.25) with the simple exponential decay with non-zero asymptotic conductivity:

$$\sigma(t)/\sigma_0 = \sigma_\infty/\sigma_0 + A \exp\left(-\frac{t}{\tau}\right), \tag{4.13}$$

and some pre-exponential factor A', inspired by an empirical formula for the resistance increase [117]. Similarly to the moisture effect, the short times were not covered by this function. Moreover, interpretation of the fit within the diffusion model, Eq. (4.10), resulted in $D \sim 10^{-14}\,\mathrm{cm^2\,s^{-1}}$, which is the same issue as for drying. The exponential decay is very general, for instance, the decrease of number of conducting spots due to deprotonation results in such form []. Up to now, the evaluation is considered as phenomenological, nevertheless, at least the

asymptotic σ_∞ related to the sensors sensitivity could be obtained. The non-zero value of σ_∞ is a sign of some reverse process to deprotonation or equilibrium amount of NH_3 absorbed to sample, otherwise the asymptote should have been zero. The time derivative clearly shows that even a tempting fit of two exponential functions or even the stretched exponential function are not satisfactory. One can imagine 'instant' deprotonation as a parallel to 'instant' evaporation (Sec. 4.1), however more effort is still needed to clarify the short term behavior. On the other hand, existence of minimum in the decay rate (by means of derivative) depending on the gas concentration could be a nice tool in a practical use for the lethal dose estimation within several seconds. This is a great advantage over the use of the long-time asymptotic analysis which requires at least 10 times more time to be successfully employed.

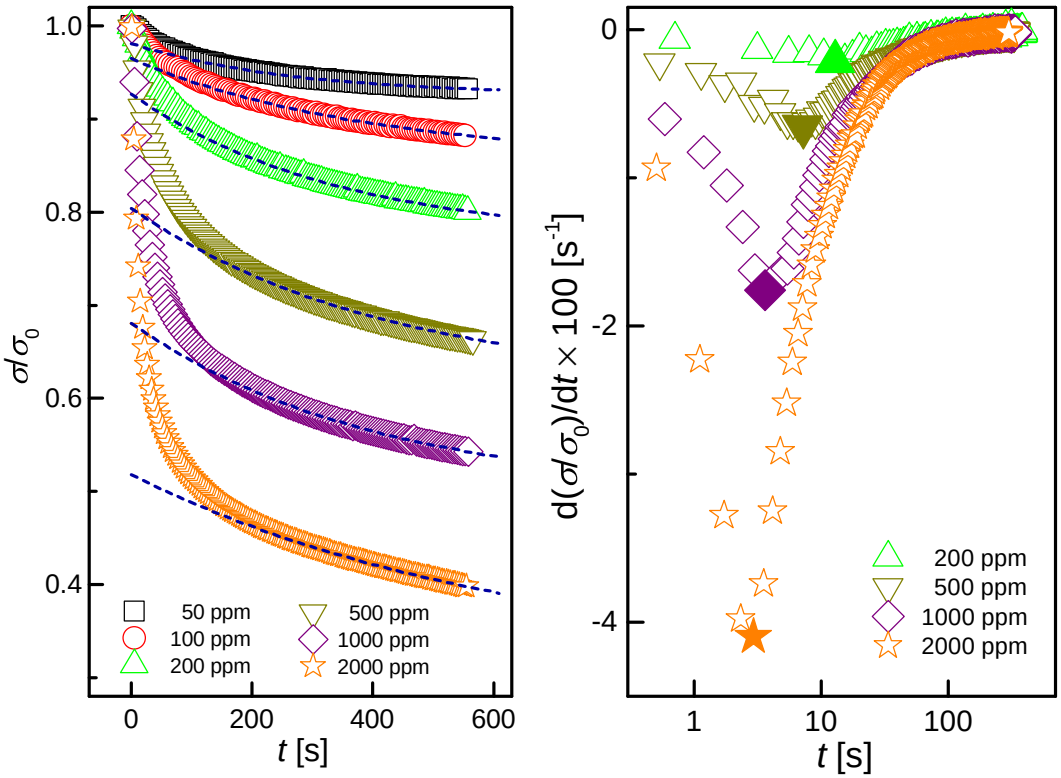

Figure 4.25: Response of PANI-DBSA to c_{NH_3} from 50 to 2000 ppm (left) and its time derivative (right). The data were fitted with a simple exponential decay function.

The response of samples with various sulfonic acids is very similar to standard HCl sample, except MSA which is slightly better. For brevity only four concentration are plotted (Fig. 4.26). For low concentrations (below 200 ppm) data for MSA were not confidential, and high doses (2000 ppm) are missing for some acids. In general, the degradation (deprotonation) of samples doped with sulfonic acids after NH_3 attack is lower. Few subsequent runs could be performed contrary to PANI-HCl which could not be used twice. From a preliminary XPS study it seems that content of sulfonic dopants remains the same and the nitrogen content increases [175,176]. We can speculate about some trapped molecules of NH_3. The detailed long-term stability study should follow. From the long-time limit we estimated the sensitivity and the relaxation time, τ, for assumed phenomenological

process. The results are summarized in Table 4.9 and Fig. 4.27. The sensitivity exhibits the trend for saturation at high concentrations. The response is highest for small dopant molecules like MSA and DBSA while the large polymer dopants PSSA and PAMPSA have the similar response to HCl. Therefore they may be preferentially used only if their long-time stability turns out to be superior. The relaxation time clearly exhibits increasing trend with c_{NH_3}, therefore at higher concentrations longer time is necessary for conductivity saturation. It should be noted that the values of τ are subjected to large uncertainty (10–20 %) regarding the selected width of fitted interval (usually last 200–300 s were used). Longer experiments are necessary for the precision improvement.

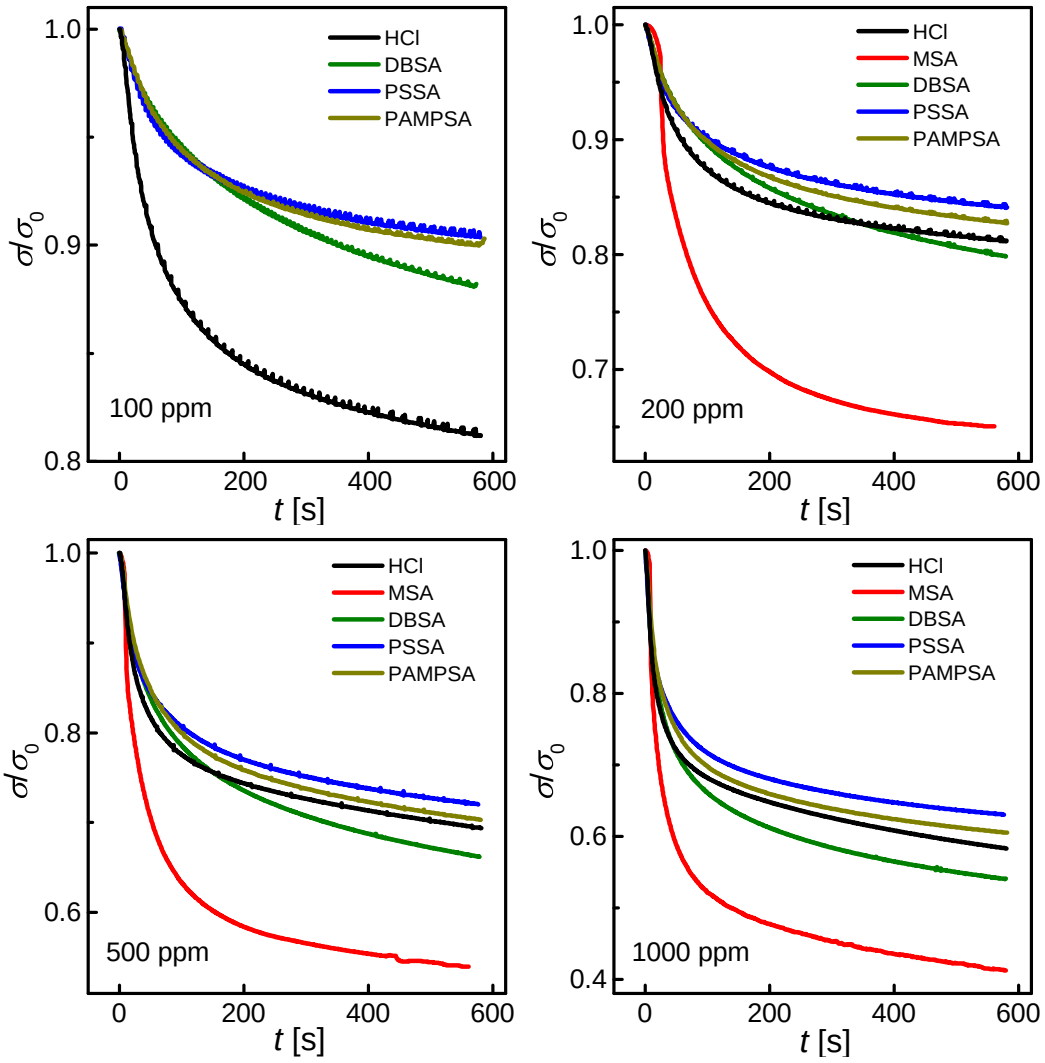

Figure 4.26: Response of PANI doped with various acids to c_{NH_3} from 100 to 1000 ppm.

4.4.3 Summary VII

Without being of prime interest, in this final section we presented the case study for PANI application as malicious gas sensor. Several sulfonic acids were

dopant	c_{NH_3} [ppm]	σ_∞/σ_0	τ [s]	c_{NH_3} [ppm]	σ_∞/σ_0	τ [s]	c_{NH_3} [ppm]	σ_∞/σ_0	τ [s]
HCl	50	0.93	65	100	0.87	160	200	0.76	280
	500	0.66	450	1000	0.56	490	2000		
MSA	50	0.86	140	100	0.79	170	200	0.63	220
	500	0.52	370	1000	0.42	420	2000	0.36	450
DBSA	50	0.93	260	100	0.86	370	200	0.77	340
	500	0.61	420	1000	0.49	440	2000	0.32	560
PSSA	50	0.93	220	100	0.90	230	200	0.83	260
	500	0.70	310	1000	0.61	340	2000		
PAMPSA	50	0.93	180	100	0.89	230	200	0.81	240
	500	0.68	290	1000	0.61	310	2000		

Table 4.9: Fit parameters of conductivity exponential decay with time, Eq. (4.13) for various NH_3 concentration for PANI films doped with various acids.

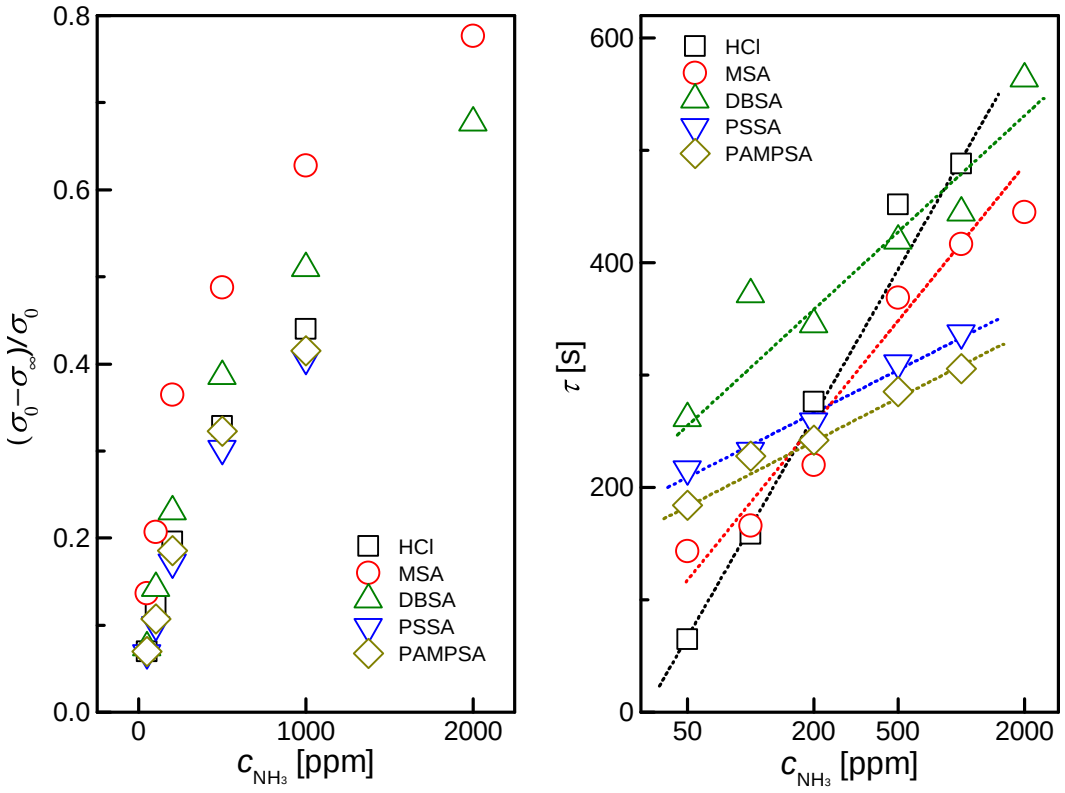

Figure 4.27: Dependence of the sensitivity (left) and the relaxation time (right) on NH_3 concentration for various PANI samples. Lines are guides to eyes only.

selected for PANI reprotonation and compared to 'standard' PANI-HCl. Some important concluding remarks can be listed:

- PANI sensors are about 10 times more sensitive to humidity then to ammonia, therefore knowledge of combined effect is essential for their real world

applications.

- PANI films cannot operate reliably without pretreatment with high dose (2000 ppm) of NH_3.

- Higher sensitivity is achieved with sulfonic acids with small molecules. Sulfonic acids are generally more stable after NH_3 attack than hydrochloric acid.

- The time response cannot be explained within simple diffusion model. The concentration-dependent minimum in the first derivative of the time response could be used as a technical tool for real data processing and evaluation.

Further investigation is needed for a better understanding of underlying physical/chemical processes and a long-term stability study should follow to provide a base prior to any stabilization progress could be achieved by synthesis modification.

Conclusion

In the presented thesis, charge transport in polyaniline and polypyrrole subjected to variety of modifications was studied by means of temperature and frequency dependence of conductivity. Although the data evaluation is not without ambiguity and there can be serious doubts on validity of theoretical models, it provides general insight into the problem. The charge transport follows the inherent heterogeneity of the systems. This heterogeneity was found at different length scales from micro-, through meso- to macroscale. A typical representative of microscale heterogeneity is the disorder and inhomogeneous doping observed in PPy-NT. From that perspective the lowest level of heterogeneity was found for PPy-NT-$FeCl_3$ samples which contained well ordered regions exhibiting homogeneous 3D VRH and regions close to MIT. When this order is disrupted by heterogenous doping and lower protonation, the transport mechanism is better explained within the GM model with the origin coming from (bi)polaronic clusters of various sizes or Q1D VRH model limited by interchain hoping. Heterogeneity at mesoscale is reflected in morphology where the increasing content of the globular phase (at expense of nanotubes) decreased overall conductivity and shifted the system into the GM regime. Finally, silver decoration of polymers with large clusters and agglomerates of µm size introduced heterogeneity at the macroscopic level. When the volume ratio of metallic silver reaches the critical value, charge transport is further driven by silver, limited by scattering at grain boundaries or interfaces. This critical value, observed within 18–27 vol.%, is affected by polymer matrix.

From several oxidants/dopants employed we found $FeCl_3$ the best from conductivity point of view for both PPy (alongside with MO as template) and PANI (alongside with MSA doping) synthesis. However, one should be careful, since the dependence on concentration of dopant and template is non-monotonic. Lowering the polymerization temperature was found to bring only minor (often negligible) improvements. From studied sulfonic acids, MSA is again a good candidate for PANI doping when sensors are of interest.

Good stability of highly conducting ($\approx 10^1\,\mathrm{S\,cm^{-1}}$) PPy-NT prepared with $FeCl_3$ was found in alkaline media where conductivity was maintained at reasonable level about $10^{-4}\,\mathrm{S\,cm^{-1}}$ after treatment with as strong as 10 M NaOH solution. However, deprotonated PPy-NT has exhibited faster aging than as-prepared samples where the half-life time was found higher than 4 months comparing to few days for deprotonated samples. Even after two years, the conductivity of PPy-NT was higher than the majority of other studied fresh samples. Accelerated aging at elevated temperatures higher than 100 °C had similar impact on conductivity as deprotonation in alkaline media. The characteristic decay time and the half-life time followed the Arrhenius law. However, its use at room temperature provided higher values than observed for natural aging. Hence, natural degradation is faster, probably due to synergistic effect of various factors such as light and humidity which were not present during accelerated tests.

Effect of drying on conductivity was studied, and it was found that it did not affect PPy-NT in contrary to all samples of granular morphology. When conductivity decreased with water removal, a phenomenological linear coupling between local conductivity and local water concentration was suggested and used in the diffusion-based model. Subsequently, it was applied on experimental data in the long-time limit. For pellets, good agreement was found and the diffusion constant was estimated to order $10^{-7}\,\mathrm{cm}^2\,\mathrm{s}^{-1}$ for both PANI and PPy regardless of variations in their synthesis. In case of thin films, the model gave $D \approx 10^{-7}\,\mathrm{cm}\,\mathrm{s}^{-2}$ and thus considered as inadequate. Generally, for thin films, the drop of conductivity was order of magnitude higher than for pellets.

To conclude, even though insight into charge transport in CP has been developed during the decades, it is still puzzling and its proper determination is challenging, particularly regarding a number of possible variations in synthesis and post-treatment. On the other hand, we believe we have provided both, a valuable feedback to technologists for further synthesis modifications, and inspiration for theoreticians for new models (approaches) development. The field is thus still open for extensive research. To name at least some directions:

- understanding of the non-monotonic dependence of conductivity on molar concentration of dopants, templates, *etc.* to maximize of conductivity,

- preparing more ordered PPy nanotubes which would cross the boundary of MIT, for instance by lowering polymerization temperature or using other dopants such as MSA,

- study of transition from the homogeneous 3D VRH regime to the heterogeneous CELT (or Q1D VRH) regime in PPy-NT by means of defined gradual thermal aging,

- development of microscopic models for aging, AC response and drying, clarification of conductivity-structure-moisture relationship,

- understanding of chemical and physical processes which determine the short-term response in sensors for their successful use in fast-responding applications.

Bibliography

[1] Heeger, A. J. Nobel lecture: Semiconducting and metallic polymers: The fourth generation of polymeric materials. *Review of Modern Physics 73* (2001), 681–700.

[2] MacDiarmid, A. G. Nobel Lecture: 'Synthetic metals': A novel role for organic polymers. *Reviews of Modern Physics 73*, 3 (2001), 701–712.

[3] Štoll, I., and Sedlák, B. *Elektřina a magnetismus*. Academia, Praha, 1993. ISBN 80–200–0172–7.

[4] Schönhals, A., and Kremer, F. Theory of dielectric relaxation. In *Broadband Dielectric Spectroscopy*, F. Kremer and A. Schönhals, Eds. Springer, 2003, ch. 1. ISBN 3–540–43407–0.

[5] Zimmerman, W., and Hewakandamby, B. Analyzing evolution equations by the finite element method. In *Multiphysics Modelling with Finite Element Methods*, W. Zimmerman, Ed. World Scientific, 2006, ch. 3. ISBN 9789812568434.

[6] Hamann, C., Burghardt, H., and Frauenheim, T. *Electrical Conduction Mechanisms in Solids*. Physikalische Monographien. Deutscher Verlag der Wissenschaften, 1988. ISBN 3–326–00380–3.

[7] Heeger, A. J., Kivelson, S., Schrieffer, J., and Su, W.-P. Solitons in conducting polymers. *Reviews of Modern Physics 60*, 3 (1988), 781–850.

[8] Botelho, A. L., Shin, Y. W., Li, M. H., Jiang, L. L., and Lin, X. Unified Hamiltonian for conducting polymers. *Journal of Physics: Condensed Matter 23*, 45 (2011), 455501.

[9] Bredas, J., Themans, B., Fripiat, J., Andre, J., and Chance, R. Highly conducting polyparaphenylene, polypyrrole, and polythiophene chains: An ab initio study of the geometry and electronic-structure modifications upon doping. *Physical Review B 29*, 12 (1984), 6761–6773.

[10] Hutchison, G. R., Zhao, Y.-J., Delley, B., Freeman, A. J., Ratner, M. A., and Marks, T. J. Electronic structure of conducting polymers: Limitations of oligomer extrapolation approximations and effects of heteroatoms. *Physical Review B 68* (2003), 035204.

[11] MacDiarmid, A. G., Chiang, J. C., Richter, A. F., and Epstein, A. J. Polyaniline: a new concept in conducting polymers. *Synthetic Metals 18*, 1–3 (1987), 285–290.

[12] Stejskal, J., Trchová, M., Bober, P., Humpolíček, P., Kašpárková, V., Sapurina, I., Shishov, M. A., and Varga, M. *Conducting Polymers: Polyaniline*. John Wiley and Sons, Inc., 2002, pp. 1–50. ISBN 978-0–471–44026–0.

[13] Cao, Y., Treacy, G. M., Smith, P., and Heeger, A. J. Solution-cast films of polyaniline: Optical-quality transparent electrodes. *Applied Physics Letters 60*, 22 (1992), 2711.

[14] Reghu, M., Vakiparta, K., Yoon, C., Cao, Y., Moses, D., and Heeger, A. Tuning through the critical regime of the metal-insulator transition in conducting polymers by pressure and magnetic field. *Synthetic Metals 65*, 2-3 (1994), 167–171.

[15] Ahlskog, M., Menon, R., Heeger, A. J., Noguchi, T., and Ohnishi, T. Metal-insulator transition in oriented poly(p-phenylenevinylene). *Physical Review B 55*, 11 (1997), 6777–6787.

[16] Sapurina, I., and Stejskal, J. The mechanism of the oxidative polymerization of aniline and the formation of supramolecular polyaniline structures. *Polymer International 57*, 12 (2008), 1295–1325.

[17] Long, Y.-Z., Li, M.-M., Gu, C., Wan, M., Duvail, J.-L., Liu, Z., and Fan, Z. Recent advances in synthesis, physical properties and applications of conducting polymer nanotubes and nanofibers. *Progress in Polymer Science 36*, 10 (2011), 1415–1442.

[18] Penner, R. M., and Martin, C. R. Electronically conductive composite polymer membranes. *Journal of Electrochemical Society 133* (1986), 310–315.

[19] Cai, Z., Lei, J., Liang, W., Menon, V., and Martin, C. R. Molecular and supramolecular origins of enhanced electronic conductivity in template-synthesized polyheterocyclic fibrils. 1. Supramolecular effects. *Chemistry of Materials 3*, 5 (1991), 960–967.

[20] Saha, S. K., Su, Y. K., Lin, C. L., and Jaw, D. W. Current-voltage characteristics of conducting polypyrrole nanotubes using atomic force microscopy. *Nanotechnology 15*, 1 (2004), 66–69.

[21] Konyushenko, E. N., Stejskal, J., Šeděnková, I., Trchová, M., Sapurina, I., Cieslar, M., and Prokeš, J. Polyaniline nanotubes: conditions of formation. *Polymer International 55*, 1 (2006), 31–39.

[22] Travers, J. P., Sixou, B., Berner, D., Wolter, A., Rannou, P., Beau, B., Pepin-Donat, B., Barthet, C., Guglielmi, M., Mermilliod, N., Gilles, B., Djurado, D., Attias, A. J., and Vautrin, M. Is granularity the determining feature for electron transport in conducting

polymers? *Synthetic Metals 101* (1999), 359–362.

[23] Kaiser, A. B. Electronic transport properties of conducting polymers and carbon nanotubes. *Reports on Progress in Physics 64*, 1 (2001), 1–49.

[24] Pietronero, L. Ideal conductivity of carbon pi polymers and intercalation compounds. *Synthetic Metals 8* (1983), 225–231.

[25] Kivelson, S., and Heeger, A. J. Intrinsic conductivity of conducting polymers. *Synthetic Metals 22* (1988), 371–384.

[26] Naarmann, H., and Theophilou, N. New process for the production of metal-like, stable polyacetylene. *Synthetic Metals 22*, 1 (1987), 1–8.

[27] Larkin, A. I., and Khmelnitskii, D. E. Activation conductivity in disordered systems with large localization length. *Soviet Physics, JETP 56*, 3 (1982), 647–652.

[28] Reghu, M., Yoon, C. O., Moses, D., Heeger, A. J., and Cao, Y. Transport in polyaniline near the critical regime of the metal-insulator transition. *Physical Review B 48*, 24 (1993), 17685–17694.

[29] Ahlskog, M., Reghu, M., and Heeger, A. J. The temperature dependence of the conductivity in the critical regime of the metal - insulator transition in conducting polymers. *Journal of Physics: Condensed Matter 9* (1997), 4145–4156.

[30] Martens, H. C. F., Brom, H. B., and Menon, R. Metal-insulator transition in PF6 doped polypyrrole: Failure of disorder-only models. *Physical Review B 64*, 20 (2001), 201102.

[31] Martens, H. Delocalization in weakly coupled disordered wires: Application to conjugated polymers. *Physical Review Letters 96*, 7 (2006), 076603.

[32] Anderson, P. W. Local moments and localized states. *Rev. Mod. Phys. 50* (1978), 191–201.

[33] Tessler, N., Preezant, Y., Rappaport, N., and Roichman, Y. Charge transport in disordered organic materials and its relevance to thin-film devices: A tutorial review. *Advanced Materials 21*, 27 (2009), 2741–2761.

[34] Mott, N. F. Conduction in glasses containing transition metal ions. *Journal of Non-Crystalline Solids 1* (1968), 1–17.

[35] Miller, A., and Abrahams, E. Impurity conduction at low concentrations. *Physical Review B 120*, 3 (1960), 745–755.

[36] Mott, N. F., and Davis, E. A. *Electronic Processes in Non-crystalline Materials*. Clarendon Press, Oxford, 1979. ISBN 978–0–19–964533–6.

[37] Castner, T. G. Hopping conduction in the critical regime approaching the metal-insulator transition. In *Hopping Transport in Solids*, M. Pollak and B. I. Shklovskii, Eds. North Holland, Amsterdam, 1991. ISBN 978–0–444–88037–6.

[38] Wang, Z. H., Ray, A., MacDiarmid, A. G., and Epstein, A. J. Electron localization and charge transport in poly(o-toluidine): A model polyaniline derivative. *Physical Review B1 43*, 5 (1991), 4373–4384.

[39] Prigodin, V. N., Samukhin, A. N., and Epstein, A. J. Variable range hopping in low-dimensional polymer structures. *Synthetic Metals 141*, 1-2 (2004), 155–164.

[40] Efros, A. L., and Shklovskii, B. I. Coulomb gap and low temperature conductivity of disordered systems. *Journal of Physics C: Solid State Physics 8* (1975), L49–L51.

[41] Nakhmedov, E. P., Prigodin, V. N., and Samukhin, A. N. No Title. *Soviet Physics Solid State 31* (1989), 368–375.

[42] Wang, Z. H., Scherr, E. M., MacDiarmid, A. G., and Epstein, A. J. Transport and EPR studies of polyaniline: A quasi-one-dimensional conductor with three-dimensional "metallic" states. *Physical Review B 45*, 8 (1992), 4190–4202.

[43] Rosenbaum, R., Nguyen, L. V., Graham, M. R., and Witcomb, M. A useful Mott-Efros-Shklovskii resistivity crossover formulation for three-dimensional films. *Journal of Physics: Condensed Matter 9* (1997), 6247–6256.

[44] Baughman, R., and Shacklette, L. Conductivity as a function of conjugation length: Theory and experiment for conducting polymer complexes. *Physical Review B 39*, 9 (1989), 5872–5886.

[45] Fogler, M., Teber, S., and Shklovskii, B. Variable-range hopping in quasi-one-dimensional electron crystals. *Physical Review B 69*, 3 (2004), 035413.

[46] Deutscher, G., Levy, Y., and Souillard, B. T 3/7 hopping conductivity in a class of disordered systems. *Europhysics Letters 4*, 5 (1987), 577–582.

[47] Aharony, A., Zhang, Y., and Sarachik, M. Universal crossover in variable range hopping with Coulomb interactions. *Physical Review Letters 68*, 26 (1992), 3900–3903.

[48] Meir, Y. Universal crossover between Efros-Shklovskii and Mott variable-range-hopping regimes. *Physical Review Letters 77*, 26 (1996), 5265–5267.

[49] Zabrodskii, A. G., and Zinovjeva, K. N. Low-temperature conductivity and metal-insulator transition in compensate n-Ge. *Soviet Physics, JETP 59*, 2 (1984), 425–433.

[50] Dvurechenskii, A. V., Dravin, V. A., and Yakimov, A. I. Activationless hopping conductivity along the states of the Coulomb gap in a-Si⟨Mn⟩. *JETP Letters 48*, 3 (1988), 155–159.

[51] Shklovskii, B. I., and Efros, A. L. *Electronic Properties of Doped Semiconductors*. Springer, Berlin, 1985. ISBN 978–3–662–02405–8.

[52] Raikh, M., Czingon, J., Ye, Q., Koch, F., Schoepe, W., and Ploog, K. Mechanisms of magnetoresistance in variable-range-hopping transport for two-dimensional electron systems. *Physical Review B 45*, 11 (1992), 6015–6022.

[53] Nguyen, L. V., Spivak, B. Z., and Shklovskii, B. I. Aaronov-Bohm oscillations with normal and superconducting flux quanta in hopping conductivity. *JETP Letters 41*, 1 (1985), 42–45.

[54] Sivan, U., Entin-Wohlman, O., and Imry, Y. Orbital magnetoconductance in the variable-range-hopping regime. *Physical Review Letters 60*, 15 (1988), 1566–1569.

[55] Rosenbaum, R., Milner, A., Haberkern, R., Häussler, P., Palm, E., Murphy, T., Hannahs, S., and Brandt, B. Magnetoresistance of an insulating quasicrystalline AlPdRe film in large magnetic fields. *Journal of Physics: Condensed Matter 13*, 13 (2001), 3169–3185.

[56] Dyre, J. C. The random free-energy barrier model for ac condcution in disordered solids. *Journal of Applied Physics 64*, 5 (1988), 2456–2468.

[57] Sheng, P., Abeles, B., and Arie, Y. Hopping conductivity in granular metals. *Physical Review Letters 31*, 1 (1973), 44–47.

[58] Abeles, B., Sheng, P., Coutts, M. D., and Arie, Y. Structural and electrical properties of granular metal films. *Advances in Physics 24* (1975), 407–461.

[59] Sheng, P., and Klafter, J. Hopping conductivity in granular disordered systems. *Physical Review B 27*, 4 (1983), 2583–2586.

[60] Zuppiroli, L., Bussac, M. N., Paschen, S., Chauvet, O., and Forro, L. Hopping in disordered conducting polymers. *Physical Review B 50*, 8 (1994), 5196–5203.

[61] Sixou, B., and Travers, J. P. Simulation of the temperature dependence of the dc conductivity in granular systems with the effective medium theory. *Journal of Physics: Condensed Matter 10*, 3 (1998), 593.

[62] Sheng, P., Sichel, E. K., and Gittleman, J. I. Fluctuation-induced tunneling conduction in carbon-polyvinylchloride composites. *Physical Review Letters 40*, 18 (1978), 1197–1200.

[63] Sheng, P. Fluctuation-induced tunneling conduction in disordered materials. *Physical Review B 21*, 6 (1980), 2180–2195.

[64] Voit, J., and Buttner, H. Fluctuation-induced tunneling and the conduction mechanism in metallic polyacetylene. *Solid State Communications 67*, 12 (1988), 1233–1237.

[65] Paasch, G., Lehmann, G., and Wuckel, L. A novel barrier model for fluctuation-induced tunnelling in highly conductive polyacetylene. *Synthetic Metals 37*, 1-3 (1990), 23–32.

[66] Paschen, S., Bussac, M. N., Zuppiroli, L., Minder, E., and Hilti, B. Tunnel junctions in a polymer composite. *Journal of Applied Physics 78*, 5 (1995), 3230–3237.

[67] Bianchi, R. F., Ferreira, G. F. L., Lepienski, C. M., and Faria, R. M. Alternating electrical conductivity of polyaniline. *Journal of Chemical Physics 110*, 9 (1999), 4602–4607.

[68] Kaiser, A. 'Metallic' polymers: Interpretation of the electronic transport properties. *Synthetic Metals 43*, 1-2 (1991), 3329–3334.

[69] Kaiser, A., Liu, C.-J., Gilberd, P., Chapman, B., Kemp, N., Wessling, B., Partridge, A., Smith, W., and Shapiro, J. Comparison of electronic transport in polyaniline blends, polyaniline and polypyrrole. *Synthetic Metals 84*, 1–3 (1997), 699–702.

[70] Kremer, F., and Rozanski, S. A. The dielectric properties of semiconducting disordered materials. In *Broadband dielectric spectroscopy*, F. Kremer and A. Schönhals, Eds. Springer, 2003, ch. 12. ISBN 3–540–43407–0.

[71] Dyre, J., and Schrøder, T. Universality of ac conduction in disordered solids. *Reviews of Modern Physics 72*, 3 (2000), 873–892.

[72] Asami, K. Characterization of heterogeneous systems by dielectric spectroscopy. *Progress in Polymer Science 27*, 8 (2002), 1617–1659.

[73] Stauffer, D. *Introduction to percolation theory.* Taylor and Francis, London, 1985. ISBN 0–85066–315–6.

[74] McQueen, D. H., Jäger, K.-M., and Pelíšková, M. Multiple threshold percolation in polymer/filler composites. *Journal of Physics D: Applied Physics 37*, 15 (2004), 2160–2169.

[75] Ambegaokar, V., Halperin, B. I., and Langer, J. S. Hopping conductivity in disordered systems. *Physical Review B 4*, 8 (1971), 2612–2620.

[76] Pollak, M. A percolation treatment of dc hopping conduction. *Journal of Non-Crystalline Solids 11*, 1 (1972), 1–24.

[77] Jonscher, A. *Dielectric Relaxation in Solids*. Chelsea Dielectrics Press Limited, 1983. ISBN 978–0–950–87110–3.

[78] MacDonald, J., and Cook, G. Reply to comments by Almond and West on Na β-alumina immittance data analysis. *Journal of Electroanalytical Chemistry and Interfacial Electrochemistry 193*, 1-2 (1985), 57–74.

[79] Havriliak, S., and Negami, S. A complex plane analysis of α-dispersions in some polymer systems. *Journal of Polymer Science Part C: Polymer Symposia 14*, 1 (1966), 99–117.

[80] Schönhals, A., and Kremer, F. Analysis of dielectric spectra. In *Broadband dielectric spectroscopy*, F. Kremer and A. Schönhals, Eds. Springer, 2003, ch. 3. ISBN 3–540–43407–0.

[81] Münstedt, H. Ageing of electrically conducting organic materials. *Polymer 29* (1988), 296–302.

[82] Elsenbaumer, R., Maleysson, C., and Jen, K. Stability of doped conductive polymers. *Polymer Materials: Science and Engineering 56* (1987), 54–55.

[83] Tansley, T. L., and Maddison, D. S. Conductivity degradation in oxygen-aged polypyrrole. *Journal of Applied Physics 69*, 11 (1991), 7711–7713.

[84] Truong, V.-T. Thermal degradation of polypyrrole: effect of temperature and film thickness. *Synthetic Metals 52*, 1 (1992), 33–44.

[85] Truong, V.-T., Ennis, B. C., Turner, T. G., and Jenden, C. M. Thermal stability of polypyrroles. *Polymer International 27*, 2 (1992), 187–195.

[86] Sixou, B., Mermilliod, N., and Travers, J. P. Aging effects on the transport properties in conducting polymer polypyrrole. *Physical Review B 53* (1996), 4509–4521.

[87] Sixou, B., Travers, J., and Nicolau, Y. Effect of aging induced disorder on transport properties of pani-csa. *Synthetic Metals 84*, 1-3 (1997), 703–704.

[88] Rannou, P., Nechtschein, M., Travers, J., Berner, D., Woher, A., and Djurado, D. Ageing of PANI: chemical, structural and transport consequences. *Synthetic Metals 101*, 1-3 (1999), 734–737.

[89] Tobolková, E., Prokeš, J., Křivka, I., Trchová, M., and Stejskal, J. Temperature- and humidity-related degradation of conducting polyaniline films. *Macromolecular Symposia 212*, 1 (2004), 447–454.

[90] Papathanassiou, A. N., Grammatikakis, J., Sakellis, I., Sakkopoulos, S., Vitoratos, E., and Dalas, E. Hopping charge transport mechanisms in conducting polypyrrole: Studying the thermal degradation of the dielectric relaxation. *Applied Physics Letters 87*, 15 (2005), 154107.

[91] Ricks-Laskoski, H. L., and Buckley, L. J. Twenty-year aging study of electrically conductive polypyrrole films. *Synthetic Metals 156*, 5-6 (2006), 417–419.

[92] Sakellis, I., a.N. Papathanassiou, and Grammatikakis, J. Pressure dependence of the dielectric loss in semi-conducting polypyrrole aged at room temperature. *Synthetic Metals 160*, 19-20 (2010), 2228–2230.

[93] Stejskal, J., Prokeš, J., and Trchová, M. Reprotonated polyanilines: The stability of conductivity at elevated temperature. *Polymer Degradation and Stability 102* (2014), 67–73.

[94] Alix, A., Lemoine, V., Nechtschein, M., Travers, J., and Menardo, C. Water absorption study in polyaniline. *Synthetic Metals 29*, 1 (1989), 457–462.

[95] MacDiarmid, A. G., and Epstein, A. J. Polyanilines: A novel class of conducting polymers. *Faraday Discussions of the Chemical Society 88* (1989), 317–332.

[96] Matveeva, E. Residual water as a factor influencing the electrical properties of polyaniline. the role of hydrogen bonding of the polymer with solvent molecules in the formation of a conductive polymeric network. *Synthetic Metals 79*, 2 (1996), 127–139.

[97] Casanovas, J., Canales, M., Fabregat, G., Meneguzzi, A., and Alemán, C. Water absorbed by polyaniline emeraldine tends to organize, forming nanodrops. *The Journal of Physical Chemistry B 116*, 24 (2012), 7342–7350. PMID: 22690647.

[98] MacDiarmid, A., and Epstein, A. J. The concept of secondary doping as applied to polyaniline. *Synthetic Metals 65*, 2–3 (1994), 103–116.

[99] Travers, J., and Nechtschein, M. Water effects in polyaniline: A new conduction process. *Synthetic Metals 21*, 1–3 (1987), 135–141.

[100] Byshkin, M., Buonocore, F., Matteo, A. D., and Milano, G. A unified bottom up multiscale strategy to model gas sensors based on conductive polymers. *Sensors and Actuators B: Chemical 211* (2015), 42 –51.

[101] Taunk, M., Kapil, A., and Chand, S. Hopping and tunneling transport over a wide temperature range in chemically synthesized doped and undoped polypyrrole. *Solid State Communications 150*, 37-38 (2010), 1766–1769.

[102] Münstedt, H. Properties of polypyrroles treated with base and acid. *Polymer 27*, 6 (1986), 899–904.

[103] Li, Y., and Qian, R. Studies on the chemical compensation of conducting polypyrrole by naoh solution. *Synthetic Metals 26*, 2 (1988), 139–151.

[104] Pei, Q., and Qian, R. Protonation and deprotonation of polypyrrole chain in aqueous solutions. *Synthetic Metals 45*, 1 (1991), 35–48.

[105] Neoh, K. G., Young, T. T., Kang, E. T., and Tan, K. L. Structural and mechanical degradation of polypyrrole films due to aqueous media and heat treatment and the subsequent redoping characteristics. *Journal of Applied Polymer Science 64*, 3 (1997), 519–526.

[106] Truong, V.-T., McMahon, P. J., and Wilson, A. R. Alkali-treated semiconducting polypyrrole for infrared detection. *Journal of Polymer Science Part B: Polymer Physics 50*, 9 (2012), 624–630.

[107] Bidez, P. R., Li, S., MacDiarmid, A. G., Venancio, E. C., Wei, Y., and Lelkes, P. I. Polyaniline, an electroactive polymer, supports adhesion and proliferation of cardiac myoblasts. *Journal of Biomaterials Science, Polymer Edition 17*, 1-2 (2006), 199–212. PMID: 16411609.

[108] Aleshin, A. N. Polymer nanofibers and nanotubes: Charge transport and device applications. *Advanced Materials 18* (2006), 17–27.

[109] Long, Y., Zhang, L., Chen, Z., Huang, K., Yang, Y., Xiao, H., Wan, M., Jin, A., and Gu, C. Electronic transport in single polyaniline and polypyrrole microtubes. *Physical Review B 71*, 16 (2005), 165412.

[110] Stejskal, J. Conducting polymer-silver composites. *Chemical Papers 67*, 8 (2013), 814–848.

[111] Ćirić Marjanović, G. Recent advances in polyaniline composites with metals, metalloids and nonmetals. *Synthetic Metals 170* (2013), 31–56.

[112] Guiseppi-Elie, A. Electroconductive hydrogels: Synthesis, characterization and biomedical applications. *Biomaterials 31*, 10 (2010), 2701–2716.

[113] Stallinga, P. Electronic transport in organic materials: Comparison of band theory with percolation/(variable range) hopping theory. *Advanced Materials 23*, 30 (2011), 3356–3362.

[114] Pipinys, P., and Kiveris, A. Variable range hopping and/or phonon-assisted tunneling mechanism of electronic transport in polymers and carbon nanotubes. *Central European Journal of Physics 10*, 2 (2012), 271–281.

[115] Balint, R., Cassidy, N. J., and Cartmell, S. H. Conductive polymers: Towards a smart biomaterial for tissue engineering. *Acta Biomaterialia 10*, 6 (2014), 2341–2353.

[116] Bai, H., and Shi, G. Gas sensors based on conducting polymers. *Sensors 7*, 3 (2007), 267–307.

[117] Kukla, A., Shirshov, Y., and Piletsky, S. Ammonia sensors based on sensitive polyaniline films. *Sensors and Actuators B: Chemical 37*, 3 (1996), 135–140.

[118] Li, Z.-F., Blum, F. D., Bertino, M. F., and Kim, C.-S. Understanding the response of nanostructured polyaniline gas sensors. *Sensors and Actuators B: Chemical 183* (2013), 419–427.

[119] Schroder, D. *Semiconductor material and device characterization*. John Wiley and Sons, New York, 1998. ISBN 0–471–24139–3.

[120] Kremer, F., and Schönhals, A., Eds. *Broadband Dielectric Spectroscopy*. Springer, Berlin, 2003. ISBN 3–540–43407–0.

[121] Keithley–Application note series. *High Resistance Measurements*, 2005. http://www.keithley.com/emarketing/resourceguides/LowLevelMeasurements_Volume2/referenceLibrary_1_Volume2.

[122] Matsumura, T., Obokata, T., and Fukuda, T. Two-dimensional microscopic uniformity of resistivity in semi-insulating gaas. *Journal of Applied Physics 57*, 4 (1985).

[123] Blood, P., and Orton, J. W. The electrical characterisation of semiconductors. *Reports on Progress in Physics 41*, 2 (1978), 157.

[124] Borup, K. A., Toberer, E. S., Zoltan, L. D., Nakatsukasa, G., Errico, M., Fleurial, J.-P., Iversen, B. B., and Snyder, G. J.

Measurement of the electrical resistivity and Hall coefficient at high temperatures. *Review of Scientific Instruments 83*, 12 (2012), 123902.

[125] Rietveld, G., Koijmans, C., Henderson, L., Hall, M., Harmon, S., Warnecke, P., and Schumacher, B. DC conductivity measurements in the Van der Pauw geometry. In *Precision Electromagnetic Measurements, 2002.* (2002), pp. 414–415.

[126] Pauw, L. v. d. A method of measuring specific resistivity and Hall effect of discs of arbitrary shape. *Philips Research Reports 13* (1958), 1–9.

[127] Montgomery, H. C. Method for measuring electrical resistivity of anisotropic materials. *Journal of Applied Physics 42*, 7 (1971).

[128] Hemenger, P. M. Measurement of high resistivity semiconductors using the Van der Pauw Method. *Review of Scientific Instruments 44*, 6 (1973).

[129] Kremer, F., and Schönhals, A. Broadband dielectric measurement techniques. In *Broadband dielectric spectroscopy*, F. Kremer and A. Schönhals, Eds. Springer, 2003, ch. 2. ISBN 3–540–43407–0.

[130] Kopecká, J., Kopecký, D., Vrňata, M., Fitl, P., Stejskal, J., Trchová, M., Bober, P., Morávková, Z., Prokeš, J., and Sapurina, I. Polypyrrole nanotubes: mechanism of formation. *RSC Advances 4*, 4 (2014), 1551–1558.

[131] Varga, M., Kopecká, J., Morávková, Z., Křivka, I., Trchová, M., Stejskal, J., and Prokeš, J. Effect of oxidant on electronic transport in polypyrrole nanotubes synthesized in the presence of methyl orange. *Journal of Polymer Science Part B: Polymer Physics 53*, 16 (2015), 1147–1159.

[132] Kopecký, D., Škodová, J., Vrňata, M., and Fitl, P. Polypyrrole micro/nanostructure prepared using azo dyes with different substituents. *Advances in Materials Physics and Chemistry 2* (2012), 89–91.

[133] Škodová, J., Kopecký, D., Vrňata, M., Varga, M., Prokeš, J., Cieslar, M., Bober, P., and Stejskal, J. Polypyrrole-silver composites prepared by the reduction of silver ions with polypyrrole nanotubes. *Polymer Chemistry 4* (2013), 3610–3616.

[134] Kopecká, J. Personal communication, 2015. University of Chemical Technology Prague, Department of Physics and Measurements, Prague.

[135] Stejskal, J., and Gilbert, R. Polyaniline. preparation of a conducting polymer(iupac technical report). *Pure and Applied Chemistry 74*, 5 (2002), 857–867.

[136] Sapurina, I., and Stejskal, J. The mechanism of the oxidative polymerization of aniline and the formation of supramolecular polyaniline structures. *Polymer International 57*, 12 (2008), 1295–1325.

[137] Bláha, M., Varga, M., Prokeš, J., Zhigunov, A., and Vohlídal, J. Effects of the polymerization temperature on the structure, morphology and conductivity of polyaniline prepared with ammonium peroxodisulfate. *European Polymer Journal 49*, 12 (2013), 3904 – 3911.

[138] Bober, P., Trchová, M., Prokeš, J., Varga, M., and Stejskal, J. Polyaniline-silver composites prepared by the oxidation of aniline with silver nitrate in solutions of sulfonic acids. *Electrochimica Acta 56*, 10 (2011), 3580–3585.

[139] Pandis, C., Peoglos, V., Kyritsis, A., and Pissis, P. Gas sensing properties of conductive polymer nanocomposites. *Procedia Engineering 25* (2011), 243–246. EurosensorsXXV.

[140] Aleshin, A. N., Lee, H. J., Park, Y. W., and Akagi, K. One-dimensional transport in polymer nanofibers. *Physical Review Letters 93*, 19 (2004), 15–18.

[141] Kaiser, A., and Graham, S. Temperature dependence of conductivity in 'metallic' polyacetylene. *Synthetic Metals 36*, 3 (1990), 367–380.

[142] Paasch, G., Schmeisser, D., Bartl, A., Naarmann, H., Dunsch, L., and Gopel, W. Structure-conductivity relation for polypyrrole with a two-dimensional microscopic structure. *Synthetic Metals 66* (1994), 135–142.

[143] Armes, S. P. Optimum reaction conditions for the polymerization of pyrrole by iron(III) chloride in aqueous solution. *Synthetic Metals 20* (1987), 365–371.

[144] Omastová, M., Trchová, M., Kovářová, J., and Stejskal, J. Synthesis and structural study of polypyrroles prepared in the presence of surfactants. *Synthetic Metals 138* (2003), 447–455.

[145] Blinova, N. V., Stejskal, J., Trchová, M., Prokeš, J., and Omastová, M. Polyaniline and polypyrrole: A comparative study of the preparation. *European Polymer Journal 43*, 6 (2007), 2331–2341.

[146] Long, Y., Chen, Z., Shen, J., Zhang, Z., Zhang, L., Huang, K., Wan, M., Jin, A., Gu, C., and Duvail, J. L. Magnetoresistance studies of polymer nanotube/wire pellets and single polymer nanotubes/wires. *Nanotechnology 17*, 24 (2006), 5903–5911.

[147] Mativetsky, J., and Datars, W. Morphology and electrical properties

of template-synthesized polypyrrole nanocylinders. *Physica B: Condensed Matter 324*, 1-4 (2002), 191–204.

[148] Yoon, C., Reghu, M., Moses, D., Heeger, A., Cao, Y., Chen, T., Wu, X., and Rieke, R. Hopping transport in doped conducting polymers in the insulating regime near the metal-insulator boundary: polypyrrole, polyaniline and polyalkylthiophenes. *Synthetic Metals 75*, 95 (1995), 229–239.

[149] Salmón, M., Keiji Kanazawa, K., Diaz, A. F., and Krounbi, M. A chemical route to pyrrole polymer films. *Journal of Polymer Science: Polymer Letters Edition 20*, 3 (1982), 187–193.

[150] Maddison, D. S., and Tansley, T. L. Variable range hopping in polypyrrole films of a range of conductivities and preparation methods. *Journal of Applied Physics 72*, 10 (1992).

[151] Kaiser, A. B. Thermoelectric power and conductivity of heterogeneous conducting polymers. *Physical Review B 40* (1989), 2806–2813.

[152] Duvail, J. L., Rétho, P., Fernandez, V., Louarn, G., Molinié, P., and Chauvet, O. Effects of the confined synthesis on conjugated polymer transport properties. *The Journal of Physical Chemistry B 108*, 48 (2004), 18552–18556.

[153] Mikat, J., Orgzall, I., Lorenz, B., Sapp, S., Martin, C. R., Burris, J. L., and Hochheimer, H. D. High-pressure low-temperature electrical properties of template-synthesized polypyrrole at low synthesis temperature: dimensional crossover under pressure. *Physica B 265* (1999), 154–159.

[154] Joo, J., Lee, J., Baeck, J., Kim, K., Oh, E., and Epstein, J. Electrical, magnetic, and structural properties of chemically and electrochemically synthesized polypyrroles. *Synthetic Metals 117*, 1-3 (2001), 45–51.

[155] Xuan, Y., Liu, X., Desbief, S., Leclère, P., Fahlman, M., Lazzaroni, R., Berggren, M., Cornil, J., Emin, D., and Crispin, X. Thermoelectric properties of conducting polymers: The case of poly(3-hexylthiophene). *Physical Review B 82*, 11 (2010), 115454.

[156] Pelster, R., Nimtz, G., and Wessling, B. Fully protonated polyaniline: Hopping transport on a mesoscopic scale. *Physical Review B 49*, 18 (1994), 12718–12723.

[157] Aleshin, A., Lee, K., Lee, J., Kim, D., and Kim, C. Comparison of electronic transport properties of soluble polypyrrole and soluble polyaniline doped with dodecylbenzene-sulfonic acid. *Synthetic Metals 99*, 1 (1999), 27–33.

[158] Zhang, Z., Deng, J., and Wan, M. Highly crystalline and thin polyaniline nanofibers oxidized by ferric chloride. *Materials Chemistry and Physics 115*, 1 (2009), 275–279.

[159] Baćani, M., Novak, M., Kokanović, I., and Babić, D. Hopping electron transport in doped polyaniline: An experimental verification of the Fogler-Teber-Shklovskii model. *Synthetic Metals 172* (2013), 28–31.

[160] Kahol, P., Satheesh Kumar, K., Geetha, S., and Trivedi, D. Effect of dopants on electron localization length in polyaniline. *Synthetic Metals 139*, 2 (2003), 191–200.

[161] Alekseeva, E. Personal communication, 2015. Charles University in Prague, Faculty of Mathematics and Physics, Prague.

[162] Stejskal, J., Riede, A., Hlavatá, D., Prokeš, J., Helmstedt, M., and Holler, P. The effect of polymerization temperature on molecular weight, crystallinity, and electrical conductivity of polyaniline. *Synthetic Metals 96*, 1 (1998), 55–61.

[163] Varga, M., Prokeš, J., Bober, P., and Stejskal, J. Electrical conductivity of polyaniline–silver nanocomposites. In *WDS'12 Proceedings of Contributed Papers: Part III – Physics*, J. Šafránková and J. Pavlů, Eds. Matfyzpress, 2012. ISBN 978–80–7378–226–9.

[164] Varga, M., Prokeš, J., Bober, P., and Stejskal, J. On the electrical conductivity of silver-content-controlled polyaniline–silver composites. *Journal of Nanostructured Polymers and Nanocomposites 9* (2013), 76–83.

[165] Kharoo, H. L., Gupta, O. P., and Hemkar, M. P. Phonon-limited electrical and thermal resistivities of noble metals. *Physical Review B 18* (1978), 5419–5426.

[166] McMillan, W. L. Scaling theory of the metal-insulator transition in amorphous materials. *Physical Review B 24* (1981), 2739–2743.

[167] Carslaw, H. S., and Jaeger, J. C. *Conduction of Heat in Solids*, 2 ed. Clarendon Press, Oxford, 1959. ISBN 0198533683.

[168] Rudajevová, A., Varga, M., Prokes, J., Kopecká, J., and J., S. The study of thermal properties of polypyrrole nanotubes. *Acta Physica Polonica A* (2015). Accepted.

[169] Zimmerman, W. *Multiphysics Modelling with Finite Element Methods*. Series on stability. World Scientific, 2006. ISBN 9789812568434.

[170] Geuzaine, C., and Remacle, J.-F. Gmsh: A 3-D finite element mesh generator with built-in pre- and post-processing facilities. *International*

Journal for Numerical Methods in Engineering 79, 11 (2009), 1309–1331.

[171] Dular, P., and Geuzaine, C. GetDP reference manual: The documentation for GetDP, a general environment for the treatment of discrete problems. http://www.geuz.org/getdp/.

[172] Erlandsson, R., Inganäs, O., Lundstr om, I., and Salaneck, W. XPS and electrical characterization of BF_4–doped polypyrrole exposed to oxygen and water. *Synthetic Metals 10*, 5 (1985), 303–318.

[173] Wolter, A., Rannou, P., Travers, J. P., Gilles, B., and Djurado, D. Model for aging in hcl-protonated polyaniline: Structure, conductivity, and composition studies. *Physical Review B 58* (1998), 7637–7647.

[174] Rudajevová, A. Personal communication, 2014. Charles University in Prague, Faculty of Mathematics and Physics, Prague.

[175] Hanuš, J. Personal communication, 2014. Charles University in Prague, Faculty of Mathematics and Physics, Prague.

[176] Mičušík, M. Personal communication, 2014. Polymer Institute Slovac Academy of Sciencies, Bratislava.

List of Tables

List of Symbols and Abbreviations

α, β	parameters of phenomenological HN dielectric function
α_r	thermal coefficient for resistivity
α_m	m-th zero of Bessel function
$\Delta\epsilon$	dielectric strength
ϵ_0	permittivity of free space
$\epsilon_\mathrm{s}, \epsilon_\infty$	$\lim_{\omega\to 0}\epsilon(\omega)$, $\lim_{\omega\to\infty}\epsilon(\omega)$
η	volume fraction of conducting islands in insulating matrix
$\hbar$	reduced Planck constant
λ	image forces correction to the barrier potential
ν_ph	phonon attempt frequency
ν_{ij}	single-phonon hopping rate
ρ,r	electrical resistivity, resistivity at reference temperature
ρ_c	water content density, molar concentration of acids, templates
σ	electrical conductivity
σ	electrical conductivity
σ_0	pre-exponential factor σ_0 in various models, initial conductivity
$\sigma_\mathrm{f}, \sigma_\mathrm{m}$	conductivity of filler/matrix
σ_RT	room temperature conductivity
σ_∞	asymptotic value of conductivity
σ_kc	pre-exponential factor related to the conductivity-water coupling
τ	relaxation time
φ	electric potential

ξ	the localization length
A	area, prefactor in Eq. (1.48), Eq. (4.11) and Eq. (4.13)
a	monomer size, adjustable parameter in the power law model
B	magnetic induction
B_{c}	crossover field in magnetoresistance
C	capacity
c	water content
$C_{\mathrm{sat}}, B_{\mathrm{sat}}$	adjustable parameters in magnetoresistance model
D	electric displacement, dimension, diffusion coefficient
d	grain size, diameter
e	elementary electric charge
E_0	characteristic parameter in dependence of conductivity on electric field
E_{c}	charging energy
E_{F}	Fermi energy level
E_{ij},R_{ij}	energy distance of two mid-gap states, spatial distance of two mid-gap states
f	geometrical factor in the Kaiser's model
f, ω	frequency, angular frequency
$g(E_{\mathrm{F}})$	density of states at the Fermi level
h	thickness
I	electric current
k	coupling constant between conductivity and water
k_{B}	Boltzmann constant
l	length
L_{B}	magnetic length

m, m^*, m_e	mass, effective mass, free electron mass
n	charge carrier concentration, exponent in VRH model
P	polarization
p	pressure
p_F,k_F	Fermi momentum, Fermi wavevector
R	resistance
R_p,R_c,R_sp, R_s	probe resistance, contact resistance, spreading resistance, sample resistance
R_hop, E_hop	optimum hopping distance, hopping activation energy
s	separation between grains in CELT model, exponent in power law models
T, T_r	temperature, reference temperature
T_0	parameter T_0 in exponential of various models
t_0	electronic transfer energy
T_p	polymerization temperature
U	Coulomb repulsion energy in the CELT model
U	voltage
W	reduced activation energy
x, y, z, r, φ	spatial coordinates
z	number of nearest neighbor chains
1D, 2D, 3D	one-dimensional, two-dimensional, three-dimensional
AR	acid red
BNN	Barton-Nakajima-Namikawa relation
CP	conducting polymers
CSA	camphorsulfonic acid
DBSA	dodecylbenzenesulfonic acid

EMA	effective medium approximation
ES VRH	Efros-Shklovsii variable range hopping
FCA	phtalocyaninesulfonic acid
FEM	finite element analysis method
FTIR	Fourier-tranformed infrared spectroscopy
GM	granular metal model
HCl	hydrochloric acid
LT, HT	low temperature, high temperature region/data
MIT	metal-to-insulator transition
MR	magnetoresistance
MSA	methanesulfonic acid
NNH	nearest neighbor hopping
OG	orange G
PA	polyacetylene
PAMPSA	poly(2-acrylamido-2-methyl-1-propanesulfonic acid)
PANI	polyaniline
PEDOT	poly(3,4-ethylenedioxythiophene)
PL	power law
PPV	poly(*p*-phenylene vinylene)
PPy	polypyrrole
PPy-NT	polypyrrole nanotubes
PSSA	poly(4-styrenesulfonic acid)
PT	polythiofene
Q1D VRH	quasi-one-dimensional variable range hopping
RFEB	the random free-energy barrier model

SEM	scanning electron microscopy
SSH	Su-Schrieffer-Heeger hamiltonian
Suc	succinic acid
SY	sunset yellow
TGA	thermogravimetric analyis
vdP	van der Pauw configuration
VRH	variable range hopping model
WAXS	wide angle x-ray scattering